

MODEL BASED ANALYSIS OF MULTIMODAL
NEUROIMAGING: FROM NEURAL MASSES TO
SPECTRAL GRAPH THEORY

A Dissertation

Presented to the Faculty of the Weill Cornell

Graduate School of Medical Sciences

in Partial Fulfillment of the Requirements for the Degree of

Doctor of Philosophy

by

Xihe Xie

November 2021

© 2021 Xihe Xie

ALL RIGHTS RESERVED

MODEL BASED ANALYSIS OF MULTIMODAL NEUROIMAGING: FROM
NEURAL MASSES TO SPECTRAL GRAPH THEORY

Xihe Xie, Ph.D.

Cornell University 2021

The direct link between human neurobiology and observed brain dynamics drives fundamental research efforts in neuroscience. Alongside technological advances, multimodal brain imaging enlarged the coverage of observable brain characteristics, and data-driven network theoretics emerged as a valuable framework for understanding high dimensional datasets and building biophysical models of brain function. This dissertation explores brain patterns arising from the underlying anatomy with structure-function models of different complexity and spatio-temporal scale, pairing theoretical models with tools from dynamical systems, signal processing, and optimization.

Non-invasive brain imaging has numerous common sources of variability, here we showcase workflows featuring increased precision and accelerated computing speed. Through these automated workflows, networks describing the underlying white-matter connections of the brain were obtained as the structural basis of our work. The combination of connection strengths and inter-region delays provided anatomical networks that were rich in information. We find in nonlinear neural mass models summarizing neuron population firing rate, sub-optimal inference and practical shortcomings hinder analysis when extending to the whole brain network. We then showcase linear, low dimensional network models of brain function that utilize the brain's anatomical connectivity, reproducing spatial patterns in the slower blood-oxygen-level-dependent (BOLD)

regimes as well as highly oscillatory encephalography frequencies. With ideas originating from spectral graph theory, our interpretable parameters capture the spatial distributions of brain activity in addition to observed functional patterns, supporting recent findings that suggest the resting brain is macroscopically linear.

BIOGRAPHICAL SKETCH

Xihe Xie was born in Beijing, China in 1991. After completing elementary school in China, Xihe moved to the United States to reunite with his family and resumed his schooling in Forest Hills, New York. While attending Francis Lewis High School, he encountered charismatic teachers in his STEM classes, sparking his initial interests in science and engineering. Before moving onto The City College of New York with a full scholarship, Xihe left his mark at Francis Lewis High School by organizing students and teachers to fund raise for a robotics team, which went on to compete in the FIRST robotics competitions and eventually grew into a specialized STEM curriculum at the high school. In college, Xihe played on the Men's volleyball team and became team captain in his senior year. During the off-season, Xihe joined the labs of Dr. Lucas Parra and Dr. Marom Bikson, where his fascination with high dimensional data and signal processing concepts was put to use in neuroscience for the first time. Xihe completed his undergraduate degree in Biomedical Engineering as *magna cum laude* and a Tau Beta Pi Engineering Honor society inductee.

During the two years after graduation, Xihe took on two junior level biomedical device jobs in industry, but quickly grew weary of the entry level tasks after completing training. But now having some expendable income, Xihe would quit both of his jobs during the summers and backpacked through 11 countries in Asia and Europe. Upon Xihe's return from his second trip, he was eager to begin pursuing his neuroscience Ph.D. and resume learning in a more curious academic environment. Xihe began his graduate school career as an early enrollee in July 2015 at Weill Cornell Graduate School of Biomedical Sciences in the lab of Dr. Keith Purpura. Soon after, Xihe would join the lab of Dr. Ashish Raj to investigate multi-modal neuroimaging and models of the human brain's

structure-function relationship. Despite an unexpected move to UCSF led by Dr. Raj, Xihe published two research articles through collaborations with Dr. Srikantan Nagarajan at UCSF, two commentary articles as part of the Brainhack community, an open source software, numerous collaborations, and a manuscript for future publication at the time of graduation. Xihe took on many volunteering, teaching assistant, and organizer roles for Brainhack and Neuromatch events and was awarded the Repronim/INCF Fellowship in 2020.

Beyond the lab, Xihe was actively involved in both the Weill Cornell and UCSF communities. He was the sports and gym liaison for the student government at Weill Cornell, and he became an officer at UCSF's Open Science Group in his short time on the West Coast. In addition to volunteering at educational outreach programs in NYC, he was a teaching assistant and workshop speaker at many hackathons. As part of his ReproNim/INCF Fellowship training, Xihe created a course with Dr. Amy Kuceyeski named *data science basics in neuroscience* to fulfill the graduate school's quantitative curriculum requirement, but with a more practical and modern approach. With his newly acquired hackathon skills, Xihe contributed to open source projects such as Jupyter and Nipy. Xihe's most treasured memories away from his work laptop are the scenic road trips with his graduate school friends and the sunny days spent playing beach volleyball at Ocean Beach or Brooklyn Bridge Park.

Especially to my supportive family, and to all those who have: listened, commiserated, advised, shared, encouraged, and celebrated (repeating as many times as necessary), I dedicate this dissertation with my deepest gratitude.

ACKNOWLEDGEMENTS

First and foremost, I would like to thank Dr. Ashish Raj and Dr. Srikantan Nagarajan, two advisors that provided opportunities and countless valuable advice from Weill Cornell to UCSF. Ashish always pushed the boundaries and was open to new things, Sri asked important questions and taught me how to critically approach the problems and tasks at hand. I am very appreciative of my thesis committee: Dr. Amy Kuceyeski, Dr. Keith Purpura, and Dr. Jonathan Victor, for sharing their expertise which was invaluable at every meeting. Thank you as well to Dr. Pablo F. Damasceno for accompanying me on pursuits of better data practices and mentorship advice.

I am extremely grateful for the Neuroscience Department at Weill Cornell Graduate School for providing a welcoming community and outstanding opportunities for teaching and peer led learning. Thanks to UCSF's Open Science Group, the Brainhack organizers, and Neurohackademy instructors, communities that kept me energized and shared valuable knowledge in scientific knowledge, publishing, ethics, and data practices. Thank you to the ReproNim team, INCF, and the ReproNim Fellowship trainers for broadening my horizons on the possibilities of scientific efforts.

Thank you to my fellow scientists and friends at Weill Cornell for their expertise and support that got me through first-year courses. Thank you to my group of classmates and friends: Thomas, Rosa, Mitchell, and George who always showered me with warm welcomes whenever I visited from SF. Last, but not least, thank you to my Family. My parents have been incredibly supportive throughout my entire life, and I am lucky to have caring extended families in New York City, Beijing, and Chiba. To my parents, thank you for your sacrifices and for being there for me despite your busy work schedule.

TABLE OF CONTENTS

Biographical Sketch	iii
Dedication	v
Acknowledgements	vi
Table of Contents	vii
List of Tables	x
List of Figures	xi
1 Introduction & Background	1
1.1 Structure-Function Problem	2
1.2 Mean Field Theory & Dynamical Models	3
1.3 Graph Theory and Network Extensions	7
1.4 Connectivity	9
1.4.1 Causality	10
1.4.2 Simpson's Paradox	11
1.4.3 Brain data is still interesting	12
1.5 Summary	13
2 Advances in Diffusion MRI	15
2.1 Diffusion Tensor Imaging	15
2.1.1 Diffusion MRI Drawbacks	18
2.2 DESIGNER Preprocessing Pipeline	19
2.2.1 Pipetography	25
2.3 Tractography	33
2.3.1 GPU-accelerated Diffusion MRI Tractography in DIPY . .	33
2.3.2 Results	34
2.3.3 Discussion and Conclusion	34
3 Whole Brain Network Neural Mass Models: A Criticism	37
3.1 Introduction	37
3.2 Methods	41
3.2.1 Experimental Procedure	41
3.3 The Wilson-Cowan Local Oscillator Model	47
3.4 Oscillator Model Performance	48
3.5 Network Extension of Wilson-Cowan Model	52
3.5.1 Network Model Performance	56
3.5.2 NMM Based Analysis	64
3.5.3 MCMC Convergence & Other Approaches	66
3.5.4 Dynamic Causal Modeling	68
3.5.5 Variational Inference	68
3.5.6 Challenges and Limitations	70
3.5.7 Conclusion	70

4	Emergence of Canonical Functional Networks from the Structural Connectome	72
4.1	Introduction	72
4.2	Theory	76
4.2.1	Network Diffusion of Brain Activity	76
4.2.2	Complex Laplacian Matrix	78
4.3	Methods	80
4.3.1	Structural Connectivity Network Computation	80
4.3.2	Canonical Functional Networks	81
4.3.3	Global Parameter Optimization for Individual Structural Eigenmodes	81
4.3.4	Similarity Analysis Between Canonical Functional Networks and Cumulative Linear Combination of Structural Eigenmodes	82
4.4	Results	84
4.4.1	Structural connectivity based functional activation patterns	84
4.4.2	Eigenmodes of the complex Laplacian resemble CFN activation patterns	85
4.4.3	Parameter tuning of complex Laplacian eigenmodes . . .	86
4.4.4	Complex Laplacian eigenmodes outperform real Laplacian eigenmodes	90
4.4.5	Group level eigenmode analysis	92
4.5	Discussion	93
4.5.1	A simple yet feature-rich graph theoretic approach	94
4.5.2	Higher predictive power than existing graph models . . .	95
4.5.3	Complex eigenmodes accommodate a diversity of spatial patterns	95
4.5.4	Rich repertoire is tunable with two biophysical parameters	96
4.5.5	Relationship to existing studies	98
4.5.6	Limitations	101
4.6	Conclusions	102
5	Spectral Graph Theory of Brain Oscillations	104
5.1	Introduction	104
5.1.1	The Structure-Function Problem in Neuroscience	104
5.1.2	A hierarchical, analytic, low-dimensional and linear spectral graph theoretic model of brain oscillations	107
5.2	Methods	110
5.2.1	Spectral graph model development	110
5.2.2	Macroscopic scale: signal evolution on the entire graph . .	114
5.2.3	Experimental Procedures	117
5.2.4	Data Processing	118
5.2.5	Model Optimization	121
5.3	Results	122

5.3.1	Graph Laplacian eigenmodes mediate a diversity of frequency responses	122
5.3.2	Spectral distribution of MEG power depends on model parameters but not connectivity	126
5.3.3	Spectral graph model recapitulates the spatial distribution of MEG power	130
5.4	Discussion	136
5.4.1	Recapitulating regional power spectra at all frequencies	137
5.4.2	Revealing sources of heterogeneity in spatial patterns of brain activity	138
5.4.3	Macroscopic brain rhythms are governed by the connectome	138
5.4.4	Emergence of linearity from chaotic brain dynamics	140
5.4.5	Relationship to other work	141
5.4.6	Other limitations and extensions	143
5.4.7	Potential applications	143
A	Appendix: Supplementary Figures	145
Bibliography		148

LIST OF TABLES

3.1	Whole Brain Neural Mass Model Parameter Inference Publications and their performance. This table does not include publications with whole brain mean field models or mechanistic models of neural activity.	41
3.2	Default parameters for the Wilson-Cowan oscillator model. The excitatory driving force P and time constants τ_e and τ_i are inferred during our experimentation, and their initial values are shown here. All default values are set such that small inputs would cause the system to oscillate (near the Hopf bifurcation point). . .	46
5.1	SGM parameters values and limits	111
A.1	Statistical comparison between HCP connectome and random connectome with Pearson's correlation.	146
A.2	Statistical comparison between HCP connectome and random connectome with Spearman's correlation.	147

LIST OF FIGURES

1.1	Oscillatory Dynamics of Neural Mass Model.	6
1.2	Network schematics.	9
1.3	Simpson's Paradox.	12
2.1	Illustrations of diffusion	16
2.2	Axial view of human brain's fiber orientation distribution.	17
2.3	Marchenko-Pastur distribution.	22
2.4	Gibb's Ringing Removal.	24
2.5	BIDS Structured Dataset Example	28
2.6	Processing pipeline overview	30
2.7	Example pre-processing output file tree	31
2.8	Example pre-processing output file tree	32
2.9	GPU streamline generation speedup compared to CPU	35
2.10	Visualization of GPU generated streamlines.	36
3.1	Illustration of a Wilson-Cowan oscillator unit.	38
3.2	MCMC sampling of posterior distribution when maximizing likelihood to average MEG power spectrum.	43
3.3	Exhaustive grid search of the local oscillator model.	49
3.4	MCMC sampling of posterior distribution when maximizing likelihood to average periodic power spectrum.	51
3.5	Source localized MEG functional connectivity matrices.	52
3.6	Network model behavior in response to external driving force	53
3.7	Network Wilson Cowan model sampling results for one representative subject.	55
3.8	Comparison between MEG spectra and network model simulated spectra for 4 subjects.	57
3.9	Global Parameters Sampling for maximizing likelihood to α band coherence.	60
3.10	Global Parameters Sampling for maximizing likelihood to amplitude envelope correlation.	62
3.11	Comparison between MEG spectra and posterior mean global parameters simulated spectra for 4 subjects.	63
4.1	The analysis overview.	79
4.2	Complex Laplacian eigenmode for different parameter choices.	84
4.3	Canonical functional networks reproduced by structural eigenmodes.	87
4.4	Structural eigenmode spatial similarity to canonical functional networks depends on model parameters.	88
4.5	Canonical functional networks have complex Laplacian eigenmode specificity.	90

4.6	Structural eigenmodes of the HCP template complex Laplacian predict canonical functional networks better than structural eigenmodes of the real Laplacian.	91
4.7	Complex Laplacian outperforms real Laplacian in recapitulating canonical functional networks with individual structural connectomes.	93
5.1	The linearized spectral graph model.	109
5.2	Spectral graph model spectra for one subject.	124
5.3	Spectral graph model depicts MEG spectra.	127
5.4	Spectral graph model parameter optimization.	129
5.5	Alpha power spatial distribution depicted by specific spectral graph model eigenmodes.	131
5.6	Beta power spatial distribution depicted by specific spectral graph model eigenmodes.	133
5.7	Spatial correlation performance of the SGM.	134
A.1	Parameter dependency of structural complex Laplace eigenmodes.	145
A.2	Spatial similarity quantified by Spearman's correlation	146
A.3	Dice coefficient optimized spatial correlation.	147

CHAPTER 1

INTRODUCTION & BACKGROUND

Structural diversity and functional complexity of the human central nervous system is often placed into spotlight through the lens of evolution. While the sheer difference in cortex size might be the most striking difference between primate and other vertebrate brains, human brains stand out even more by its ability to invention and communicate symbol systems, which is poorly equipped in other primates. What special human brain functionality allowed us to invent cultural tools such as languages, numeric systems, and even arithmetics? As an exercise, one can consider two possible hypothesis at extreme ends of the structure-function argument:

- Cultural functionality is acquired by expanded cortical plasticity unique to human brains, where newly acquired skills can be attributed to freshly established connections independent of an anatomical constraint.
- Humans have evolved specialized circuitry in the cortex, and specific brain circuitry contributes to unique cognitive functions.

With the plastic brain scenario from the first hypothesis, one can imagine if a group of people learned to play video games with novel control mechanisms, the plasticity induced changes in each person's brain may occur at various unpredictable locations in the brain. On the other hand, one would imply brain regions responsible for language and arithmetic are only found in humans. Of course, both of these extremes have been proven false by evidence. Specialists like musicians experience enhanced sensorimotor functions after repeated association, feedback, and cognitive practices, which are hallmarked by strengthened

connections near the arcuate and intraparietal sulcus [1]. Whereas mechanisms for vocal learning is identified in song birds [2] and symbolic associations and computations in primate brains were also found to be associated with their prefrontal and parietal structures [3, 4]. If anatomical structures do support development of specialized functions in the brain, then how exactly does the complex connections made by billions of neurons give rise to the functional signals recorded by neuroscientists today?

1.1 Structure-Function Problem

Elucidating how structure shapes observable function is at the heart of a wide spectrum of scientific disciplines. Often, functional units have easily discernible structures governing their roles in a biological system. For example, the 3D molecular structure of a protein forming an ion channel receptor for transport across membranes. As the system becomes more complex, it becomes increasingly difficult to explain emergent function in relation to its underlying structure. Currently, the most complex physical system in the known universe is the central nervous system; the dense synaptic connections and staggering axonal projections in the brains of even simple organisms underlie the myriad of fascinating behaviors in nature.

The relationship between the brain's structure and function is of particular interest in neuroscience, and outside of the bench science laboratories, non-invasive imaging and physiological recordings have paved way for mathematical models relating biological structure to observed function. Hodgkin and Huxley published the first successful model of ionic currents in 1952, simulating the action

potential of neurons revealing behavior of ion channels and how types of ion channels can give rise to action potentials [5]. Their work fueled experiments and simulations for the deciphering the diverse electrical activity in the central nervous system. Since then, new experimental techniques to measure neuronal activity at larger populations have become available for models of different scales, including optical recordings with voltage sensitive dyes over a cranial window, functional magnetic resonance imaging (fMRI), or high temporal resolution electro-encephalography (EEG) or magneto-encephalography (MEG) methods. These more powerful measurement techniques have revealed patterns of coherent activity that span larger volumes of the cortex, and with it, newer ideas of modeling coherent neural activity,

1.2 Mean Field Theory & Dynamical Models

Properties of neuronal spikes and mechanistic models of neuron firing tells a microscopic story of single neuronal unit decision making based on accumulation of evidence, but more complex behavior such as movement and cognition do not arise from the spikes of a single neuron. Instead, the collective behavior of many cortical, thalamic, and spinal neurons in a large nervous system network dictates behavior. But at this larger macroscopic scale, are there conceptual frameworks to mathematically model collective neural activity rather than mechanistic ion channels? Turns out in everyday life and most branches of science, there exists observed phenomena that reflects collective behavior and not that of individual units. Research in these areas is based on mathematical laws that govern macroscopic variables such as magnetic fields or fluid flow [6, 7]. These laws provide a framework for integrating, explaining, and predicting observed empirical data.

In neuroscience, there indeed exists mean field theories of electromagnetic brain activity [8]. Rather than focusing on the ionic properties of an individual spiking neuron, such mean field models described the action of populations of neurons [9]. With advanced computing power and larger data collectives, these models have been established to model seizures [10], encephalographies [11], sleep [12], anesthesia [13], and resting-state brain networks [14, 15]. Additionally, more effective approaches to model inversion; i.e. estimating likelihood of model parameters from data, make such models powerful tools for understanding perception, behavior, and multimodal neuroimaging data.

The core concept behind mean field models are dynamical systems. First established by Newton and Leibniz, these differential equations describe how a variable changes as a function of the system's current states and parameters. The most famous example is Newton's second law $F = ma$, or more formally: $\frac{dV}{dt} = \frac{F}{m}$. Where a is the acceleration and V is the velocity of a mass m under some force F . While Newton used such concepts to study planetary motion, dynamical systems expressing temporal dynamics of a system according to some underlying physical law can easily be translated to biology. For example, the Hodgin-Huxley model consist of membrane potential and ion channel variables, and differential equations are then derived from the biophysics of ion flow through voltage-gated channels, the conversion of the potential into firing rate, and other biophysical properties of neurons [5, 16].

Single neuron spikes are highly nonlinear, and mean field approaches assume that coherent dynamics of neurons populations resemble that of single neurons. Accordingly, the mean ensemble activity is modeled with the same conductance-based theory as seen in single neuron spiking: the all-or-nothing

firing of individual neurons is replaced by a sigmoid-shaped activation function that maps average membrane potential to mean firing rate. Such nonlinear systems of differential equations is complex and no clear analytical solution exists. Poincare had an insightful analysis of dynamical systems, illustrating the existence of a geometric phase space spanned by all of the system's variables [17]. A point in this space corresponds to unique combination of the system's states, yielding not only a time course for each of the variables, but also attractor behavior, bifurcation, and stability analysis.

Attractors describe the characteristics of a dynamical system's activity: steady state, periodic, or chaotic. In terms of neuron dynamics, a periodically spiking neuron corresponds to a limit cycle attractor, but when a current input occurs, then chaotic oscillation is exhibited. While an attractor is structurally stable when a small change in parameters leads to slight changes in its shape, unstable attractors are found near bifurcation parameter values, where slight parameter changes drastically shifts dynamic behavior. Additionally, neurons are in constant presence of noise due to thermal energy, ion channel fluctuations, and irregular inputs from its connections [18, 19]. Adding random noise to our dynamical system is the equivalent to adding perturbations at each time step, which may cause switching between attractor states. Figure 1.1 is an example Wilson-Cowan oscillator model (which we will see in more detail in Chapter 3)'s temporal dynamics and phase planes illustrated for different states, showing parameter regimes that produces steady states and limit cycle activity.

While the mathematics of stochastic differential equations is not trivial, modern large-scale brain dynamics are rooted in stochastic processes. The two key ingredients for differential equations are a coupling term that represents synaptic

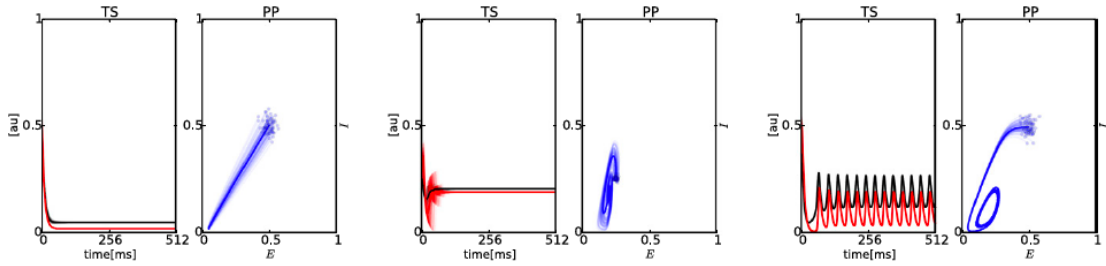


Figure 1.1: Oscillatory Dynamics of Neural Mass Model.

Black lines are the traces of excitatory neuron population E and red lines are those of inhibitory population I . Solid black and red lines are the average time courses computed over different brain regions. The $E - I$ plane trajectories are also shown for two stable states and a limit cycle state. Model parameters and simulations follow those of the *Virtual Brain* defaults and as reviewed in [20].

interactions between neurons, and a noise term to disrupt synchronization. The mathematical complexity of such models are one main reason why nonlinear dynamical systems have yet made their way into clinical settings. Another reason being mean field approaches view the brain dynamics as a forest while ignoring the behavior of individual trees and their leafs, meaning the inferred model parameters are a rough method to reduce the dimensionality of complex high dimensional data [21]. Interpreting model parameter estimates require robust methods to evaluate their values, as these estimates are sensitive to arbitrarily selected initial conditions and biases introduced by the objective function. Adding a network connections term and expanding the same dynamical system to all brain regions in a network further creates non-identifiability issues of model parameters. Chapter 3 will provide an overview of such a mean field model where we used a bare-bones approach to examine model performance and parameter interpretability, showing weaknesses in whole brain extensions of all-or-nothing nonlinear firing rates, and setting up analytical linear approaches to whole brain modeling in Chapter 4 and 5.

1.3 Graph Theory and Network Extensions

Evidence of correlated activity is observed at the microscopic scale of communicating neurons, prompting extensive efforts to theoretically model these synchronous input and output relationships for decision making [22, 23, 24, 25]. While information from single neuron spike recordings can be sufficiently summarized with poisson distributions and probabilistic models [26, 27], high dimensional data from whole brain recordings with fMRI, EEG, and MEG require dimensionality reduction for meaningful interpretation. Graph theory and network theoretics have emerged as an advantageous tool in the field of neuroimaging.

The field of network neuroscience seeks to understand systems that are defined by nodes, or an individual functional unit, and their interactions through connections, which are often referred to as edges (see Figure 1.2). Together, these units and connections form a network where specific dynamics play out, building models that can explain, describe, or predict behavior of real physical networks. For example, pairwise interactions can be described using an $N \times N$ adjacency matrix [28], where N is the number of nodes in the network, and each ij -th element of the matrix gives the connection strength between nodes i and j . The properties of the adjacency matrix are characterized using a framework of mathematical approaches known as graph theory. In neuroscience, the nodes can be chosen to reflect anatomical or functional units, such as cell bodies at the microscale or functionally distinct volumes at the macroscale. On the other hand, edges can be chosen to represent anatomical connections based on synapses, white matter streamlines or even statistical similarities in dynamics [29, 30, 31, 32].

There are common measures of interest simply from the graph itself. For example, clustered connections can be used to identify locally efficient subgraphs or larger-scale "communities" that has specialized functions [33]. Sparsely connected nodes can indicate "cavities" of architecture for information segregation [34, 35]. Hubs are nodes which are more connected than usual, which can be localized or globally connected to form a "rich club" [36]. Such properties have already helped reveal how neurophysiological synchrony and information transmission is supported by specific nodes & edge architectures [37, 38, 39]. However, the works shown here will focus on an alternative application of graph theory: embedding data in a network and creating principled theory of how the system that generated the data might work [40]. Such theory based models will combine a graph with a differential equation specifying dynamics of the nodes, edges, or both, granting the ability to make claims about the mechanism or dynamics that a data-driven network focused on empiricism cannot make.

Theory-based models commonly implement dynamic systems defined at each node. In neuroscience, the Hodgkin-Huxley model [5] or the Rulkov map neurons [41] are relevant at the neuronal microscopic scale. For populations of neurons, the FitzHugh-Nagumo [42] or Kuramoto oscillators [43] are all viable. For this work, we are focusing on whole brain MEG and fMRI data, therefore our nodes represent volumes of gray matter tissue. Mean field approach based models have been used in combination with edge adjacency matrices derived from white matter tractography for network dynamics [44]. At the whole-brain level, models must abstract away many anatomical details to ensure that the mathematics is manageable and the results are interpretable [45]. Additionally, at this macroscopic end of brain function, metrics such as functional connectivity do not necessarily have a physical counterpart, meaning laws of network models

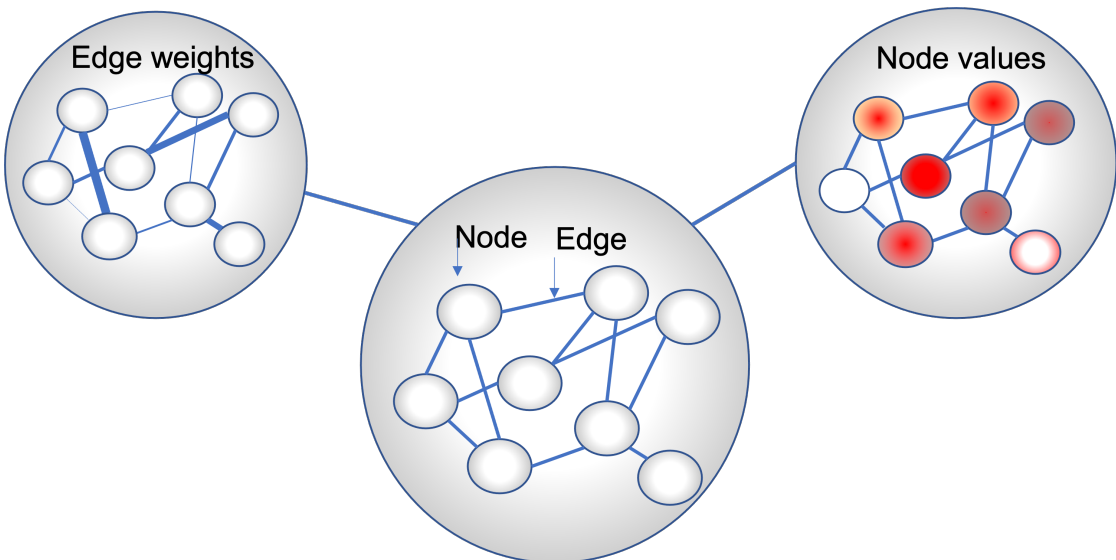


Figure 1.2: Network schematics.

The simplest and most commonly used network model for neural systems is to represent pattern of connections (edges) between neural units (nodes). More sophisticated network models can be created from the simplest example shown here, such as adding edge weights and node values or explicit functions for dynamic. There are more complex hypergraphs and dynamically evolving graphs not shown in this example.

that capture the observed statistical functional patterns is more or less abstract or conceptual at best. This distinction between realism and phenomenology is important in determining whether a model can be used to infer functional patterns of realistic anatomy.

1.4 Connectivity

Here in this work, we aim to understand the neuronal populations and their interactions between each other, and how they gives rise to our observed functional data. However, neuroscientists cannot directly measure interactions, statistical techniques are used to infer interactions from simultaneously recorded brain signals, and finally asking the question: how does population A mechanisti-

cally affect population B? Functional connectivity converts measured signals into statistical estimates of "connectivity", which are then thought of as a measure or approximation of some strength of interactions. Some techniques include using information flow [46], granger causality [47], coherence analysis [48, 49], or dynamic causal modeling [50]. In some cases, estimated connectivity are interpreted as able to replicate network properties of functional or anatomical neural data without attributing causal significance [51, 52, 53]. In fact, our work in Chapter 4 aims to describe functional brain organization popularized by [53]. However, another philosophy interprets changes in parameter estimates in more causal terms; describing mechanisms in learning and cognition [54, 55, 56], pathological processes [57, 58, 59, 60], or re-organization from plasticity [61, 62]. Connectivity measures are functions of correlations, thus the language and interpretations should reflect such. Terms such as "improvement in predictive power", "model comparison", or "conditional correlations" can more precisely described what's done.

1.4.1 Causality

Connectivity implies a connection between two things, whereas causality implies cause and effect. A variable causally affects another variable if a perturbation of the first variable would induce a change in the activity of another variable [63]. Or for neuroscientists, if a neuron influences another neuron, then perturbing the first (electrically) would affect the second, and the same concept for regions of the brain. However, it is always possible to construct a common input which will produce the same effect on a neuron that we believe is influenced by another neuron. Similarly, if there's no causal influence between two neurons

A and B, it is always possible to use an additional neuron C to change A and B so that they now look like they do interact. This logical weakness, statistical confounding, stems from the existence of unobserved variables that affect the observed data in a way that often makes the estimation of connectivity impossible. In neuroimaging, the countless unobserved variables (billions of neurons) likely have more influence than the few observed ones (number of sensors), and statistical tools that fit to low-dimensional brain recordings ignore the the high dimensional aspects of brain activity, they describe the statistics of joint neural data without causal insights. More importantly, the signals we observe in small areas can span arbitrary dimensions related to other confounds, e.g. movement related signals in visual cortex [64, 65]. Therefore, we are in situations where the number of confounds is many orders of magnitude greater than the number of measured variables.

1.4.2 Simpson's Paradox

We can use a very simple example to highlight the threat of confounding, a scenario where an unobserved interaction can either cancel out an effect or induce spurious effects [66]. Imagine there are two brain states (See Figure 1.3 for illustration), and one is associated with high activity of neuron A and low activity of neuron B, while another is associated with low activity of neuron A and high activity of neuron B. If we do not know the brain state (confound) one may conclude that A has a negative influence on B. But if we know the brain states, we then see that A increases the activity of B. In neuroimaging datasets, it is possible to directly observe Simpson's paradox. For instance, the choice of analysis parameters, such as seed regions, functional parcellations, and network

community separation, may yield different results [67, 68].

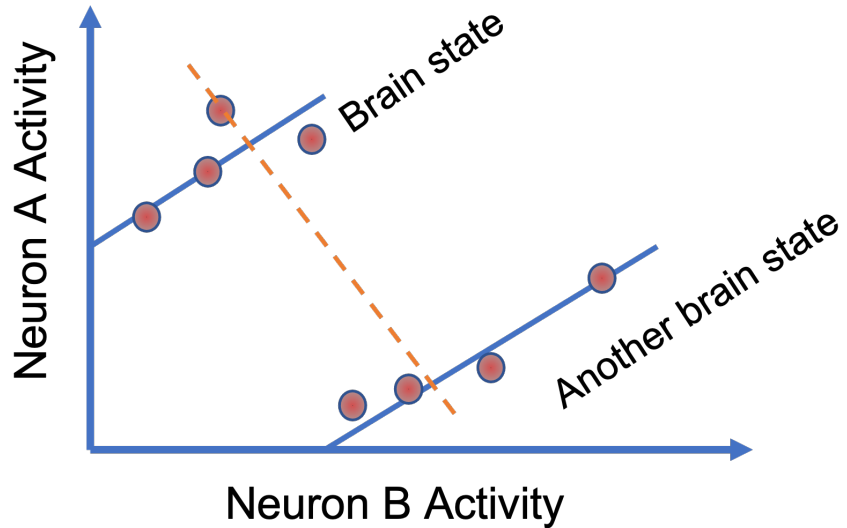


Figure 1.3: Simpson's Paradox.

The dots represent neural activity recordings from both neurons. The orange line indicates a negative correlation between A and B. However, this correlation is confounded by the two brain states which are not observed. The blue line indicate that each brain state has a positive correlation between A and B. The Simpson's paradox showing a correlation is not indicative of causality.

1.4.3 Brain data is still interesting

If we do not expect causal inference to be possible, then what is left to do with neuroimaging data? This conundrum does not imply that trying to understand the joint dynamics of many neurons or brain areas is not interesting. For example, low dimensional projections of brain recordings can reveal invariant patterns [69, 70] and potential biomarkers [71, 72, 73] pending experiments to find neuronal equivalents. Besides perturbation studies, the confounding problem may not be an issue in exhaustively recorded and mapped out systems, and it would be interesting to examine connectivity in small organisms such as *c. elegans*,

aplysia, or larval zebrafish. More possibilities are covered in the opinion piece by Mehler & Kording [74], who made me feel compelled to include this section of text. In Chapters 4 and 5 of this work, we showcase mappings between anatomical white-matter connections to joint dynamics of brain regions. And we use this introduction as an opportunity to state that joint statistics are not meaningful statements about causality, but more biological insights may be derived from correlations and mappings we show, and hopefully pave way for a linear framework of macroscopic scale brain dynamics.

1.5 Summary

Network extensions of mean field models have had a difficult time penetrating the barrier between research and practicality. The justification for averaging over molecules is often plausible in statistical physics, but whether this logic works in neuroscience remains an open question. To our knowledge, there has been no study that shows networks that computes like brains can be approximated by the underlying mean field approximation. To be specific, every neuron is special in the sense that they do not interact with random neurons, but a fixed set, or even worse, a set that changes through neuroplasticity. Additionally, newer works in deep learning that ditches theory for empiricism is already outperforming these crude abstractions of neurophysiology in terms of speed and predictive power [75, 76, 77]. However, we might not have to surrender theory for full on data driven interpolations just yet. Spectral graph theory, which studies a graph in relationship to the characteristic polynomial, eigenvalues, and eigenvectors, have given rise to a family of whole brain models that utilizes far richer anatomical connection information.

Chapter 2 will cover in detail how adjacency matrices, or "connectomes" are derived from diffusion weighted imaging (DWI), additionally showcasing advances made in image processing and white matter streamline generation. Chapter 3 will then examine how mean field approaches incorporate connectomes to model whole brain network dynamics and discuss its disconnects from reality. Chapter 4 will illustrate a simple use of spectral graph theory to attain spatial patterns of brain dynamics. Together with Chapter 5, we showcase the rich amount of information that can be extracted from the spectral properties of brain networks. We believe the intricate organization of the brain has many specialized properties or functions we are yet unaware of, and the future is bright for careful combinations of experiment, modeling, and theory that will link increasingly realistic models with more neuroanatomical detail for analysis of observed neurophysiology.

CHAPTER 2

ADVANCES IN DIFFUSION MRI

2.1 Diffusion Tensor Imaging

Diffusion is a process that involves the movement of molecules via thermally driven random motions, or namely Brownian motion (see Figure 2.1). Generally, factors such as molecular weight, viscosity, and temperature are the common solution properties influencing diffusion. However, in biological tissues, the cellular organization of the tissue influences the mobility of diffusing molecules by acting as obstacles within our organs. In certain cases, this means that the distance traveled by a diffusing molecule in one direction will not be the same as some other directions. As a comparison, in a solution with no barriers to diffusion, diffusion is isotropic or the same in all directions (See Figure 2.1, middle). On the other hand, if diffusion is hindered by some particularly oriented barriers, then it is termed anisotropic diffusion (Figure 2.1, right). In the anisotropic scenario, the structural organization of the barriers can be identified simply by the diffusion patterns and the degree of anisotropy is directly related to the geometry of the barriers.

Diffusion weighted imaging(DWI) takes advantage of the phenomenon that water diffusion is highly anisotropic in tissues of the nervous system. In magnetic resonance imaging techniques, diffusion is often measured by an "apparent diffusion coefficient" (ADC). Which is not a *true* measure of the intrinsic diffusion, but instead a metric dependent on the interaction of the molecule (water in most biological usages) with the cellular structures over a given amount of diffusion time. In contrast to DWI, diffusion tensor imaging (DTI) computes a diffusion

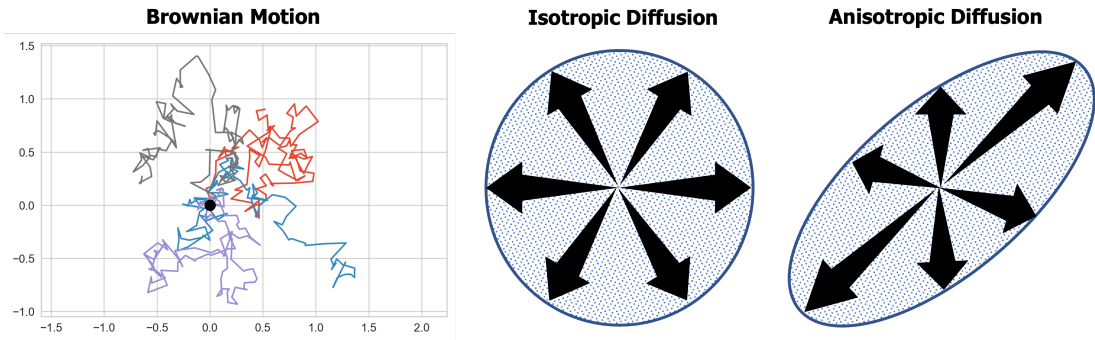


Figure 2.1: Illustrations of diffusion

Left: Diffusion process illustrated by simulated Brownian motion where four particles, indicated by different colors, all begin at the same origin of $(0, 0)$ yet end up with different random paths. In biological tissues, diffusion path of water molecules will be influenced by cellular microstructures. Middle: cartoon illustrating diffusion with similar molecular displacement in all directions (isotropic). Right: cartoon illustrating greater diffusion in one direction over others (anisotropic).

tensor that's a 3-by-3 matrix instead of one numerical value. This 3D tensor allows estimates of water mobility in all directions for a given voxel, enabling quantification of anisotropic diffusion. The methodology to combine diffusion metrics with magnetic resonance pulses was introduced by Stejskal and Tanner in 1960 [78], and eventually adapted to clinical routines by Le Bihan and colleagues in 1980 [79]. The key idea in this adaptation is that stationary water spin signal will be the same in response to two magnetic pulses of opposite polarities, but moving water will return spin signals in a different position, giving off a weaker signal. The difference in signal attenuation is proportional to the water motion. Modern DTI acquisition routines reduce scan time by sending a series of oscillation gradient reversals instead of a train of 180° pulses. Water movement is sampled in all directions covered by the diffusion sensitive gradients, providing quantification of diffusion in x, y, z directions of a 3D brain volume.

The concept of diffusion coefficient is only briefly covered here, as there has been much more sophisticated methods of quantifying anisotropic diffusion

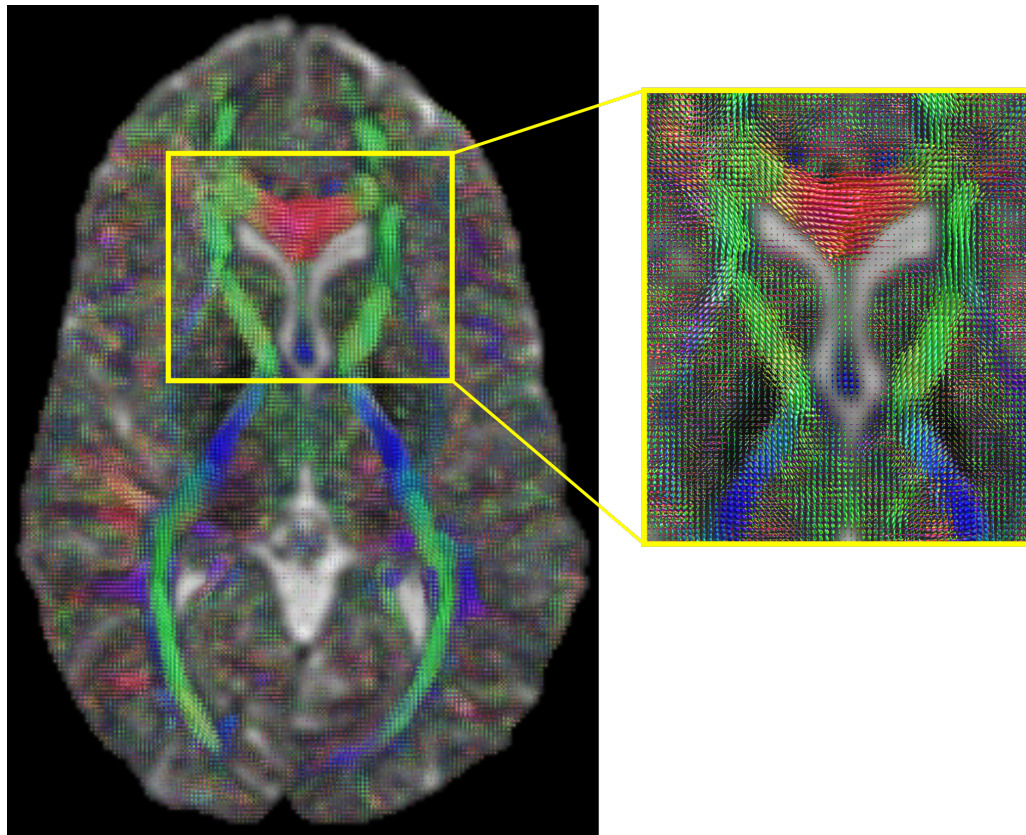


Figure 2.2: Axial view of human brain’s fiber orientation distribution.

Tri-dimensional representation of water diffusion along white-matter fibers with color coded x (red), y (green), z (blue) axes representing main diffusion direction. Spherical models provide information about the degree of anisotropy, with longer poles representing directed diffusion and smaller spheres representing isotropic diffusion. Zoomed in region showing anisotropic diffusion along the corpus callosum.

[80, 81, 82, 83]. However, the simple ADC framework provides an intuitive feel for diffusion tensors and has led to many valuable findings. Early observations of water diffusion in human brains *in vivo* focused on areas of large diffusion variation. Measurements showing a range of diffusion constants in white-matter fibers with different gradients revealed myelinated sheaths, microfilaments, and axonala membranes can act as barriers to water molecules traveling along the length of axons [84]. On the other hand, gray matter does not exhibit anisotropic diffusion due to the lack of long oriented fiber structures [85, 86]. Subsequently,

studies showing anisotropic water diffusion in animal brains and spinal cords [87, 88, 89] in addition to human cranial nerves [90, 91] proved the usefulness of diffusion weighted MRI. Eventually, DTI was adapted for measuring brain maturation [92, 93] as well as non-invasive fiber orientation [94].

2.1.1 Diffusion MRI Drawbacks

While diffusion tensors became even more widely adapted with modern neuroscience studies acquiring multiple modalities of brain images at the same time, improving the signal to noise ratio (SNR) of DWI contrasts and accuracy of tensors have also shifted into focus. Despite its clinical usages for both brain [87, 95] and body [96, 97], a low signal to noise ratio and artifact contamination are usual sources of low confidence in diffusion measurements. Specifically, long scan echo times (60-120 ms) and strong diffusion gradient pulses limits precision, and subsequently the accuracy of diffusion estimations after acquisition [98, 99]. Aside from post hoc digital processing, improved SNR can be achieved by lengthening scan time or lowering spatial resolution. Longer scan times for each gradient direction only increases precision slowly, while echo times imposed by hardware and acquisition protocol prevents changes in scan time. Additionally, loss in anatomical detail and smoothing effects contradicts the goal of improving SNR by lowering spatial resolution.

Unlike hardware imposed SNR deficits, diffusion MRI in humans suffers from additional artifacts from a variety of sources. While all MR acquisitions experience degrees of motion artifacts, diffusion MRI is exceedingly sensitive to motion. During the strong gradient pulses, any head motion or small tissue

movement such as pulsating flow amplifies the detected shifts in molecules. If all spin shifts detected in all voxels experience the same motion displacement, there is minimal loss in signal coherence and effects on ADC measurements. However, problematic artifacts occur when voxels in different slices of MR acquisition experience different degrees of motion during a single MR pulse sequence. In addition, macroscopic head motion will not be identical replicas of itself every time, and an accumulation of shifts over time during a sequence of pulses will lead to large signal variations across the image[100]. Another artifact arising from repeated gradient pulse switches is eddy currents, where conducting surfaces in the MRI machinery induct currents in response to the on-off switching of magnetic pulses, which results in erroneously persisting gradients in addition to the main gradient [101, 102]. As mentioned before, low spatial sampling resolution to shorten scan time is common in diffusion MRI acquisition protocol, the effect of this shortcoming is exacerbated when high-contrast boundaries are poorly sampled, leading to Gibbs ringing artifacts [103, 104, 105]. Such boundary artifacts have been identified to cause inaccuracies such as erroneous negative diffusivity and kurtosis values (kurtosis map black voxels) [103, 106, 107]. Lastly, spatial signal bias caused by radio frequency pulse inhomogeneity which also requires correction [108, 109].

2.2 DESIGNER Preprocessing Pipeline

Improving diffusion tensor estimates via spatial smoothing [110] or averaging [111] are considered brute force techniques that do not specifically target a type of contamination such as Gibbs ringing or thermal noise. To amend the noise and artifact issues mentioned above, Ades-Aron and colleagues proposed the DE-

SIGNER pipeline, which stands for "Diffusion parameter ESTimation with Gibbs and NoisE removal" [112]. This preprocessing pipeline was shown to increase diffusion estimation precision by a factor of 2 compared to aforementioned pipelines while preserving spatial resolution. Since then, specific proposed procedures in DESIGNER has been adapted into the open source software *mrtrix3* [113].

Mrtrix3 provides a large collection of functionality for diffusion MRI focused processing and analysis. Similar to older pre-existing tools such as Freesurfer [114], SPM [115], and FSL [116], the suite of neuroimaging tool provide standalone modules but do not have any pre-established workflows, capabilities for parallel processing across subject data, or a standardized input & output data framework. Although the DESIGNER pipeline is available as an open source Python project, the simple scripts does not comprehensively cover end-to-end diffusion MRI processing, and is not easily scalable to large datasets. Here, we will summarize the problems and preprocessing procedures recommended by DESIGNER, introduce our contributions to automating diffusion MRI processing, and showcase collaborative efforts on accelerating diffusion derived tractography computations.

MP-PCA

The pre-requisite step before targeted artifact removal is to denoise, as corrupted spatially varying MRI data can propagate through preprocessing procedures and lower the accuracy of the final diffusion quantification [117]. The electronic components and the human subject being scanned can introduce a zero mean Gaussian distributed "thermal noise" to the sensitive MR scanners

[118, 119]. This thermal noise is further amplified by parallel imaging acquisition protocols for accelerated scan times, which introduces a non-uniform scaling of the noise amplitudes [120]. This ubiquitous noise becomes a dominant contribution to voxel signals when employing high resolutions, short pulse repetition times, and/or lower magnetic fields [121, 122]. Many existing denoising techniques deals with this spatially variant non-Gaussian noise by weighted averaging of selected patches of voxels that share similar statistics [123, 124, 125, 126, 127, 128]. These approaches suffer from the blurring of the image and introduction of additional partial volume effects that leads to downstream errors or biases in diffusion modeling.

To remove local noise variations while preserving edges in the images, Hotelling proposed the idea of transforming a redundant dataset into principle components and preserving only thee components carrying signal [129]. Hotelling’s assumption that diffusion MRI data is redundant is based on the confirmed phenomenon that 1) correlation between many diffusion weighted signals is brought by one underlying diffusion process, and 2) because the diffusion signals can be modeled be efficient represented by a small number of parameters (spherical models). Since then, it has been shown that principal component analysis (PCA) of redundant data reveals a majority of signal variance is contained in a few components [130, 131] , and the noise associated eigenvalues follow a Marchenko-Pastur (MP) distribution parameterized by non-Gaussian noise variance [132] (See Figure 2.3).

To remove the pure noise associated eigenvalues and eigenvectors, one needs to optimally select the appropriate noise level and the number of noise components to remove before reconstruction of the signal matrix. Coincidentally, the

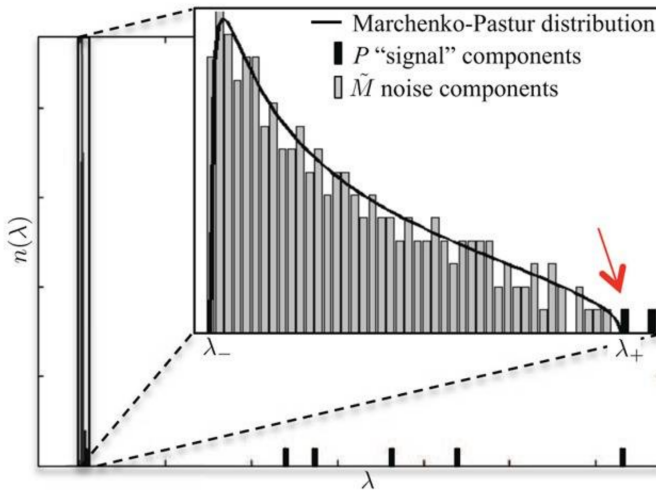


Figure 2.3: Marchenko-Pastur distribution.

Example of simulated Marchenko-Pastur distribution and it's upper end zoomed in, showing a universal characteristic of correlated noise in covariance matrices computed during PCA analysis, distinguishing between noise- and signal-carrying components. Image taken from the published work of Veraart et al., who generated this example with simulated data matrix of size 90×250 [133].

mean of the lowest eigenvalues will exceed the expected value of the MP distribution if at least one eigenvalue corresponds to a signal component. Therefore, the denoising algorithm will iteratively add eigen values from the noise end (see Figure 2.3) until the sum of eigen values is greater than or equal to the expected value of the MP distribution. Subsequently, the denoised signal matrix will be reconstructed using the remaining signal components, without compromising anatomical detail and only requires about 1 min of processing time for a whole brain volume.

Gibb's ringing artifact correction

Gibb's ringing is an ubiquitous artifact that manifests as oscillatory signals near sharp image gradients. In the case of brain MRI, the borders between cerebrospinal fluid (CSF), gray matter (GM), and white matter (WM) are the

usual source of Gibb's ringing artifacts due to insufficient sampling. This ringing artifact is clearly illustrated mathematically when we consider that MR images are acquired in k -space. The k -space encodes both the phase and frequency of the acquired data, which represents the spatial frequency information of the MR volume. Every point in the k -space data matrix contains partial information for the complete image, but does not correspond to the same point in the image matrix. The outer rows of k -space contains high spatial frequency data describing information about the borders and contours of the image. On the other hand, the inner parts of the matrix provide information on low spatial frequency content, such as the general contrast of the image [134, 135]. To recover the actual MRI image, one relates the k -space acquired Fourier expansion coefficients to intensities values at voxel x ($I(x)$) as the following:

$$I(x) = \frac{1}{N} \sum_{k=0}^{N-1} c(k) \cdot e^{\frac{-2\pi i k x}{N}} \quad (2.1)$$

where $c(k)$ are the N expansion coefficients in k -space. The Gibb's phenomenon says that while a Fourier series converges exponentially after $2N + 1$ terms for a periodic signal, the convergence deteriorates for a function that is not periodic [136]. In the case of a sharp image transition near boundaries, more high frequency components are required to reconstruct the image. Requiring higher amounts of N components for a sharp edge that deteriorates Fourier series convergence will cause Gibb's ringing artifacts to appear.

Similar to denoising techniques, image filtering approaches to removing Gibb's ringing can smooth the oscillatory artifacts. But the filtering will apply a global smoothing effect, thus the spatial resolution of the image is reduced and finer details are lost [137, 138]. More intricate methods involves piece-

wise reconstruction of smooth regions [137, 139]. But the requirement for edge detection introduces instabilities due to the need for optimal parameter choices. The DESIGNER pipeline recommends an alternative approach where the k -space series expansions are modeled as a sinc function in image space. The method implemented here avoids spatial filtering, and makes use of the fact that the strength of the ringing effect depends on the precise location of the boundary in a sampling grid (or how the sinc function is sampled). The sinc function is found by optimizing the amount of ringing removed, which is quantified by the absolute differences in a certain “neighborhood” around a voxel, and the size of the “neighborhood” is the only parameter required. The final voxel value is obtained by re-interpolating the shifted image positions based on the original image grid voxel intensities [106].

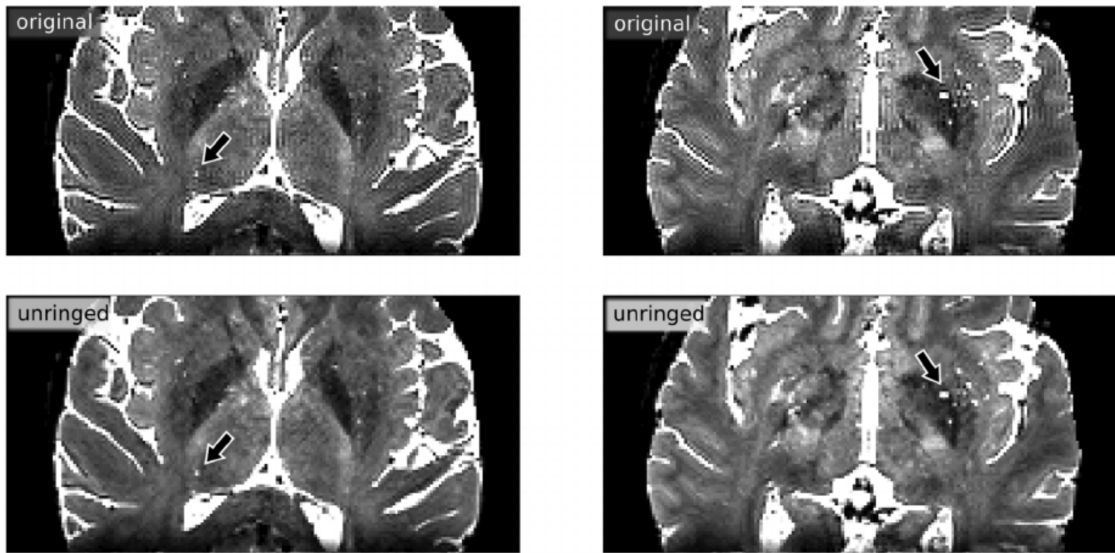


Figure 2.4: Gibb’s Ringing Removal.

Two example anatomical MRI slices with obvious ringing artifacts. Arrows indicating the fine details and peak structures are preserved after removal of ringing. Image taken from the published work of Kellner et al.’s original work on subvoxel shifts [106].

Rician bias correction

The noise in diffusion MRI is governed by a Rician or non-central χ distribution that creates a positive bias in low SNR images [140]. This bias affects the fitting of any diffusion model at high gradient values [140]. Taking advantage of our MP-PCA procedure, the DESIGNER pipeline suggests using the estimated noise level at each voxel to estimate the expected value of the true voxel intensity signal as described by [141], as it has been shown that denoising using MP-PCA returns a proxy expectation value of measured magnitude intensity [133]

B1 inhomogeneity correction

The signal intensity of MR images can be spatially biased due to radiofrequency (RF) field inhomogeneities caused by high-density receiver coils, often named B_1 bias field. This bias often persists through voxels of the same tissue type, and can ultimately affect the final tensor fitting as well. In DESIGNER, it is recommended to estimate this bias field based on the mean $b = 0$ image and apply the field correction to all volumes [142, 143, 144].

2.2.1 Pipetography

While all the diffusion MRI preprocessing procedures discussed above are by no means recent advances in digital image processing, the effort to create accessible and standardized tools has hindered the usability of each methodology. First, tracking down working code and data associated with manuscripts is an impossible task, and the quality of shared code is fully dependent on efforts of

the authors. The original DESIGNER publication [112] provides a simple script for executing the recommended steps in serial, but did not concern themselves with reusability, reproducibility, and data provenance. Since then, <https://brainlife.io> has adopted the DESIGNER pipeline as a standalone module on their publicly accessible cloud computing platform. Brainlife adopts data and code reproducibility principles and is focused on provenance tracking, however, users are limited by inflexible inputs, finite shared computing resources and remote data storage. Overall, there is still a need for an end-to-end tool that takes input diffusion MRI data and outputs network derivatives in a standardized generalizable fashion.

Pipetography (Pipeline for tractography) is an open source Python library that accepts standardized Brain Imaging Data Structure (BIDS) datasets [145] for pre- and post-processing of anatomical and diffusion MRI data. We utilized the Python workflow engine Nipype [146] and its interfaces capabilities with different neuroimaging tools to create a parallelizable standardized workflow for diffusion MRI data processing. The Python library is hosted on the Python package index online for download, whereas documentation, version control, basic testing are hosted through GitHub at <https://github.com/axiezai/pipetography>. The library consists of interfaces that interact with *FSL* [116], *ANTS* [147], and *mrtrix3* [113] for image processing. To improve usability of the library, we also provide containerized images in both Singularity and Docker formats, so users do not need to install all three neuroimaging tools separately. Here, we summarize the inputs and workflows implemented in pipetography and recommend visiting the pipetography webpage for a full working example of diffusion data processing.

BIDS

Despite the fact that MR modality images are routinely acquired for neuroimaging research, there has been no widely adopted standard for organizing and describing the data collected in an imaging experiment. Not only are standardized file naming conventions rarely found within labs, but proper documentation of acquisition protocols and scanner parameters are also often left to individual lab's preferences. This renders sharing and reusing data (within or between labs) difficult if not impossible, and creates an unnecessary barrier that complicates the application of automated pipelines.

The Brain Imaging Data Structure (BIDS) is a standard for organizing and describing MRI datasets. The BIDS standard uses file formats compatible with existing software, unifies the majority of practices already common in the field, and captures the metadata necessary for most common data processing operations. BIDS naming standard (See Figure 2.5) not only provides human understandable names for all imaging outputs, but also provides a way to manage data curation without the need to install and maintain an additional software application. Additionally, data description and neuroimaging meta data is easily accessible through JSON files for reading and usage in neuroimaging tools.

Unlike other neuroimaging data management tools that have not been widely adopted, the BIDS approach provides a very simple naming convention scheme that can be easily employed when converting from scanner DICOM files to Nifti images. Additionally, there exists an ecosystem of BIDS related tools to assist adopting to the standard, and ease execution of commonly used neuroimaging workflows. The suite of BIDS applications simply reads the BIDS folder layout and extracts necessary meta data to minimize human error and maximize

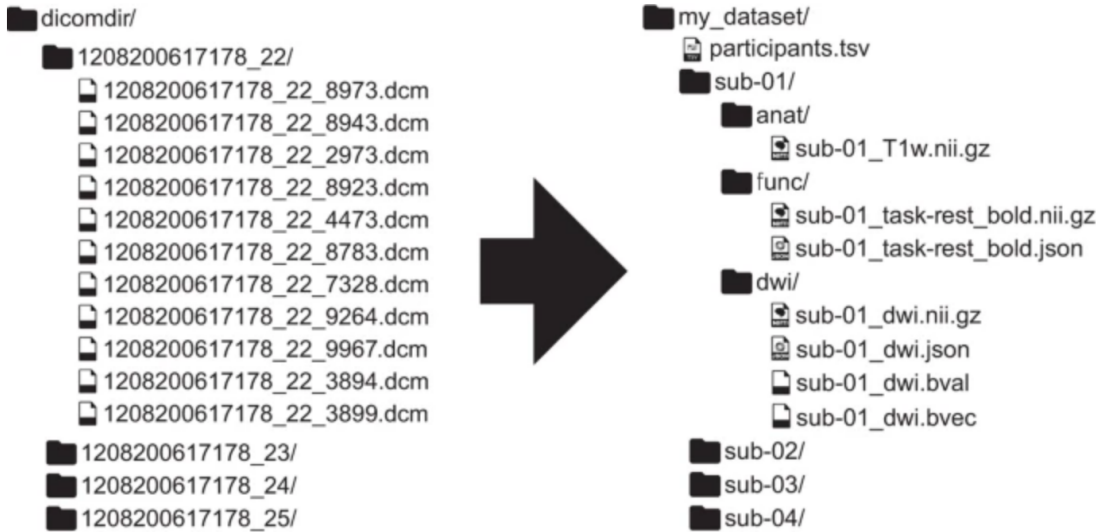


Figure 2.5: BIDS Structured Dataset Example

BIDS is a format for standardizing and describing outputs of neuroimaging experiments (left) in a way that is intuitive to understand and easy to use with existing analysis tools (right).

adaptation.

In *pipetography*, we adapted the BIDS standard so that users can simply provide a directory as input, and the BIDS meta data files alongside the naming convention will allow a layout of subjects and scanning session combinations to be created. All subject-session combinations will construct a workflow graph to execute processing steps, and the entire workflow for the dataset is automatically parallelized across subjects with the help of Nipype. Subsequently, all outputs will be saved according to the BIDS standard as well, with intermediate files saved for provenance. Next, we will summarize the modules implemented for end-to-end processing of a diffusion BIDS dataset.

Anatomical Images

The pipeline is initialized by a *PyBIDS* [148, 149] assisted reading of the BIDS dataset layout, including validation of all file naming and meta data for fulfillment of the required BIDS specifications. With this layout framework, the only required input from users is the BIDS dataset location, workflow graph is automatically created for all subjects and sessions with Nipype. If given enough processing resources (number of CPU's), both anatomical and diffusion MRI processing steps will be executed in parallel as long as pre-requisite inputs are found. The full processing pipeline is illustrated in Figure 2.6, with the anatomical steps summarized in red.

The goal of anatomical MRI processing is to obtain a high resolution brain volume in the standard coordinate space established by the Montreal Neurological Institute (MNI) [150]. Each subject's anatomical MRI volume is transformed and co-registered to the MNI template brain provided by *FSL*, and after skull stripping and brain extraction, a 5 tissue type segmentation is performed [151] to create a binary mask MRI volume highlighting the gray matter white matter interface (GMWMI). The GMWMI voxels will be used as the starting positions for tractography and white matter fiber streamline generation.

DWI

The diffusion weighted image (DWI) module (Figure 2.6, middle) consists of the DESIGNER recommended steps and a few add-on steps to prepare for tractography. In addition to the previously discussed DESIGNER steps, the workflow uses the anatomical module outputs to transform the DWI volume

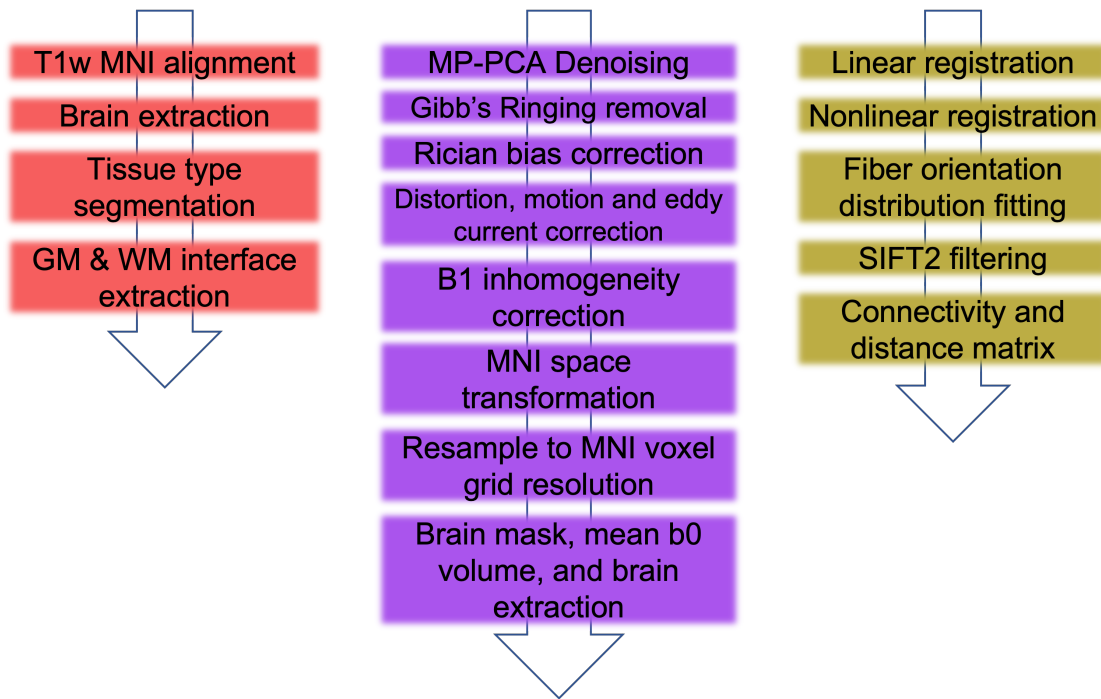


Figure 2.6: Processing pipeline overview

Anatomical MRI preprocessing pipeline (left), diffusion MRI pipeline (middle), and connectome generation (right). The anatomical pipeline feeds its outputs into intermediate steps of the diffusion MRI pipeline. The connectomes pipeline uses diffusion MRI derived fiber tractograms and standard atlases to compute connectivity statistics.

as well as its directional gradients into MNI space, and resamples the voxels to match the voxel grids of the MNI standard. Brain masks, mean b_0 volumes, and skull stripped DWI images will be outputted in BIDS naming convention, a full example output tree is shown in Figure 2.7.

Connectomes

The goal of our research is to use connectome profiles as anatomical information for structure-function modeling of brain activity. Therefore, the last step of the pipeline is to obtain connectivity strength matrices and corresponding distance adjacency matrices in pairs. These matrices consist of rows and columns

```

/Users/xxie/sample_data/dwipreproc/BIDS_output/derivatives/
└── pipetography
    ├── graph
    │   ├── preprocessing.dot
    │   ├── preprocessing.png
    │   ├── preprocessing_detailed.dot
    │   └── preprocessing_detailed.png
    └── sub-01
        └── ses-002
            └── preprocessed
                ├── T1w_space-acpc.nii.gz
                ├── T1w_space-acpc_seg-5tt.mif
                ├── T1w_space-acpc_seg-gmwm_i_mask.nii.gz
                ├── T1w_space-acpc_seg-wm_mask.nii.gz
                ├── dwi_space-acpc_res-1mm.b
                ├── dwi_space-acpc_res-1mm.bvals
                ├── dwi_space-acpc_res-1mm.bvecs
                ├── dwi_space-acpc_res-1mm.json
                ├── dwi_space-acpc_res-1mm.mif
                ├── dwi_space-acpc_res-1mm.nii.gz
                ├── dwi_space-acpc_res-1mm_b0mean.nii.gz
                ├── dwi_space-acpc_res-1mm_seg-brain.nii.gz
                └── dwi_space-acpc_res-1mm_seg-brain_mask.nii.gz

```

Figure 2.7: Example pre-processing output file tree

Following BIDS specifications, the pre-processing outputs are placed in a *derivatives* folder inside the BIDS directory. The *graph* folder has images illustrating the constructed workflow graph that was executed for each subject and session. For each session, a *preprocessed* folder is created to organize all anatomical and DWI derived outputs.

corresponding to parcellated regions in a chosen atlas image, where voxels belonging to a region of interest (ROI) are marked by integer labels instead of MR signal intensities. For each input atlas image, a separate workflow is created to linearly (affine transform) co-register and nonlinearly (warping) co-register the image to the DWI in MNI space. Meanwhile, white matter modeling is performed with a spherical deconvolution approach [152, 153]. However, the density of reconstructed connections is not reflective of the density of underlying white

matter fibers. Therefore, we implement the spherical-deconvolution informed filtering of tractograms (SIFT) method to determine a subset of the streamlines reconstruction such that the streamlines densities throughout the white matter are as close as possible to fiber densities estimated using the spherical deconvolution diffusion model [154]. In particular, the SIFT2 implementation by *mrtrix3* determines an appropriate cross-sectional area multiplier for each streamline rather than removing streamlines altogether, and biologically accurate measures of fiber connectivity are obtained by making use of the complete streamlines reconstruction.

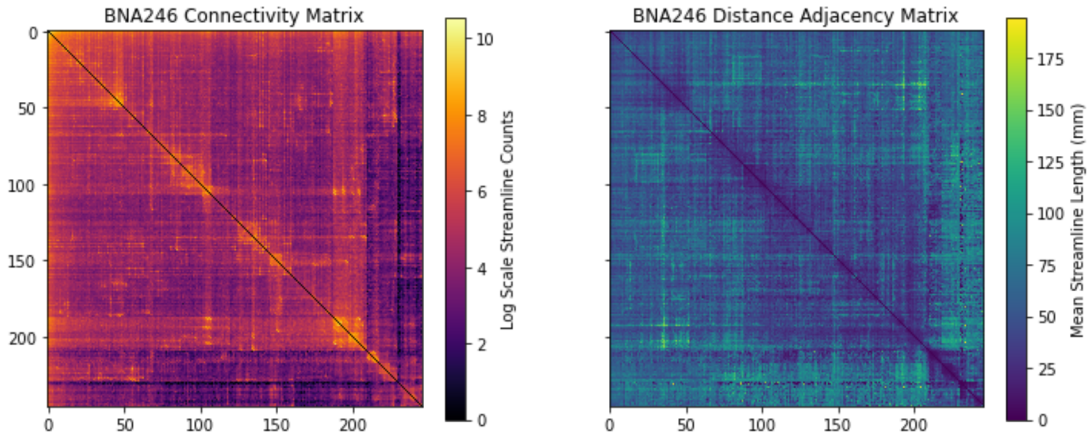


Figure 2.8: Example pre-processing output file tree

Connectivity strength matrix (left) and distance adjacency matrix (right) for the 246 ROIs of the brainnectome atlas, showing strongly connected regions are closely located.

Finally, the connectomes are constructed from input tractograms and parcelation images, weighted by SIFT2's output metrics. The final connectomes are stored in a *connectomes* folder next to *preprocessed* as *.csv* files. An example output for the 246 regions *brainnectome* atlas [155] is shown in Figure 2.8. Next, we will recommend the latest addition in white matter tractogram computation.

2.3 Tractography

Tractography based on diffusion-weighted MRI provides non-invasive in vivo estimates of trajectories of long-range brain connections. These estimates are important in research that measures individual differences in brain connections and in clinical use-cases. But the computational demands of tractography present a barrier to progress. Here, we present a GPU-based tractography implementation that accelerates tractography algorithms implemented as part of the Diffusion Imaging in Python (DIPY) project. This implementation speeds up tractography by at least a factor of 200X, providing tractographies that closely match CPU-based solutions. These speedups enable applications of tractography in clinical data, and in very large datasets.

2.3.1 GPU-accelerated Diffusion MRI Tractography in DIPY

DIPY (Diffusion Imaging in Python; <https://dipy.org>) is an open-source software library that implements many methods in computational neuroanatomy [156]. Relying on the DIPY implementation of residual bootstrap tractography [157], we implemented a multi-GPU parallelizable version constructed on NVIDIA’s CUDA application programming interface (API). The API of the GPU version is compatible with the one implemented in DIPY, enabling direct comparisons and interoperability. A docker container of the software makes the installation and use of the software straightforward. The software is available at <https://github.com/dipy/GPUStreamlines>. Experiments to profile the performance of the algorithm were conducted using an AWS *p3.16xlarge* instance with 8 NVIDIA Tesla V100 Graphical Processing Units and 488 GB RAM.

For comparison, CPU code was run on an AWS *x1e.4xlarge* with 488 GB RAM. We used two datasets, the first is a HARDI acquisition with 2x2x2 mm³ isotropic voxels, 150 b=1,000 s/mm² volumes and 10 b₀ volumes previously described in [158]. The other dataset was a Super-Resolution Hybrid Diffusion Imaging (HYDI) dataset [159], with an effective resolution of 0.625 mm³ isotropic voxels, b=500, 800, 1600, 2600 s/mm², in 134 diffusion directions, and 8 b₀ volumes, also previously described in [160]. In both cases, 27 seeds were placed in each voxel in the white matter to initialize tracking.

2.3.2 Results

In the HARDI dataset, with the seeding approach used here, approximately 2.1M streamlines were generated. Using the CPU-based residual bootstrap tracking algorithm took approximately 13 hours. The GPU-accelerated implementation provides approximately 200-fold speedup with a single GPU, and up to 671-fold speedup with 8 GPUs run in parallel (Figure 2.9). In the HYDI dataset, the seeding approach used generated 150M streamlines (497GB). Tracking in this case with 8 GPU completed in just under 2 hours. A subset of the HYDI streamlines are shown in Figure 2.10.

2.3.3 Discussion and Conclusion

A GPU-based implementation of residual bootstrap tractography provides orders of magnitude speedup, relative to the CPU-based version, while providing solutions that match CPU-based solutions very closely. This was demonstrated in

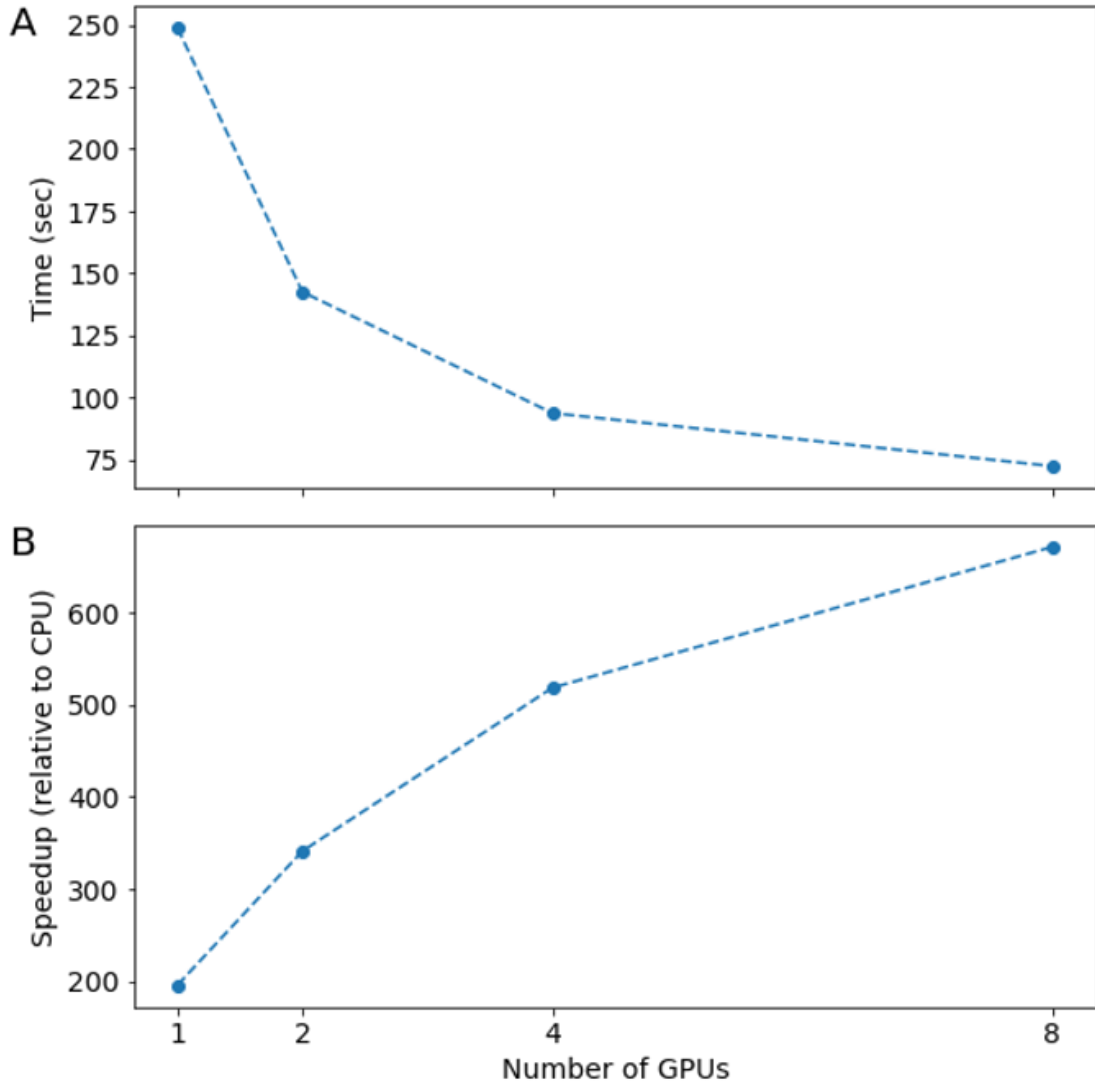


Figure 2.9: GPU streamline generation speedup compared to CPU

For the same task (HARDI data, 27 seeds per WM voxel) tractography duration decreases with the number of GPUs available. Speedup relative to CPU ranges from approximately 200-fold, with one GPU to almost 700-fold with 8 GPUs.

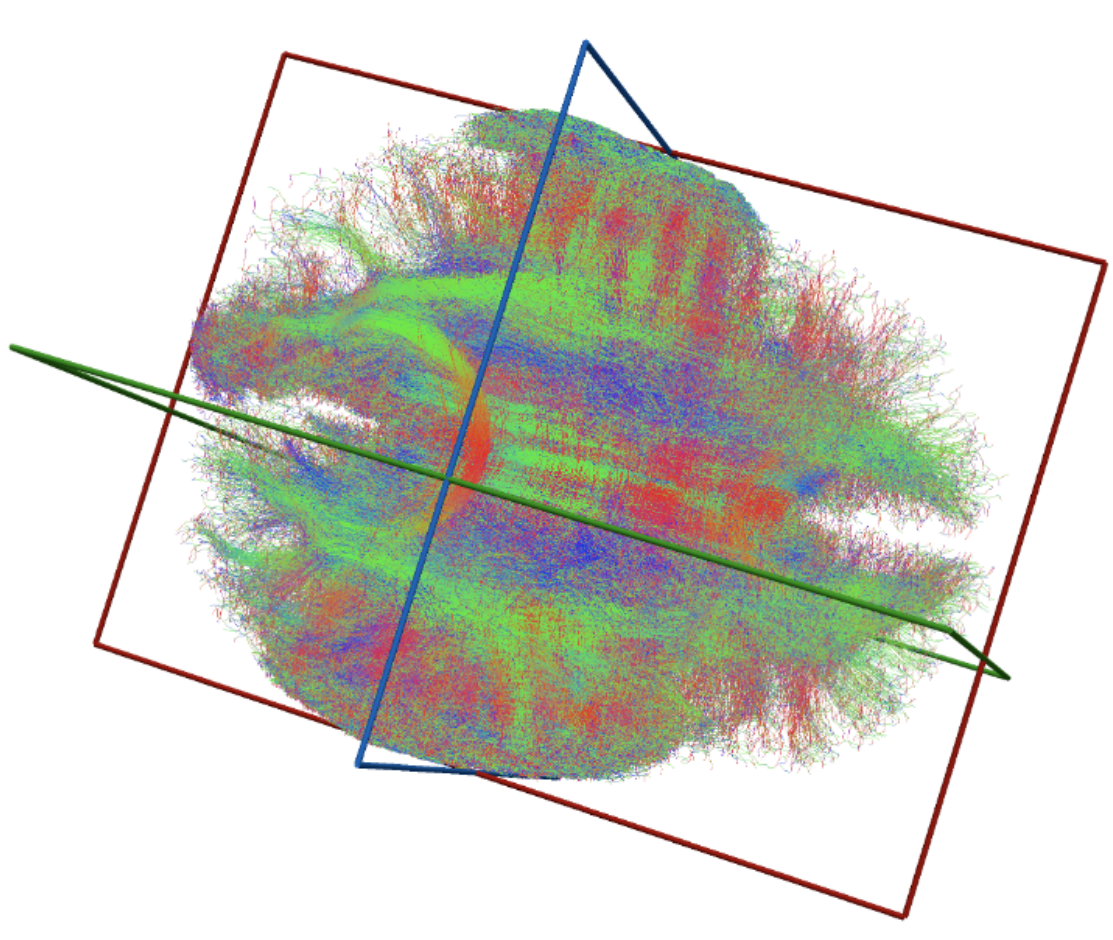


Figure 2.10: Visualization of GPU generated streamlines.

GPU-accelerated tractography of high-resolution data, acquired at 0.625 mm^3 effective resolution. This is a small subset sampled randomly for visualization purposes: approximately 8M streamlines of the 150M streamlines tracked.

standard and high-resolution measurements. Thus, this GPU-based implementation allows researchers to both (1) save time and money solving existing problem sizes and (2) solve new problems that are computationally intractable on CPU-only resources. Open-source software is provided, as well as a docker container that encapsulates the software, together with all of its dependencies available at docker.pkg.github.com/dipy/gpustreamlines/gpustreamlines.

CHAPTER 3

WHOLE BRAIN NETWORK NEURAL MASS MODELS: A CRITICISM

3.1 Introduction

Computational models in neuroscience has advanced to untangle observed neural signals at the macroscopic scale, with fMRI being the most common modality for model based approaches to decipher complex neural mechanisms [161]). As nonlinear behavior is inevitably encountered at the microscopic scale of individual neurons, neural mass models (NMMs) have emerged as a powerful approach to balance interpretability and biological relevance of computational models. Such models summarizes the state of locally interacting neuron populations with few parameters and a conversion from mean excitation level to mean population response [162]. The conversion is typically performed via a nonlinear sigmoid function, whereas the mean firing rates, connection profiles, and membrane potentials are parameterized mathematically to model the lumped activity of particular brain regions[163, 164, 165]. The Wilson-Cowan single oscillator model [16] have evolved into a family of macroscopic NMMs in recent literature; with derivations for neocortical dynamics [166], controllability of brain networks [167], biomarkers in disease [168], and second order statistics of observed brain signals [15, 169, 170, 171, 172].

In a rare occurrence of public introspection amongst computational neuroscientists, Wilson and Niv's work [161] questioned whether model fitting is necessary for model-based analysis of fMRI. They addressed the weakness of models having free parameters, and the results of the analysis depend on how free parameters are set. While their work was limited to the context of rein-

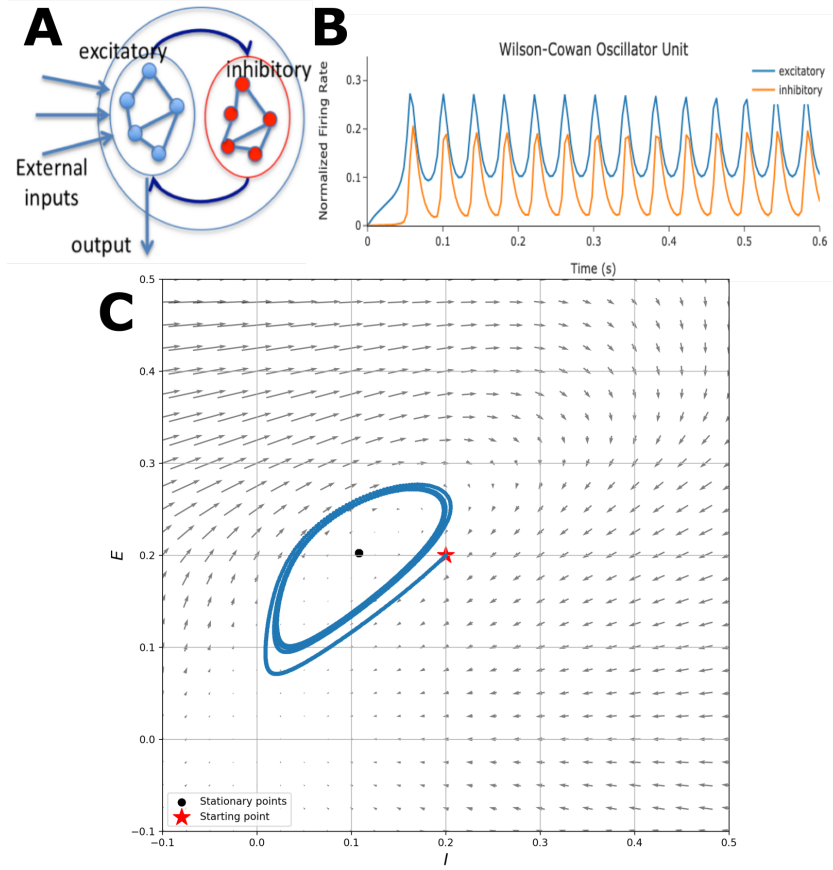


Figure 3.1: Illustration of a Wilson-Cowan oscillator unit.

A: Local excitatory-inhibitory subpopulation structure with long range excitation only to the excitatory population. **B:** Oscillatory time course with default parameter settings as listed in Table 3.2, showing inhibitory population slightly lagging behind excitatory activity. **C:** Numerical simulation showing that the model is a single frequency oscillator, and at the current parameter regime, there exists a limit cycle stationary point at $E = 0.2$ and $I = 0.1$. The number of stationary points and their behavior is subject to change depending on the initial conditions of the system.

forcement learning and a single learning rate parameter, their conclusion is generalizable to the wider model-based neuroscience field: precise identification of parameters is not always necessary, and it is hard to identify neural correlates with model-based analysis due to sensitivity to parameters. More recently, Hartoyo et al. [173] disseminated the problem of unidentifiability in whole brain models, where different parameters combinations can generate similar model predictions, especially in higher order multi-parameter dynamical systems. It

has long been known that fitting of an unidentifiable model to data results in large uncertainties, out of the 22 unknown parameters from the linearized network model implemented by Hartoyo et al., only one parameter was found to be identifiable when fitted to EEG data. Nonetheless, the computational neuroscience field pushed the limit of neuron population level mean field models and extended them to describe neural activity at the whole brain scale.

Despite the prolific use of NMMs for whole brain model-based analysis, their nonlinear nature leads to difficulties in parameter inference and generalizable decoding of neural mechanisms. The saddle point and Hopf bifurcation behavior of the Wilson-Cowan model are neatly described by the original work of Wilson & Cowan [16], the Virtual Brain [20] and reviewed by Breakspear [44]. Such nonlinear systems are silent or in steady-state for most parameter regimes, but interesting oscillating behavior is observed when network coupling or external driving force parameters push the system over the Hopf bifurcation. During parameter inference, constant switching between regimes and model behavior leads to many local minimas during parameter optimization. To avoid this non-convex problem and parameter identifiability issues, a common practice is to sets all biophysiological parameters for neural subpopulations in a NMM to be near an appropriate Hopf bifurcation point, then one or few global parameters are optimized to second order functional connectivity (FC) metrics such as brain regions pairwise correlation or synchrony [168, 15, 169, 172, 174, 175]. However, this leaves a few problems; What does manually selecting the initial parameter conditions imply about biological mechanisms? How does model optimization perform when inferring more than one global parameter at a time? Does the fMRI FC metric fitting translate well to the encephalography modalities? And finally whether the model parameters optimized for FC metrics translate well to

the frequency spectrum?

The traditional practice of only finding one or two optimal global connectivity related parameters, sometimes by manual grid search(see all works in Table 3.1), while having its merits, is a fault of the high dimensional and nonlinear nature of NMMs. Techniques such as stochastic gradient descent found success in deep learning mainly due to the overparameterization of networks and the theory behind the universal approximation theorem [176, 177]. On the other hand, biophysiological models do not have the luxury of overparameterization, making any gradient descent algorithms difficult to implement for model optimization. In this work, we will investigate and discuss the difficulties faced in gradient descent based approaches to parameter inference, as well as address the shortcomings of current network NMMs. We present a systematic examination of the Wilson-Cowan model. First, we examine the performance of a single Wilson-Cowan oscillator unit when fitting to broad band spectra, and whether MCMC sampling can converge to a reasonable posterior distribution for its parameters. In addition, we do not expect a single oscillator model to be able to capture the properties of an entire MEG frequency spectrum. However, if introducing coupling and delays to identical brain regions creates more dynamical oscillations as suggested by ([15]), then a systematic examination of the new objective function space should be made. We implement the whole brain network Wilson-Cowan model to sample for posteriors that captures whole brain MEG derivatives such as coherence functional connectivity (COH) and amplitude envelope correlation (AEC), with the goal to verify whether the global parameters themselves can capture these metrics well, and whether the inferred parameters for FC produces a biophysiological power spectrum.

Table 3.1: Whole Brain Neural Mass Model Parameter Inference Publications and their performance. This table does not include publications with whole brain mean field models or mechanistic models of neural activity.

Name	Modality	Target	Highest Accuracy
Zimmerman et al. [168]	fMRI	Correlation FC	$r = 0.57$
Honey et al. [175]	fMRI	Correlation FC	$r = 0.48$
Demirtas et al. [174]	fMRI	Correlation FC	$r = 0.743$
Wang et al. [172]	fMRI	Correlation FC	$r = 0.46$
Schirner et al. [178]	fMRI	BOLD Time series	$r = 0.50$
Falcon et al. [179]	fMRI	Correlation FC	$r = 0.29$
Abeysuriya et al. [169]	MEG	Synchrony FC	$r = 0.48$
Deco et al. (2017) [180]	MEG	Envelope FC	$r = 0.45$
Deco et al. (2009) [15]	fMRI	Kuramoto order parameter	Not reported
Hadida et al. [181]	MEG	Envelope FC	$r = 0.42$

3.2 Methods

3.2.1 Experimental Procedure

Study Cohort

We acquired MEG, anatomical MRI, and diffusion MRI for 36 healthy adult subjects (23 males, 13 females; 26 left-handed, 10 right-handed; mean age 21.75 years (range: 7–51 years). All study procedures were approved by the institutional review board at the University of California at San Francisco (UCSF) and are in accordance with the ethics standards of the Helsinki Declaration of 1975 as revised in 2008.

MRI

A 3 Tesla TIM Trio MR scanner (Siemens, Erlangen, Germany) was used to perform MRI using a 32-channel phased-array radiofrequency head coil. High-resolution MRI of each subject's brain was collected using an axial 3D magnetization prepared rapid-acquisition gradient-echo (MPRAGE) T1-weighted sequence (echo time [TE] = 1.64 ms, repetition time [TR] = 2,530 ms, TI = 1,200 ms, flip angle of 7°) with a 256-mm field of view (FOV), and 160 1.0-mm contiguous partitions at a 256×256 matrix. Whole-brain diffusion weighted images were collected at $b = 1000\text{s/mm}^2$ with 30 directions using 2-mm voxel resolution in-plane and through-plane. The T1-weighted images were then parcellated into 68 cortical and 18 subcortical regions using the Desikan-Killiany atlas available in Freesurfer [114, 182], the voxel labels were used to identify modeled dipoles in MEG source Reconstruction.

Structural Connectivity Network

To construct high resolution average connectivity matrices with the same Desikan-Killiany parcellations, we obtained openly available data from the Human Connectome Project [183]. Subject specific structural connectivity was computed using diffusion MRI data: *Bedpostx* was used to determine the orientation of brain fibers in conjunction with *flirt*, as implemented in the FSL software [184]. In order to determine the elements of the adjacency matrix, we performed tractography using *probtrackx2*. We initiated 4,000 streamlines from each seed voxel corresponding to a cortical or subcortical gray matter structure and tracked how many of these streamlines reached a target gray matter structure. The weighted connection between the two structures $c_{j,k}$ was defined as the number

of streamlines initiated by voxels in region j that reach any voxels in region k , normalized by the sum of the source and target region volumes ($c_{j,k} = \frac{\text{streamlines}}{v_j + v_k}$). This normalization prevents large brain regions from having high connectivity simply due to having initiated or received many streamlines.

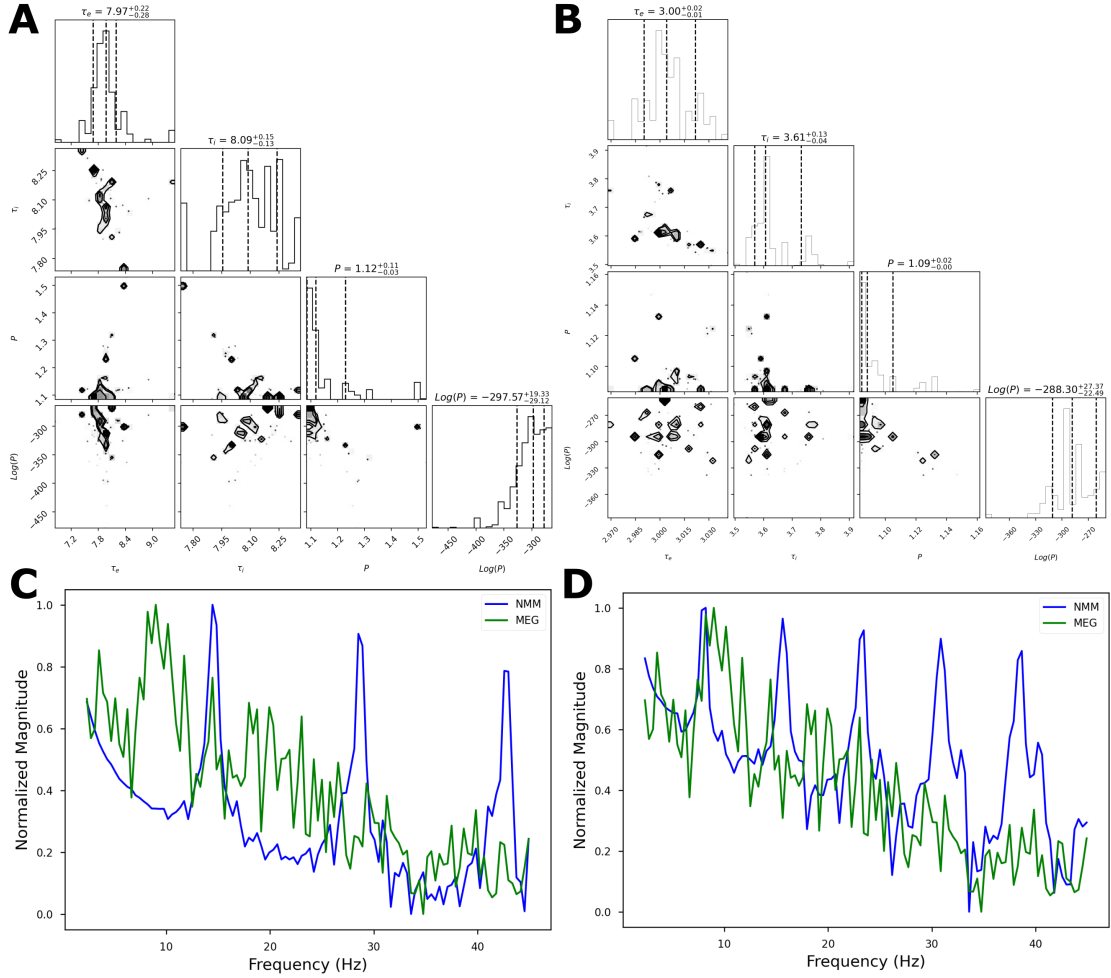


Figure 3.2: MCMC sampling of posterior distribution when maximizing likelihood to average MEG power spectrum.

Corner plot of the posterior marginal distributions for parameters τ_e , τ_i , and P when initiating from default values (A) or Hopf bifurcation point (B). C and D illustrates the average MEG spectrum (green) alongside the oscillator model spectra (blue) simulated with the posterior mean values shown from the corner plots above.

MEG Acquisition and Source Reconstruction

MEG recordings were acquired at UCSF using a 275-channel CTF Omega 2000 whole-head MEG system from VSM MedTech (Coquitlam, BC, Canada). All subjects were instructed to keep their eyes closed for 5 min while their MEGs were recorded at a sampling frequency of 1,200 Hz. Then, all recordings were downsampled to 600 Hz and digitally filtered to remove DC offset and other noisy artifact outside of the 1 to 160Hz bandpass range prior to source reconstructions. To "invert" our sensor space recordings to the MRI voxels, we used an adaptive spatial filtering algorithm from the NUTMEG software tool [185]. To prepare for source localization, all MEG sensor locations were co-registered to each subject's anatomical MRI scans. The lead field (forward model) for each subject was calculated in NUTMEG using a multiple local-spheres head model (three-orientation lead field) and an 8mm voxel grid which generated more than 5,000 dipole sources, all sources were normalized to have a norm of 1. Finally, the MEG recordings were projected into source space using a beamformer spatial filter. Source estimates tend to have a bias towards superficial currents and the estimates are more error-prone when we approach subcortical regions, therefore, only the sources belonging to the 68 cortical regions were selected to be averaged around the centroid.

Functional Connectivity

To analyze static functional connectivity in the MEG data and in the model, we computed both α band coherence (COH) and amplitude envelope correlation (AEC) with MNE Python's connectivity module implementations [186]. First, multi-taper power spectrum densities were computed with digital pro-

late spheroidal sequences (DPSS) windows, and adaptive weights were used to combine the tapered spectra into full power spectral densities (PSDs). Finally for data with estimated cross- and power spectral densities S_{xy} and S_{xx}, S_{yy} , the coherence is given by:

$$COH = \frac{|E[S_{xy}]|}{\sqrt{E[S_{xx}] * E[S_{yy}]}} \quad (3.1)$$

To compute the amplitude envelope correlation, narrow band MEG time courses were obtained by bandpass filtering between 8 and 12 Hz. Hilbert transformed analytic signal corresponding to the orthogonalized narrow band time courses were computed to account for spatial leakage and zero-lag correlations. As recommended by [187, 188, 180], MEG resting-state FC is maximized by solely considering ultra-slow fluctuations of the amplitude envelope. Therefore, a 4th order low-pass Butterworth filter at 0.2Hz is implemented, obtaining an envelope time course with alpha band carrier frequency. Finally, the Pearson correlation between every pair of envelope time courses were computed.

Model Parameter Inference

Statistical sampling is a valuable tool in modern machine learning techniques, with Metropolis-Hastings [189] and Gibbs [190, 191] samplers being the most widely used algorithms. Such algorithms allow marginalization over parameters and find an estimate of the posterior density that is consistent with an observed dataset. The posterior probability function, is taken from Baye's rule and can be written as:

$$p(\theta|y) \propto p(\theta)p(y|\theta) \quad (3.2)$$

Where $p(\theta)$ is the distribution of prior beliefs on our model parameter values and $p(y|\theta)$ is a conditional likelihood probability distribution of observing our data given some set of model parameters θ . To "marginalize" these parameters θ for a posterior probability distribution that is consistent with observed data, we write our conditional likelihood probability as a Gaussian:

$$\log P(y|\theta) = -\frac{1}{2} \sum_n \left[\frac{y_n - f(E_n(t) - I_n(t))}{\sigma_n^2} + \log \sigma_n^2 \right] \quad (3.3)$$

For all parameters θ , we will use uniform ("uninformative") priors for the term $p(\theta)$. In this formulation of MCMC, we are drawing samples from a probability distribution and we want that to be a probability distribution for parameters that produces some outcome $f(E_n(t) - I_n(t))$ which closely resembles the mean and variances of y . Here, we take y and the function f to be one of the MEG derived FC metrics.

Table 3.2: Default parameters for the Wilson-Cowan oscillator model. The excitatory driving force P and time constants τ_e and τ_i are inferred during our experimentation, and their initial values are shown here. All default values are set such that small inputs would cause the system to oscillate (near the Hopf bifurcation point).

Symbol	Physiological Parameter	Value
a_e, a_i	Response function max slope	1.3, 2
θ_e, θ_i	Response function threshold	4, 3.7
c_1, c_2	Excitatory coupling	16, 12
c_3, c_4	Inhibitory coupling	15, 3
r_e, r_i	Refractory periods	1, 1
τ_e, τ_i	Time constants	8 ms
P	External driving force	1.25

3.3 The Wilson-Cowan Local Oscillator Model

The original derivation of the single oscillator Wilson-Cowan model is illustrated in [16], which observed cycles of excitation and inhibition producing oscillations typically seen observed in neural activity. Variants of this model has been implemented in several works, notably in ([15]) with an extremely simplified model, to highlight the importance of delays and coupling in the brain.

For local oscillations, two subpopulation of neurons are considered: an excitatory subpopulation (E) driving towards increased oscillatory activity, and an inhibitory subpopulation (I) driving towards quiescence. Given static local subpopulation couplings, varying firing amongst the two subpopulation of neurons, and an external driving force controlling the excitation, the model is able to describe the mean temporal dynamics of a mean field of neurons. Additionally, Wilson & Cowan introduced "response functions" where local firing-thresholds within each subpopulation control the response of initially quiescent neurons to excitation, they are modeled as sigmoidal functions:

$$S(x) = \frac{1}{1 + e^{-a(x-\theta)}} - \frac{1}{1 + e^{a\theta}} \quad (3.4)$$

Where a and θ are parameters detailing the sigmoidal response function's maximum slope and the position of maximum slope respectively. Finally, with $E(t)$ and $I(t)$ representing the ratio of neurons firing for the two subpopulations respectively, the original Wilson-Cowan model is defined as:

$$\tau_e \frac{dE_j(t)}{dt} = -E_j(t) + (1 - r_e E_j(t)) S_e(c_1 E_j(t) - c_2 I_j(t) + P) + \epsilon_j(t) \quad (3.5)$$

$$\tau_i \frac{dI_j(t)}{dt} = -I_j(t) + (1 - r_i I_j(t)) S_i(c_3 E_j(t) - c_4 I_j(t)) + \epsilon_j(t) \quad (3.6)$$

Where τ_e and τ_i are time constants, the length of the refractory periods are parameterized by r_e and r_i , $c_{1,2,3,4}$ are parameters representing the strength of excitatory-excitatory, inhibitory-excitatory, excitatory-inhibitory, and inhibitory-inhibitory connections respectively. $\epsilon_j(t)$ is the Gaussian noise, following Muldoon et al. [167], the noise is scaled by 0.00001 to ensure accuracy in step-wise integration of the differential equations. Lastly, P is the external driving force pushing neurons out of quiescence. In this formulation, the time constants τ_e and τ_i together with the external drive parameter P controls the Hopf bifurcation point of this model, and all local connection strengths are held constant during inference. A summary of all model parameters is listed in Table 3.2 and the model's time course and stationary points are illustrated in Figure 3.1, the parameter settings listed here is consistent with the limit cycle settings as published originally by Wilson & Cowan [16] and the network controllability work by Muldoon et al. [167].

3.4 Oscillator Model Performance

Figure 3.2 shows the oscillator model solutions sampled based on MCMC's walkers and maximum likelihood estimations. Here, we only focused on the three parameters affecting oscillatory frequency and Hopf bifurcation point, and

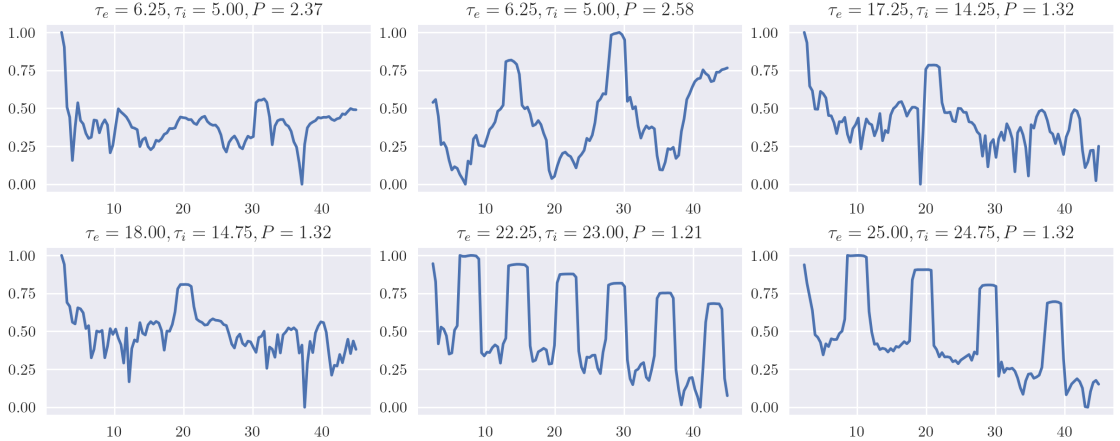


Figure 3.3: Exhaustive grid search of the local oscillator model.

Parameters affecting Hopf bifurcation point and oscillatory frequency were iteratively computed over a 3-dimensional grid to look for an optimal solution that matches closely with the observed average MEG spectra.

implemented non-informative flat priors and arrived at posterior distributions that are moderately constrained by the observed average MEG spectrum. We initiated our samplers under two conditions: default parameter values as described in [167] ($\tau_{e/i} = 8$ and $P = 1.25$) or near a 10Hz oscillatory Hopf bifurcation point ($\tau_e = 3.0$, $\tau_i = 3.6$, and $P = 1.1$). Under both scenarios, we see high uncertainty for both τ_i and P , despite τ_e having a narrower distribution, the samplers for both τ_e and τ_i did not accept parameters far away from their initial positions. Moreover, τ_i seems to have more than one highly probable value. Using the posterior means as model parameter inputs, the simulation produced a power spectrum with 15Hz peak and subsequent harmonic peaks at 30 and 45 Hz when initiated from default values. While the most notable peak in a human MEG spectrum is the alpha peak around 10Hz, the likelihood maximization mechanism arrived at a solution that captured the 10Hz alpha peak only when initiated near a 10Hz oscillatory regime. We will discuss the question of MCMC sampler convergence in the discussion section.

States of quietness, transience, steady-state, and limit cycle in dynamical systems used by NMMs are clearly illustrated and reviewed in ([44]) and ([20]), where small changes in model parameters or initial conditions can affect the behavior of the model output. Due to these changes in model behavior, it is extremely easy for our samplers to be stuck in a certain regime and reject samples that are outside of the preset limit cycle regime as set by default parameters. Figure 3.3 shows the 6 most closely matching spectras found by exhaustive grid search. These results suggest that there exists sets of parameters that can produce oscillations at any of the notable frequency peaks, but also bringing into question the problem of identifiability. We see two sets of parameters producing notable peaks at 20Hz, and a set of parameter producing a 15Hz oscillation that is different from the set obtained from MCMC sampling.

A broad band frequency spectrum, however, has both a periodic and aperiodic component ($\frac{1}{f}$ -like fall off), and interpretations of physiological spectrum can be compromised by periodic features mixed with offsets and exponential components that do not contribute to frequency specific feataures [192]. Paired with the fact that our oscillator model can only produce one principle frequency of oscillation, we implemented the *FOOOF* algorithm from Donoghue et al. [192] to obtain a periodic frequency power spectrum. Figure 3.4 shows the same posterior sampling procedure's results when maximizing likelihood to a periodic component only spectrum, and the bottom panels show both the average MEG and model simulated spectrum without the aperiodic component. In this new maximum likelihood space and sampling from the same initial starting ranges, we see that the samplers were able to explore much wider parameter ranges and did not get stuck in the initial regime. However, the uncertainties around the posterior means is still large, and parameters τ_i and P even shows hints of

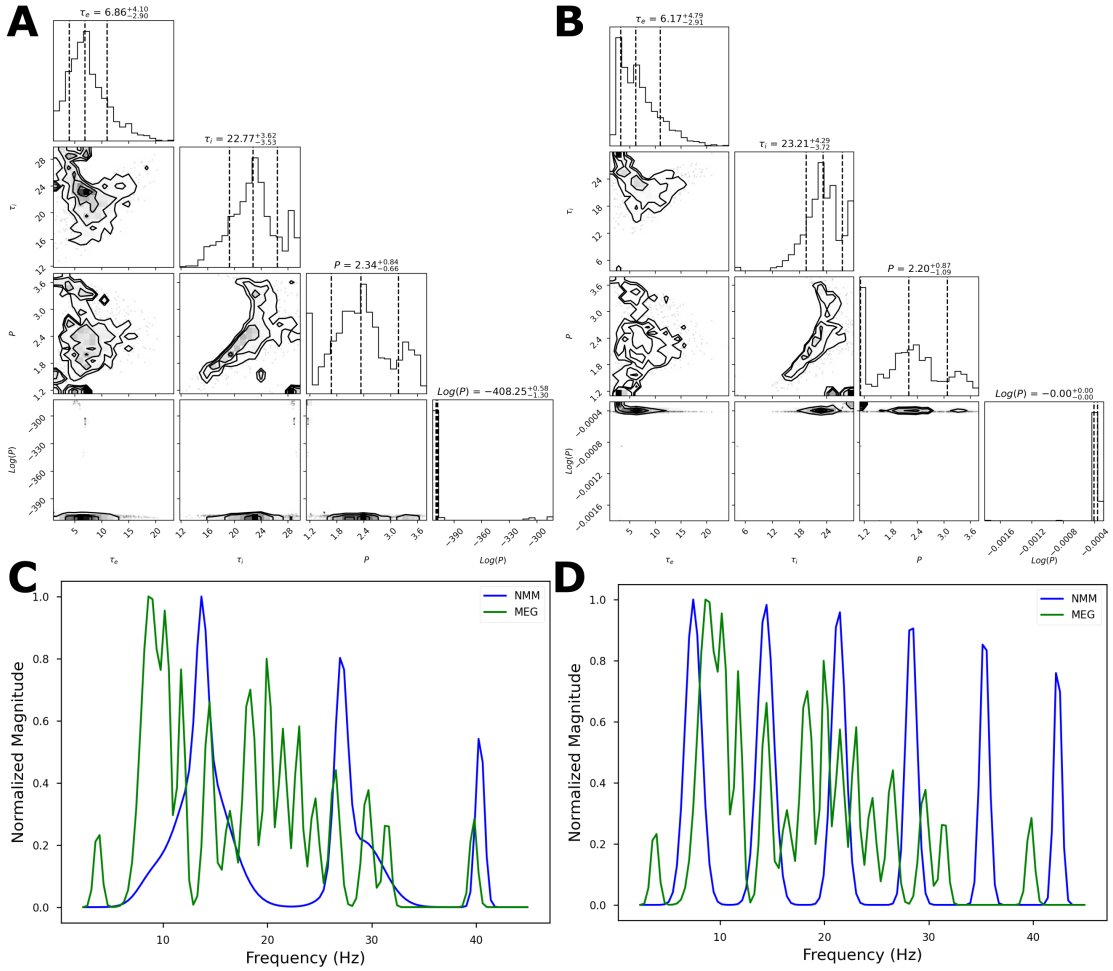


Figure 3.4: MCMC sampling of posterior distribution when maximizing likelihood to average periodic power spectrum.

Corner plot of the posterior marginal distributions for parameters τ_e , τ_i , and P when initiating from default values (A) or Hopf bifurcation point (B). C and D illustrates the average MEG spectrum (green) alongside the oscillator model spectra (blue) simulated with the posterior mean values shown from the corner plots above.

bimodal distributions. Lastly, despite a smoother surface for the samplers, the final posterior means did not produce a spectra that closely matched with the most notable frequency peaks in the observed MEG spectrum for both initial conditions.

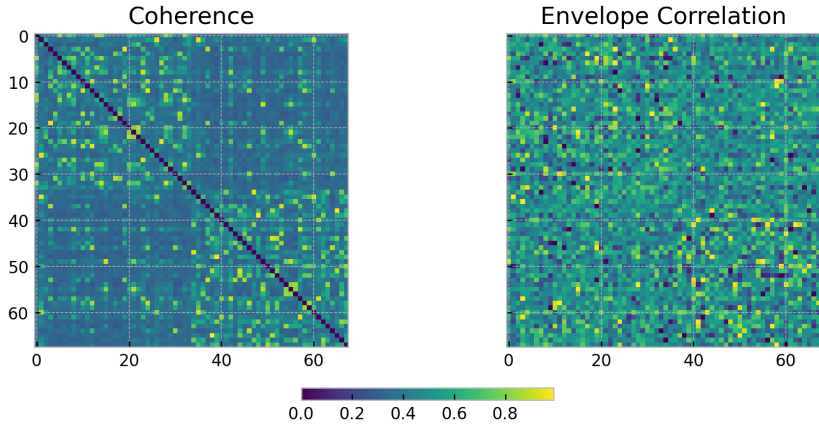


Figure 3.5: Source localized MEG functional connectivity matrices.

MEG recordings were source localized and averaged to each cortical brain region as parcellated by the Desikan-Killiany atlas [182], α band coherence matrix of pairwise cortical brain regions showing hemispheric block structure is on the left, and narrowband amplitude envelope correlation matrix showing weaker hemispheric block structure is on the right.

3.5 Network Extension of Wilson-Cowan Model

The oscillator model is a single frequency oscillator model, to extend this to the whole brain network, we are simply saying the broadband oscillations we observe in encephalography recordings are fully dependent on the reverberant properties in the long range white matter connections. On the macroscopic whole brain scale, the excitatory neuronal population receives delayed signals from interconnected regions via white matter streamlines and coupling terms, thus extending the original oscillator model to a network of j brain nodes coupled by a connectivity matrix A :

$$\tau_e \frac{dE_j(t)}{dt} = -E_j(t) + (1 - r_e E_j(t)) S_e(c_1 E_j(t) - c_2 I_j(t) + c_5 \sum_k A_{jk} E_k(t - \tau_d^k) + P) + \epsilon_j(t) \quad (3.7)$$

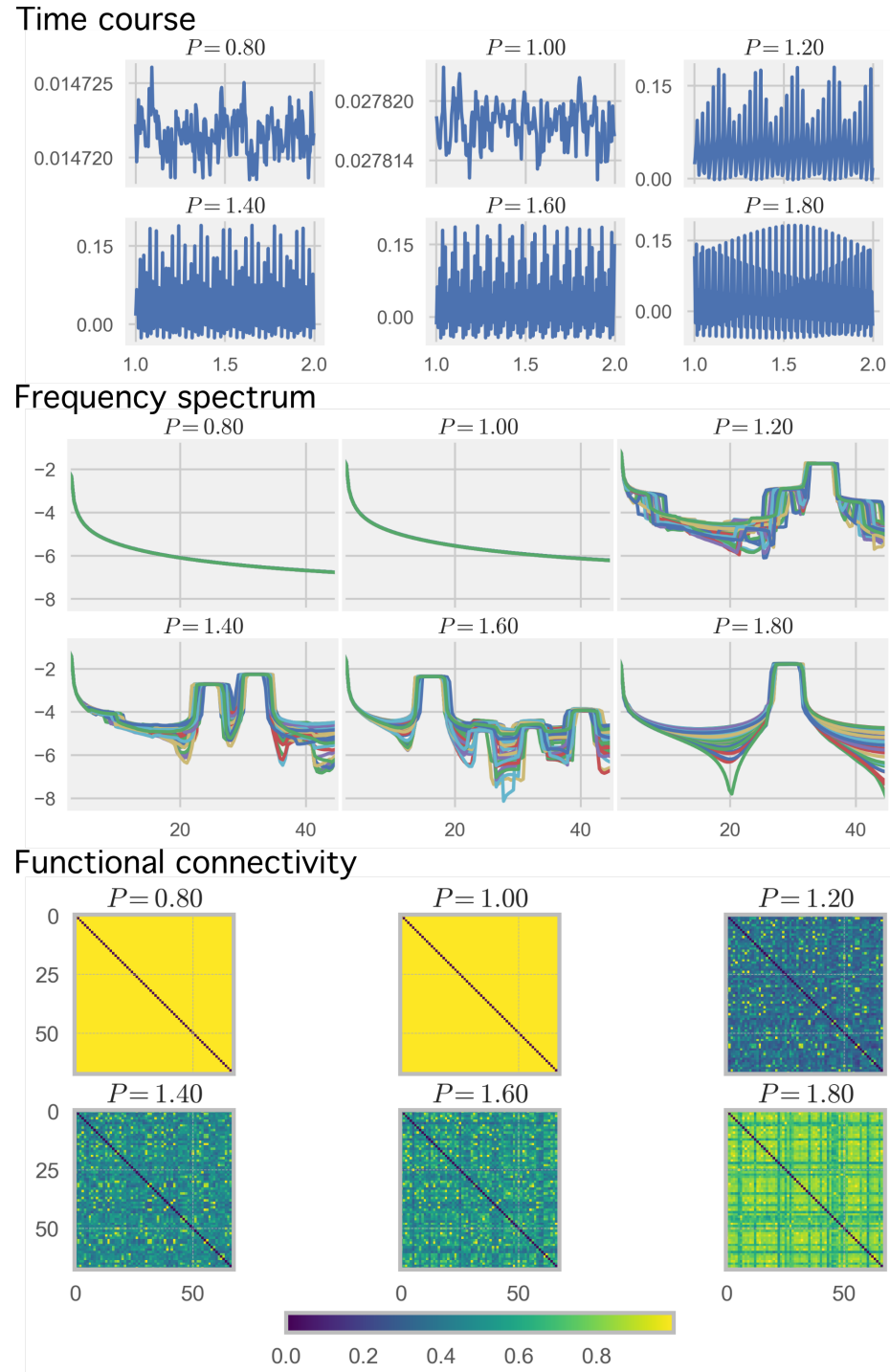


Figure 3.6: Network model behavior in response to external driving force

Panels showing network model's time course, frequency spectrum, and coherence functional connectivity from top to bottom with increasing external driving force parameter P . Simulations are performed with default parameter values and $c_5 = 1.5$, the model is dominated by noise at low P , but switches to an oscillatory regime when P crosses the Hopf bifurcation value. The example time course is shown for one brain region only, whereas the frequency spectrum is shown for all brain regions.

$$\tau_i \frac{dI_j(t)}{dt} = -I_j(t) + (1 - r_i I_j(t)) S_i(c_3 E_j(t) - c_4 I_j(t)) + \epsilon_j(t) \quad (3.8)$$

Here, the delay parameter τ_d^k accounts for propagation time between distance brain regions as calculated by white matter streamline distances, which interferes with the dynamics of each node. To oscillate, the model is pushed passed the Hopf bifurcation point by either P or a high enough global coupling strength (c_5). Therefore, like all pre-existing literature, only the global parameters that affect the dynamics in the default local parameter regime are inferred.

In the whole brain network model, the simulation is hindered by the feedback & coupling term at each time step. In [181], this problem was simplified by simulating without noise and an average propagation delay. However, they still encountered quadratic increases in complexity and doubling in computation time. Specifically, at each time step size h , the sum of delay terms in each equation needs to be computed at time t and $t + h$, and interpolated for each substep. This substep size is subject to further decrease if a noise term is introduced to the equations, which further increases the amount of computations necessary for one simulation of the model. Additionally, initialization of delayed nonlinear system of equations is a sensitive operation. Delayed systems require a smooth function for initialization to be defined over $[t_0 - \tau_{max} t_0]$, where t_0 is the initial time and τ_{max} is the largest delay. Additionally, it should itself be a solution of the system, which makes this circular and impossible.

There is no solution to this problem of increasing complexity and initialization, in our simulations, and consistent with prior works [181], we set the initial function to be constant and nodes are initially disconnected from the network for a period of time equal to maximum delay. Additionally in our implementation,

we interpolate past solutions for all unique delays in our network and the full solution with an adaptive-step Runge-Kutta integrator of order 8 [193].

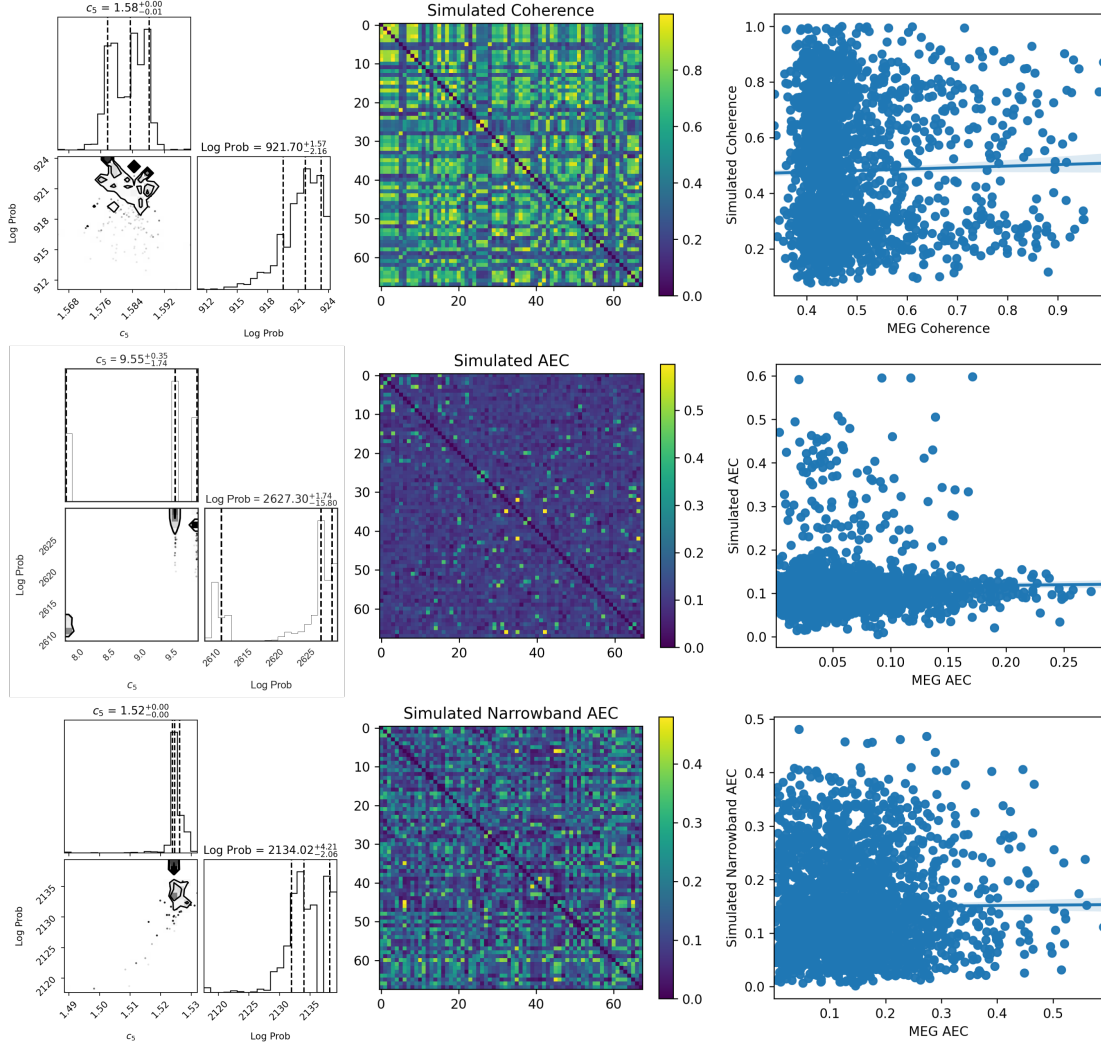


Figure 3.7: Network Wilson Cowan model sampling results for one representative subject.

Top row shows the results for coherence maximum likelihood sampling, broadband AEC sampling in the middle, and bottom row shows the results for narrowband AEC maximum likelihood sampling. Left column shows the sampled posterior distributions for the global coupling parameter c_5 , the middle column shows the network model simulated FC matrices with the posterior mean, and right column shows the scatter plot and linear regression line for the FC matrix entries. Both parameter posteriors achieved near zero slope for the linear fit.

3.5.1 Network Model Performance

Existing literatures expanding neural mass models to the network level fixes the local within population connection strength parameters (in this case c_1 , c_2 , c_3 , and c_4) for all nodes in the network. Meaning all oscillators at every node of the network are identical, the only thing differentiating and producing varying dynamics is driven by the connection properties. In particular, the connection strengths scaling each node's output, the delayed inputs to each node, and the noise being propagated throughout the network can augment oscillatory activity at each node. For fMRI modeling, a Balloon-Windkessel hemodynamic model [194, 195] is usually layered on top of the NMMs for parameter optimization (For example, see [168]). On the other hand, encephalography based modeling wraps another metric on top of the NMM outputs, such as kuramoto coupling parameters in [15]. Here, we examine purely the NMM outputs and whether they are good basis for network modeling. We fixed the time constants τ_e and τ_i so that each oscillator has a base oscillating frequency of near 10Hz, and we fixed $P = 1.1$ to be right below the Hopf bifurcation point so the network's dynamics is purely driven by connectivity.

Figure 3.5 shows the source localized MEG derived metrics for the cortical regions parcellated according to the Desikan-Killiany atlas [182]. Coherence is a purely spectral content based second order statistic, whereas AEC is a time course transformation based correlation metric. These two FC metrics covers both aspects of a neural time series recording; synchrony and delayed correlations between connected regions. Here we focus on the α band coherence and AEC between 8Hz and 12Hz, showing hemispheric block structure, where intra-hemispheric regions experience high coherence while inter-hemispheric regions

experience low coherence. Before sampling the network model's parameters, we examined the effect of P on network dynamics shown in Figure 3.6, here all other parameters are held in their default values while P drove the system from pure noise to oscillating signals, changing the dominant oscillatory frequency and coherence FC patterns as P shifted. Interestingly, the FC matrices became over-saturated if the value of P deviated far from the default operating range ($P = 1.25$).

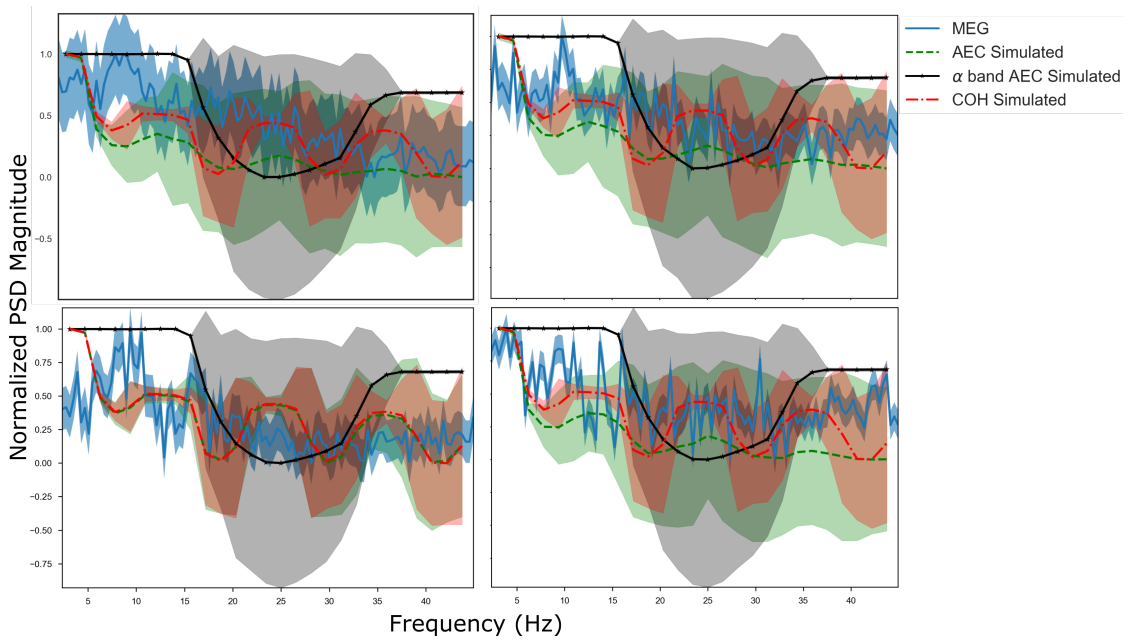


Figure 3.8: Comparison between MEG spectra and network model simulated spectra for 4 subjects.

Model simulated spectra were computed with the posterior mean for global coupling parameter c_5 after MCMC sampling. The average spectra from all cortical brain regions is shown as lines, and the standard deviation summarized from all regions is shown as shaded fillings. Source localized MEG spectra is shown in blue, coherence parameter simulated spectra is shown in red, narrowband and broadband AEC parameter simulated spectra are shown in black and green respectively. All spectras were normalized by their minimum and maximum values to be between 0 and 1 for equal visualization scale.

We first sampled only the global coupling parameter c_5 's posterior distribution with MCMC. Figure 3.7 shows the posteriors for likelihood functions attempting to maximize both COH (top) and AEC (middle, bottom). While both

sampling attempts arrived at posteriors with relatively low certainty, the resulting FC metrics do not fit well with observed MEG derived FC. The simulated coherence FC did not preserve the hemispheric block structure, and lost the sparsity we saw in Figure 3.5’s coherence FC. On the other hand, both narrowband and broadband AEC preserved the sparsity but did not perform well in terms of correlation as shown by the scatter plot.

At its essence, FC matrices are second order statistics computed from time course activity over time, whether recordings like MEG or simulated activity with our network NMM. And here we see that changing the maximum likelihood definition or objective function in parameter inference drastically affects the gradients and eventual posterior parameter values. For modeling based analysis to claim its parameters describe the full relationship between some phenomenon and brain activity, we believe the model needs to encapsulate both first order statistics as well as its second order metrics. In Figure 3.8, we show the MEG spectra in comparison to the model spectra simulated with posterior parameter means obtained by attempting to match both COH and AEC. We see that introducing a connectome with delays and noise to the model did expand the oscillatory repertoire of the oscillators, and because we fixated our time constants to produce oscillations of 10Hz, the resulting spectra with newly sampled global coupling parameter also produces spectra with an alpha peak. Interestingly, narrowband AEC samplers were consistently stuck around $c_5 \approx 1.5$, and produced nearly identical spectra with oscillations in the β range only. On the other hand, other simulated spectra are not able to produce an isolated β peak near 20Hz, which is also a significant characteristic of a human brain signal power spectrum. Furthermore, Figure 3.8 shows that c_5 sampling of the network model only arrived at two different ranges of posterior means when fitting to

FC; Coherence and narrowband AEC fitting led to a lower estimated global coupling value, $c_5 \approx 1.6$ produced nearly identical spectra with narrow variance and a leading spectral peak around 10Hz whereas $c_5 \approx 1.5$ produced the black colored spectra with oscillations around 25Hz. Secondly, fitting to AEC (green) led to a higher estimated global coupling of $c_5 \approx 9$, as illustrated by the widely varying green spectra at lower magnitude. However, one subject (lower left) fell into a minima near $c_5 \approx 1.6$ when fitting to AEC, thus producing an identical spectrum to COH fitting, underlining the issue of parameter unidentifiability and unfriendly landscape of model fitting.

Next, in contradiction to what's commonly done in the field, we initialize all global parameters τ_{ae} , τ_i , P , and c_5 for MCMC sampling. We wanted to see if increasing the dimensionality of the parameter space can improve model performance. Additionally, we set the initial conditions for each τ_e and τ_i samplers to be 8ms with a small random noise, this way, the model is initialized away from an optimal limit cycle regime. In this new initialization parameter regime, the network model produces a uniform 20Hz oscillatory at every node. We want to check if the MCMC samplers can find parameter posteriors that are in the appropriate oscillatory regime as opposed to being stuck traversing between oscillatory, quiescence, and transience activity regimes.

Figure 3.9 and Figure 3.10 illustrates the sampler's inability to survey the 4 dimensional parameter space set by the network model for alpha band coherence or AEC. In Figure 3.9, neither τ_e or τ_i samplers escaped their initial positions near 8ms, and the samplers were stuck between a few acceptable ranges. Additionally, global coupling parameter c_5 and external driving force P had high uncertainties as well. As mentioned above, the initialization parameters puts the model into

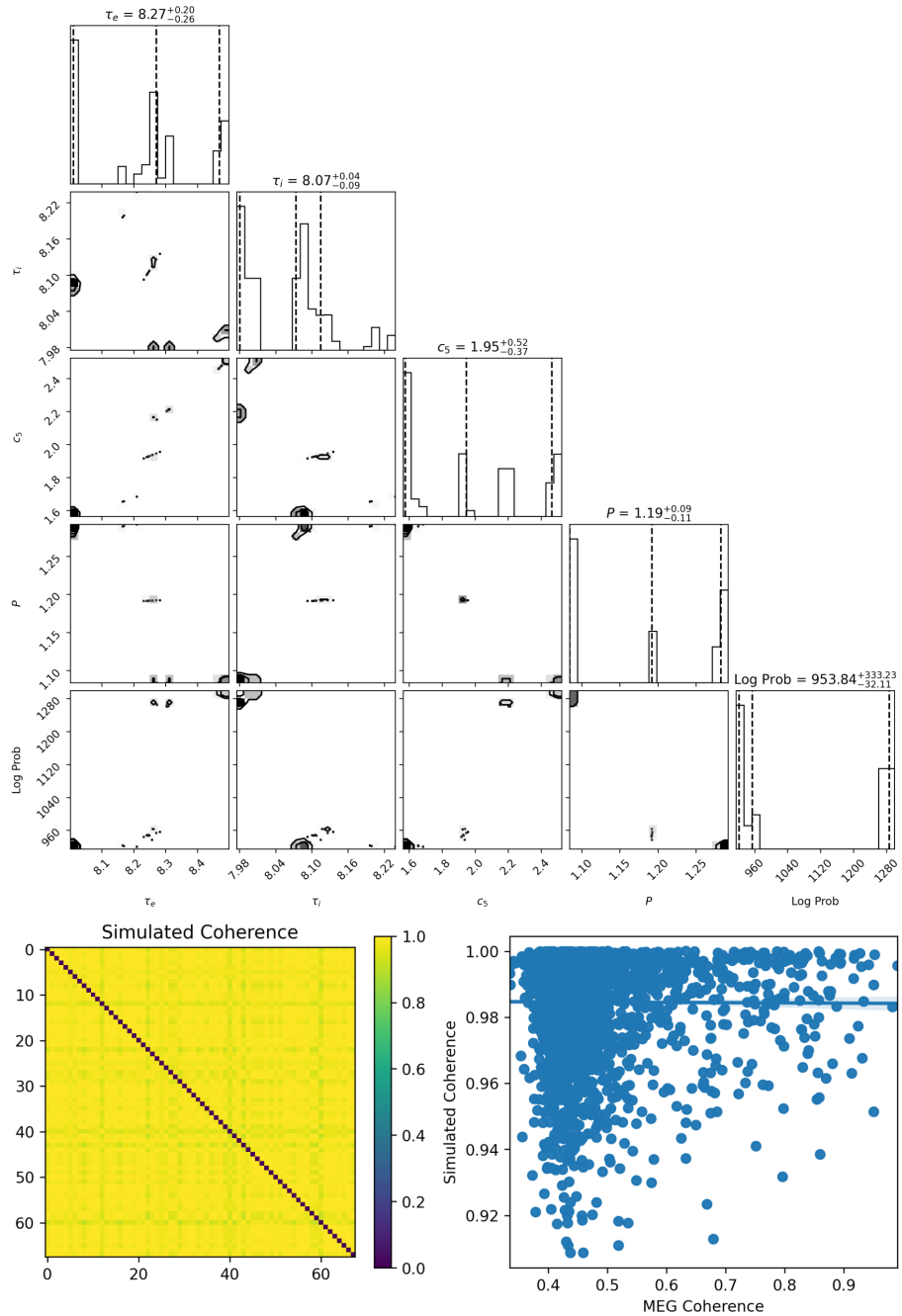


Figure 3.9: Global Parameters Sampling for maximizing likelihood to α band coherence.

Corner plot constructed after MCMC sampling for 50000 steps. The first 5000 steps were discarded and final posterior distribution shown were thinned by half. Neither τ_e or τ_i deviated far from the initial positions, and there is high uncertainty around c_5 and P . Bottom row shows the model simulated coherence with resulting posterior means and the scatter plot against MEG coherence with linear fit for the coherence matrix entries showing no correlation at all.

a 20Hz oscillatory regime, and despite an objective function set for likelihood of the α band, the samplers were not able to arrive at a viable solution for α band coherence. The simulated coherence shown in Figure 3.9 in combination with the spectra shown in Figure 3.11 shows that there was no oscillations or variability near 10Hz. Additionally, not only were the samplers stuck in the initial parameter ranges of producing a 20Hz oscillation, one subject (lower right) transitioned into a transient state with no oscillatory activity.

Similarly, Figure 3.10 shows the same failure of samplers escaping its initial positions. However, in this case, the posterior distributions for all parameters had extremely narrow 95% confidence intervals. Additionally, we do not see these posteriors having more than one frequently visited value as compared to coherence and Figure 3.9. Despite this certainty, the simulated AEC matrix had very little to non-significant correlation and linear fit. And the elements of the simulated AEC matrix is much higher than the observed MEG AEC values. This high AEC is an obvious result when taking into account the quiet spectra shown in Figure 3.11, the AEC parameters produced no oscillatory activity in the alpha range and were stuck in the oscillatory regime of the initial parameter conditions near 20Hz. For two of the subjects, the spectra in green showed little to no variability and no obvious speaks, indicating all nodes of the network were in a transient state. Lastly, the spectra produced by parameters sampled for alpha band AEC were also stuck in the initial ranges, producing spectra almost identical to coherence or broadband AEC fits.

Based on the existing literature's avoidance of this parameter fitting procedure for network NMMs, and the fact that we are implementing a barebones approach with no adjustments to the mean firing rate model, we did not expect the network

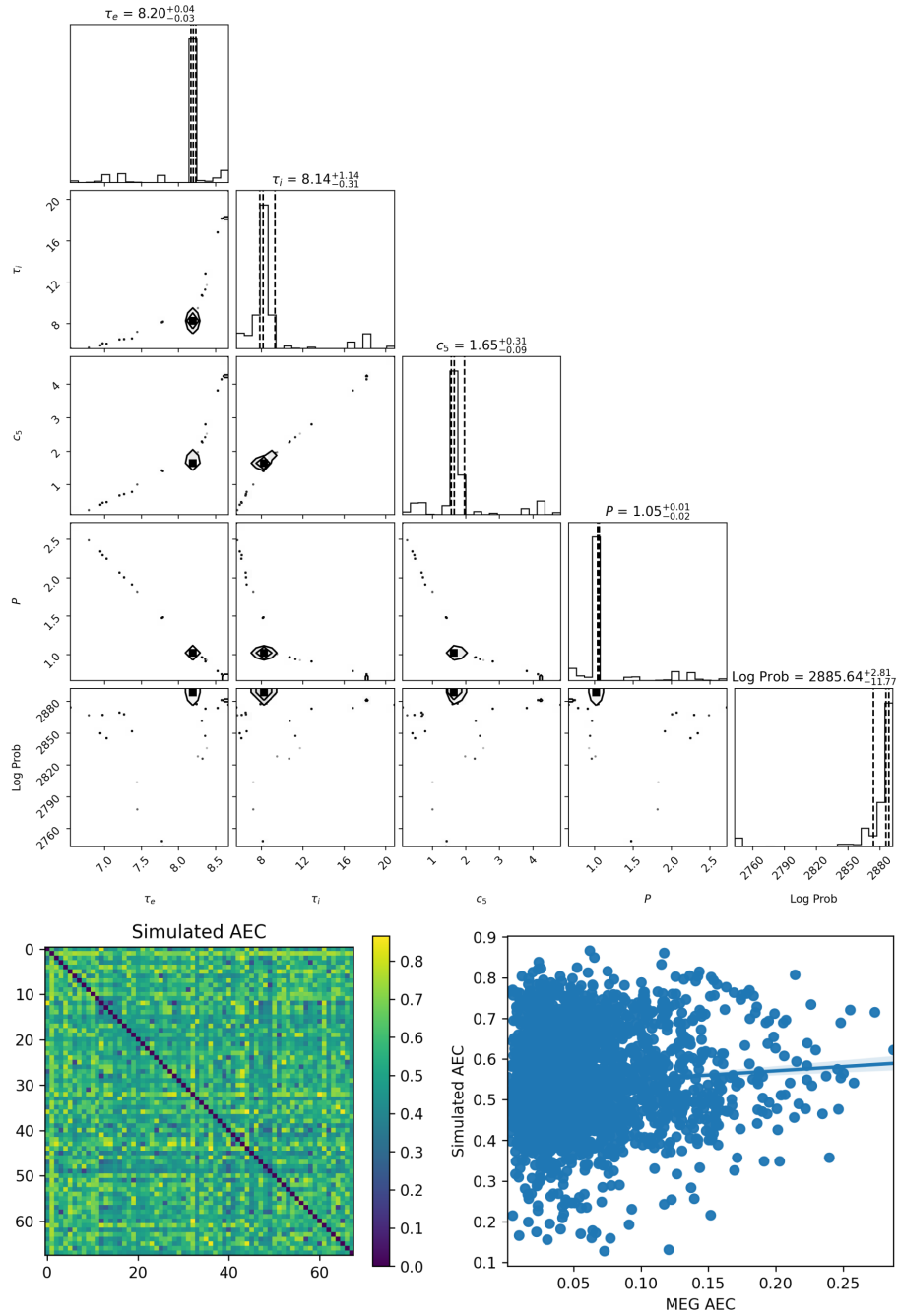


Figure 3.10: Global Parameters Sampling for maximizing likelihood to amplitude envelope correlation.

Corner plot constructed after MCMC sampling for 25000 steps. The first 5000 steps were discarded and final posterior distribution shown were thinned by half. Neither τ_e or τ_i deviated far from the initial positions, but the posterior distributions have narrower confidence intervals as compared to coherence sampling in Figure 3.9. Bottom row shows the model simulated AEC with resulting posterior means and the scatter plot against MEG AEC with linear fit showing a slight correspondence, but different scales.

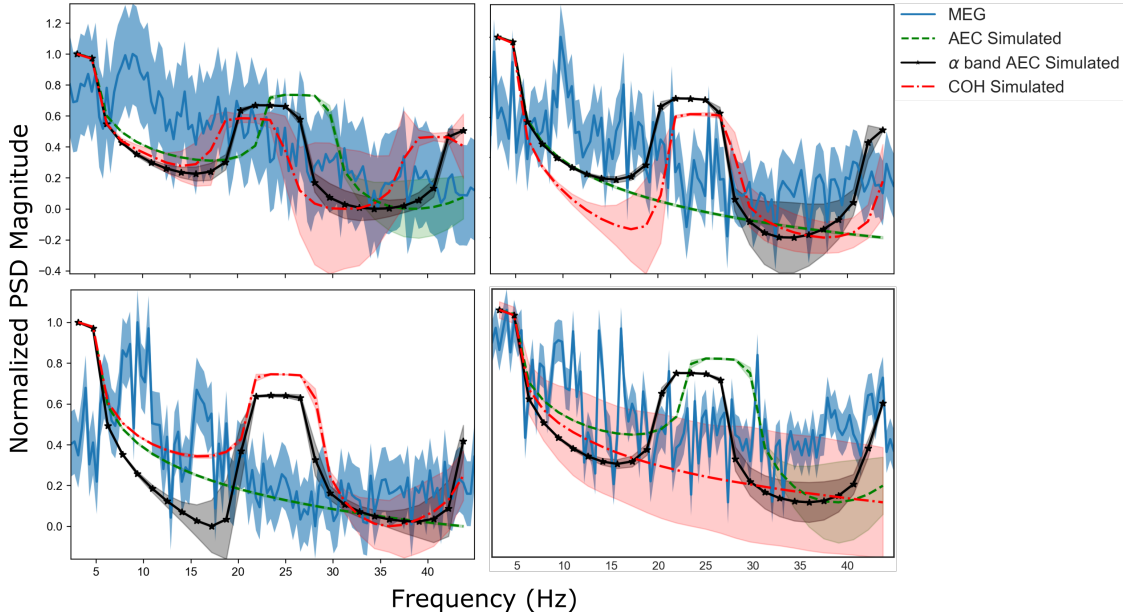


Figure 3.11: Comparison between MEG spectra and posterior mean global parameters simulated spectra for 4 subjects.

Model simulated spectra were computed with the posterior means for τ_e, τ_i, c_5, P after MCMC sampling. The average spectra from all cortical brain regions is shown as lines, and the standard deviation summarized from all regions is shown as shaded fillings. Source localized MEG spectra is shown in blue, coherence parameters simulated spectra is shown in red, narrowband and broadband AEC parameters simulated spectra is shown in black and green respectively. All spectra were normalized by their minimum and maximum values to be between 0 and 1 for equal visualization scale.

NMM to perform well in capturing neural activity statistics. Typically, a more specified model is required to produce any meaningful statistics. We've shown that a typical oscillator unit produces limit cycle activity at a single frequency as specified by the model parameters, and adding a network component to the model does not easily translate to network metrics being produced by the network model. Furthermore, the existing practice of setting model parameters near an oscillatory regime and searching for parameters that fits some neural activity metric well doesn't take into account the problem of unidentifiable parameters. Lastly, network models are high in dimensionality, making parameter posterior sampling a consuming and unpredictable exercise. And by limiting every node

to have identical parameter values to decrease parameter inference complexity is not biologically realistic and produces irrelevant results.

3.5.2 NMM Based Analysis

Parameter inference of a full brain network neural mass model is rarely attempted in the computational neuroscience field. The complexity due to their nonlinearity and network size with numerous delays, combined with the tangled nature of neurological recordings, makes the optimization of these NMMs a nearly impossible task. The first thing we've shown here is that an oscillating Wilson-Cowan neural population has a limit cycle activity for a specific frequency given a specific set of parameters. Extending this model to the network scale by introducing delays and connectivity, but fixing all nodes to have identical parameters for computational tractability does not necessarily provide the broadband spectrum that is characteristic of observed encephalography recordings.

In most NMM analysis (see Table 3.1), the comparisons are made to fMRI BOLD functional connectivity, which has limited temporal resolution, and recorded neural dynamics are limited to below 1Hz. Whereas NMMs mean firing rate outputs are simulated with millisecond time-steps, to compensate for the mismatch in data type and temporal resolution, a Balloon-Windkessel hemodynamics model [195, 196] is used to transform the model outputs to BOLD signals (For example, see [196, 197]) for functional connectivity comparison. Practically, parameters for the NMM is first fitted either by exhaustive grid search or constrained optimization, followed by another model fitting for the BOLD signal transformation. The two layers or model fitting leads to low interpretabil-

ity of final parameters, and low correlations with high variances in parameter distribution on the group level leads to uncertainties about any result.

In other publications, for the sake of computational tractability, a more simplistic Wilson Cowan model variant with more varied model behavior is used as an alternative (For example, see [15], where an additional Kuramoto coupling parameter is required for spectrum computation). In this model, the sigmoidal activation function is simplified to one term, and its inputs are generalized to include network level driving forces and noise. Bringing into question the meaning behind a nonlinear sub-population neuron activation function for network level inputs. In Muldoon et al.'s work on network controllability [167], the original network model was made to oscillate at 20Hz, and no model fitting was performed, only changes in functional network properties based on a single nodal stimulation with the driving force parameter was measured. Again, based on our results with the same model implementation and identical parameter regimes, a network of identical oscillators will not provide simulated functional network metrics that closely resemble those of a realistic brain. Functional connectivity metrics and network activity will undoubtedly change according to network connections, but the parameters producing the accepted functional outputs may not produce an acceptable spectra. Moreover, it is unclear if there is an optimal parameter regime that is suitable for a given brain state due to parameter unidentifiability issues as discussed by numerous works [173, 198, 199].

Overall, it is no surprise that the promise of personalized diagnosis with model based analysis has been overtaken by the capabilities of deep learning or the analytical efficiencies of linear models [200, 201]. Deep learning neural networks takes advantage of repeated and chained linear regression units with

rectified linear activation units (ReLU) to make extremely fast classifications of data, and it has already been shown to produce high accuracy for biological phenomenon [202, 77]. In this framework, interpolating high dimensional data for a given classification or embedding is made possible by the massive flexibility of layered linear units, and is already superior than any nonlinear NMMs in terms of training speed and prediction power. In fact, finding a global minimum to the massive parameter space of deep neural networks is frowned upon due to generalizability, and training of complex parameter spaces is made efficient by backpropagation of gradients. On the other hand, Linear models such as the works cited above transforms dynamical systems to the Fourier domain and uses structural eigen basis to relate functional patterns to a given structural connectome. These efforts provide models that are low-dimensisonal, hierarchical across spatial scales, and efficient to compute as the analytical models do not require step adaptive integrators. The trade offs over linear and nonlinear macroscopic models was recently examined by Nozari et al. [203], whom also reported on the performance of nonlinear NMMs to fit neurodynamic time course data. In addition to reporting linear models outperforming nonlinear models on the macroscopic scale, their work also commented on the macroscopic brain properties that masks nonlinear dynamics. Together with our results, we believe it is evident that nonlinear NMMs are not the optimal model of choice for model-based macroscopic neurophysiological data analysis.

3.5.3 MCMC Convergence & Other Approaches

In our results, we avoided the topic of convergence for our samplers. Convergence is often a difficult topic to discuss for MCMC sampling based analysis,

because convergence can only be guaranteed for sample statistical problems with a high number of samples. For high dimensional model parameter inference, quality of the sampled posterior is often evaluated by acceptance ratio of samples and inspection of the posterior as compared to the prior. Additionally, statistics like the Gelman-Rubin statistic [204] are not applicable to modern MCMC algorithms as the multi-samplers used for parallelization are not independent from each other. On the other hand, integrated autocorrelation time [205] quantifies the effective number of independent samples needed and sampler efficiency. However, our sampling chains for all scenarios produced high acceptance rates and integrated autocorrelation times that required extremely large amounts of MCMC samples and weeks long computation times. This implies that the log likelihood ratios conditioning our parameter inference problem is not sufficiently exploring the entirety of the parameter space. Our resulting weak fits with the fact that majority of accepted samples have low likelihoods suggest global sampling methods are not the proper approach for NMM parameter optimization. Secondly, the Wilson-Cowan network model parameters are not capable of describing the high dimensional features of functional neural recordings.

One may suggest that global parameter optimization methods with multiple local searches may improve our model fits. Approaches such as simulated annealing [206] or basin hopping [207] may arrive at inferred parameters that provide better fits, but has their short comings. Firstly, these approaches provide point estimates of model parameters, ignoring any uncertainty in the case of complex parameter spaces that may have more than one possible solutions. In addition, while convergence for these algorithms can be determined by consecutive visits to the current optimal solution, the solution is still sensitive to initialization, and there is no formal way of selecting optimization hyper-parameters such as

tolerances, iterations, temperature, or cooling schedule (exploration scheme). Furthermore, these approaches do not provide any formalism for an objective function, and does not have the advantage of using a Bayesian framework which provides a set framework and a model evidence metric.

3.5.4 Dynamic Causal Modeling

One popular model based analysis is dynamic causal modeling (DCM), these approaches focus on discovery of effective network connectivity, and the emphasis is placed on a few nodes of interest [208]. Typically used for determining causality in fMRI data, this method aims to find the causal network that best supports the observed data as measured by Bayesian model evidence [209]. While the goal of DCM based studies are different from model based analysis of neural recordings, the insights gained from causality in small subnetworks of the brain with a formal framework is extremely valuable. However, this approach is made impractical for whole brain studies due to the number of evaluations and possible networks required to be considered. Furthermore, in the case of NMMs, the nonlinear nature of the model makes the model inversion problem extremely inefficient. Whereas DCM works typically takes advantage of fully connected network models that are easily invertable.

3.5.5 Variational Inference

Variational inference is a statistical method used to approximate parameter posterior densities in Bayesian models, where parameters and their uncertain-

ties are obtained through optimization rather than expensive sampling. The optimization is theoretically performed based on the gradients of a posterior distribution obtained through Baye’s theorem. However, the partial derivatives culminating in the full parameter space gradient is intractable for macroscopic network NMMs, and current implementations of variational inference such as *Edward2* [210] and *PyMC3* [211] uses a “black box” inference approach. While these approaches seem effective for simpler problems, the need to fully sample the posterior hinders the usage of these tools for network NMMs. In particular, a network model such as the Wilson Cowan model requires the integration of two sets of derivatives for every brain region. And additionally for each brain region, the algorithm is required to remember past solutions at all nodes, and interpolate the past solutions based on unique distance induced delays as assigned by the connectomes. This makes computation of one realization with minimal time steps extremely slow on CPU backends (several minutes), needing to sample thousands of solutions for the likelihood estimation per iteration is simply impossible when taking into account computing time. Moreover, efficient parameter optimization relies on convex structural properties of the problem to guarantee rapid convergence to a solution. But in the case of NMMs and their black-box objective functions, these properties cannot be theoretically determined. In our case of expensive objective functions, the strategy needs to restrict the exploration of the search space to remain computationally tractable, further crippling network model based approaches to exploring neural data.

3.5.6 Challenges and Limitations

We've already addressed the problem of MCMC requiring large numbers of samples for diversity and statistical validity, which is computationally expensive and often times not practical to achieve with network scale NMMs. To further add to the challenges, reliable estimations of functional connectivity maps require on the order of a minute worth of data. This finite data problem in source localized encephalography recordings is comprehensively explored by Sommariva et al. [212], concluding unsurprisingly that estimating functional connectivity is prone to errors with less data. Our numerical network NMM simulations of 2 seconds is on the low end of data length, and is certainly prone to unreliable functional connectivity outputs. This effect is further amplified if initialization of the delayed dynamical systems are not properly selected, as initial values affect the stationary points and stability of the oscillating system. We limited our simulation time to 2 seconds for the simple reason of practical computation time. Numerical integration of NMMs require time-steps below the millisecond to ensure accuracy at every time step. When more uncertainties from delayed inputs and noises at every network node is introduced, the integrators usually takes even smaller time steps, exponentially increasing the time needed to simulate one realization of the NMM. Therefore, parameter exploration poses immediate impossibilities, which is often commented on by published NMM works or avoided by simplifying the problem.

3.5.7 Conclusion

The dimensionality and nonlinearity of network NMMs leads to low confi-

dence for a given system to produce functional dynamics with desired properties, and subsequently compare these models for effective analysis. Additionally, there is no formal methodology for selecting initial values of the delayed dynamics or the initial positions of parameters. In the case of the Wilson-Cowan model, the mean firing rates of neuron sub-populations output is simply not appropriate for encephalography modality data modeling. Recordings of neural activity involves excitation driven currents or blood-oxygen dependent activity, the sensor level average activity we observe in data is not simply explained by firing rate models and more mechanistic details are required. In our work, we show that one of the widely adapted NMMs is specified for neuron population level firing rate studies of a specified frequency, extending such a model to the network scale does not allow accurate, reliable, or efficient optimization. Furthermore, second order connectivity statistics often does not encapsulate sufficient evidence for tuning of network model parameters. Overall, we believe claims of unidentifiable network NMM parameters as low dimensional descriptors of biophysiological data should be carefully examined. More effective alternatives in linear models and deep learning has already surpassed NMMs, and offers more insight into the embeddings of functional brain recordings.

CHAPTER 4

EMERGENCE OF CANONICAL FUNCTIONAL NETWORKS FROM THE STRUCTURAL CONNECTOME

4.1 Introduction

The exploration of structure and function relationships is a fundamental scientific inquiry at all levels of biological organization, and the structure-function relationship of the brain is of immense interest in neuroscience. Attempts at mathematical formulations of neuronal activity began with describing currents traveling through a neuron's membranes and being charged via ion channels [5]. Recently, the focus of computational models have expanded from small populations of neurons to macroscale brain networks, which are now available via diffusion-weighted and functional magnetic resonance imaging (dMRI and fMRI) [213]. Using computational tractography on dMRI images, detailed whole brain white-matter tracts, and their connectivity can be obtained, to yield the brain's structural connectivity (SC). Using correlated activation patterns over time in fMRI data reveals functional connectivity (FC) with high spatial resolution. Such high resolution images of the brain also allowed neuroscientists to label the brain according to anatomical or functional regions of interest (ROIs) [182, 214]. Subsequently, efforts in graph-theoretic modeling have emerged as an effective computational tool to study the brain's SC-FC relationship based on the parcellated brains: ROIs become nodes and connectivity strengths become edges on the graph, while dynamical systems describing neuronal activity are played out on this graph structure [215, 213, 216].

Diverse graph based methods have been employed to relate the brain's

SC to FC. Particularly, perturbations and evolution of the structural and functional networks have been investigated using both graph theoretical statistics [217, 36, 218, 219, 220, 221, 222] as well as network controllability [223, 167]. Structurally informed models use graphical representations of the brain's connections to couple anatomically connected neuronal assemblies [16, 224], numerical simulations of such neural mass models (NMMs) provides an approximation of the brain's local and global activities, and are able to achieve moderate correlation between simulated and empirical FC [225, 226, 165, 175, 227]. However, approximations through stochastic simulations are unable to provide a closed form solution and inherits interpretational challenges since dynamics is only obtained from iterative optimizations of high dimensional NMM parameters.

An emergent field of work have suggested low-dimensional processes involving diffusion or random walks on the structural graph as a simple means of simulating FC from SC. These simpler models are equally if not more successful at simulating fMRI FC patterns [228, 229] as well as MEG oscillatory patterns [230, 231] than conventional NMMs. Lastly, these simpler graph diffusion models, which naturally employ the Laplacian of SC, have been generalized to yield spectral graph models whereby Laplacian eigen-spectra were sufficient to reproduce functional patterns of brain activity, using only a few eigenmodes [232, 229, 231]. Thus, a Laplacian matrix representation of a network can be used to find characteristic properties of the network [233], and its eigenmodes (or spectral basis) are the ortho-normal basis that represent particular patterns on the network. Such spectral graph models are computationally attractive due to low-dimensionality and more interpretable analytical solutions.

The SC's Laplacian eigenmodes are therefore emerging as the substrate on

which functional patterns of the brain are thought to be established via almost any reasonable process of network transmission [232, 229, 234], and metrics quantifying structural eigenmode coupling strength to functional patterns were also recently introduced [235]. These works mainly focused on replicating canonical functional networks (CFNs), which are stable large scale circuits made up of functionally distinct ROIs distributed across the cortex that were extracted by clustering a large fMRI dataset [53]. In [53] seven CFNs (these are spatial patterns, not to be confused for the entire network of graph of the connectome) were identified. Hence recent graph modeling work has attempted to address whether these canonical patterns can emerge by only looking at the structural connectivity information of the brain.

Although spectral graph models have been reasonably successful, they leave several important gaps. First, they accommodate only passive spread, hence are incapable of producing oscillating or traveling phenomena, which are critical properties of brain functional activity. Second, they do not incorporate path delays caused by finite axonal conductance speed of activity propagating through brain networks. Third, they are capable of reproducing only deterministic and steady-state features of empirical brain activity, giving a single predicted FC for a given SC. Hence these models cannot easily explain the substantial variability observed amongst individuals, as well as between different recording session of the same individual. This suggests that simplistic spectral graph models will need to be augmented with a set of richer time- or individual-varying features or parameters in order to make them more realistic. Unfortunately, this is a goal that is at variance with the key attraction of these methods - their parsimony and low-dimensionality.

In this study we propose a novel spectral graph approach that is able to produce a far richer range of functional activity and dynamics without compromising on the simplicity and parsimony of the spectral graph model. We hypothesise that the introduction of realistic path delays and axonal conductance speeds can allow graph spectra to display the kinds of pattern-richness observed in real data. Hence we utilize both the SC connectivity strength matrix as measured by white-matter fiber tract density, as well as the distance matrix as measured by the average white-matter fiber tract distance between pairs of ROIs. We show that the additional distance information allows for examining of network dynamics in the complex domain in terms of a novel complex-valued Laplacian. This approach involves only global model parameters, which between them accommodate a rich diversity of spatiotemporal patterns that are capable of closely reproducing the diversity of spatial patterning seen across a large number of healthy subjects. Through this minimalist complex diffusion model, the characteristic patterns of signal spread described by corresponding complex-valued eigen-spectra can be tuned to exhibit activation patterns resembling human CFNs. We show that the complex approach significantly and consistently exceeds the performance of existing works relating real-valued SC Laplacian's eigen-spectra to measured FC [229, 235, 232, 175]. The introduction of the complex-valued Laplacian and accompanying complex graph diffusion may be an important contribution to the emerging literature on graph models of brain activity, and furthers our understanding of the structure-function relationship in the human brain.

We begin with a general theory of complex graph diffusion incorporating path delays, leading to the emergence of the complex-valued Laplacian. Then we present detailed statistical analysis showing the ability of complex eigenmodes

to be tuned by model parameters and reproducing CFNs. We present comparison with the current approach of using real-valued eigenmodes, followed by a detailed Discussion.

4.2 Theory

Notation. In our notation, vectors and matrices are represented in **bold**, and scalars by normal font. We denote frequency of a signal, in Hertz (Hz), by symbol f , and the corresponding angular frequency as $\omega = 2\pi f$. The structural connectivity matrix is denoted by $\mathbf{C} = c_{l,m}$, consisting of connection strength $c_{l,m}$ between any two pairs of brain regions l and m .

4.2.1 Network Diffusion of Brain Activity

For an undirected, weighted graph representation of the structural network $c_{l,m}$, we model the average neuronal activation rate for the l -th region as $x_l(t)$:

$$\frac{dx_l(t)}{dt} = -\beta(x_l(t) - \alpha \sum_{l \neq m}^m c_{l,m} x_m(t - \tau_{l,m}^\nu)) + p_l(t) \quad (4.1)$$

Where we have a mean firing rate equation at the m -th region controlled by an inverse of the common characteristic time constant β , and input signals from the l -th regions connected to region m are scaled by the connection strengths from $c_{m,l}$ and delayed by $t - \tau_{m,l}^\nu$. The term $\tau_{m,l}^\nu$ is the delay in seconds obtained from the distance adjacency matrix defined by $\tau_{m,l}^\nu = \frac{D_{m,l}}{\nu}$, with ν representing the conductance speed in the brain's SC network. The global coupling parameter α

acts as a controller of weights given to long-range white-matter connections.

The delays between connected brain regions turn into phase shifts in the frequency profiles of the oscillating signals. Thus we obtain the following Fourier transforms from (4.1): $\frac{dx_l(t)}{dt} \rightarrow j\omega X_l(\omega)$, $x(t - \tau_{m,l}^\nu) \rightarrow e^{-j\omega\tau_{m,l}^\nu} X_m(\omega)$, and the oscillatory frequency $\omega = 2\pi f$. Applying the listed Fourier transforms to (4.1) we can obtain the following:

$$j\omega X_l(\omega) = -\beta(X_l(\omega) - \alpha \sum_{m \neq l} c_{m,l} X_m(\omega) \exp -j\omega\tau_{m,l}^\nu) + p_l(\omega) \quad (4.2)$$

We then define a complex connectivity matrix as a function of angular frequency ω as $\mathbf{C}^*(\omega) = c_{m,l} \exp -j\omega\tau_{m,l}^\nu$. Therefore, a structural connectivity matrix whose nodes are normalized by $\deg_m = \sum_l c_{ml}$ at frequency ω can be expressed as:

$$\mathbf{C}(\omega) = \text{diag}\left(\frac{1}{\deg}\right) \mathbf{C}^*(\omega) \quad (4.3)$$

Replacing the connectivity term in (4.2) with (4.3) and adjusting all vector notations into matrix notation, we derive the following equations for network level activity in the frequency domain:

$$j\omega \mathbf{X}(\omega) = -\beta(\mathbf{X}(\omega) - \alpha \mathbf{X}(\omega) \mathbf{C}(\omega)) + \mathbf{P}(\omega) \quad (4.4)$$

$$\mathbf{X}(\omega)(j\omega \mathbf{I} + \beta(\mathbf{I} - \alpha \mathbf{C}(\omega))) = \mathbf{P}(\omega) \quad (4.5)$$

4.2.2 Complex Laplacian Matrix

Our goal is to examine the characteristic patterns of diffusion revealed by the structural network's normalized Laplacian matrix. Here, we make use of (4.3) to introduce a complex Laplacian matrix that absorbs the network properties of both the structural connectivity matrix as well as the distance adjacency matrix. By substituting the complex Laplacian matrix and rebalancing (4.5), we obtain a closed-form solution for $\tilde{\mathbf{X}}(\omega)$:

$$\mathbf{X}(\omega) = (j\omega I + \beta \mathcal{L}(\alpha, k))^{-1} \mathbf{P}(\omega) \quad (4.6)$$

In this closed-form solution, we defined a complex Laplacian matrix \mathcal{L} as a function of global coupling strength α and wave number k , which facilitates the dynamics and frequency profiles observed on the brain's connectome. Since frequency ω and transmission speed v always occur as a ratio, we define the wave number $k = \frac{\omega}{v}$. The wave number represents the spatial frequency of any propagating wave, describing the amount of oscillations per unit distance traveled [236]. Then the complex Laplacian matrix \mathcal{L} has the form:

$$\mathcal{L}(\alpha, k) = \mathbf{I} - \alpha \mathbf{C}^*(k) \quad (4.7)$$

Where \mathbf{I} is the identity matrix and $\mathbf{C}^*(k)$ is the complex connectivity matrix as defined above. While (4.3) indicates that the propagating signals in the network is governed by \mathcal{L} , the complex Laplacian of the network describes the characteristic patterns of signal spread in a network, and we can obtain these spatial patterns via the decomposition:

$$\mathcal{L}(\alpha, k) = \sum_{n=1}^N \mathbf{u}_n(\alpha, k) \lambda_n(\alpha, k) \mathbf{u}_n^H(\alpha, k) \quad (4.8)$$

Where $\lambda_n(\alpha, k)$ are the eigenvalues of the complex Laplacian matrix and $\mathbf{u}_n(\alpha, k)$'s are the complex eigenmodes of the complex Laplacian matrix. Here, the entries of the complex Laplace eigenmodes represent the relative amount of activation in each parcellated brain region as controlled by global coupling and wave number parameters.

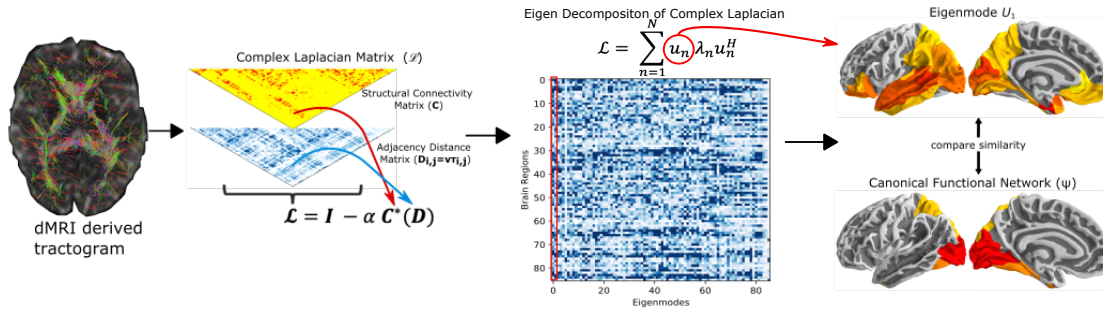


Figure 4.1: The analysis overview.

Structural connectivity matrix (C) and distance adjacency matrix (D) were extracted from diffusion MRI derived tractograms, to construct the complex Laplacian of the brain's structural network. An eigen decomposition on the network's complex Laplacian (\mathcal{L}) was performed obtain complex structural eigenmodes of the brain (U). The spatial similarities were computed between the structural eigenmodes and canonical functional networks in fMRI. Here, as an example, we show brain rendering of the leading eigenmode from the HCP template structural connectome (right column, top) and the canonical visual functional network (right column, bottom).

4.3 Methods

4.3.1 Structural Connectivity Network Computation

We constructed structural connectivity networks according to the Desikan-Killiany atlas where the brain images were parcellated into 68 cortical regions and 18 subcortical regions as available in the FreeSurfer software [237, 182]. We first obtained openly available diffusion MRI data from the MGH-USC Human Connectome Project to create an average template connectome [183]. Additionally, we obtained individual structural connectivity networks from 36 subjects' diffusion MRI data. Specifically, *Bedpostx* was used to determine the orientation of brain fibers in conjunction with *FLIRT*, as implemented in the *FSL* software [116]. Tractography was performed using *probtrackx2* to determine the elements of the adjacency matrix. We initiated 4000 streamlines from each seed voxel corresponding to a cortical or subcortical gray matter structure and tracked how many of these streamlines reached a target gray matter structure. The weighted connection between the two structures $c_{l,m}$ was defined as the number of streamlines initiated by voxels in region l that reach any voxel within region m , normalized by the sum of the source and target region volumes. This normalization prevents large brain regions from having extremely high connectivity due to having initiated or received many streamline seeds. Afterwards, connection strengths are averaged between both directions ($c_{l,m}$ and $c_{m,l}$) to form undirected edges. Additionally, to determine the geographic location of an edge, the top 95% of non-zero voxels by streamline count were computed for both edge directions, the consensus edge was defined as the union between both post-threshold sets.

4.3.2 Canonical Functional Networks

We chose the 7 CFN parcellations mapped by Yeo et al. [53] as the functional spatial patterns most frequently visited by the human brain. The brain parcellations were created from fMRI recordings of 1000 young, healthy English speaking adults at rest with eyes open. A clustering algorithm was used to parcellate and identify consistently coupled voxels within the brain volume. The results revealed a coarse parcellation of seven networks: $\Psi_{CFN} = \{\text{limbic, default, visual, frontoparietal, somatomotor, ventral attention, dorsal attention}\}$.

The CFN parcellation was co-registered to brain regions of interest in the gyral based Desikan-Killany atlas [182] to match the dimensionality of our complex Laplacian structural eigenmodes. Then spatial activation maps of each canonical network was produced by normalizing the number of voxels per brain region belonging to a specific CFN by the total number of voxels in the brain region of interest (Fig 1). Both the functional networks and the Desikan-Killany atlas are openly available for download from Freesurfer [114] (<http://surfer.nmr.mgh.harvard.edu>).

4.3.3 Global Parameter Optimization for Individual Structural Eigenmodes

To ensure that we obtained a globally optimal set of parameters α, k that provided a complex Laplacian eigenmode \mathbf{u}_n which is the most similar to the spatial pattern of each of the seven Ψ_{CFN} , we performed an optimization of the cost function: $f(\alpha, k, n) = 1 - \text{corr}(\Psi_{CFN}, \mathbf{u}_n(\alpha, k))$ to determine the optimal eigenmode,

coupling, and wavenumber for each canonical functional network. We used the “basin-hopping” global optimization technique on this cost function, a robust technique for non-convex cost functions [207]. This algorithm is able to escape from local minima in the parameter space by accepting and “hopping” to new parameters even if they increase the cost function. The algorithm will accept iterations that decrease the cost function evaluation with a probability of 1, but only accept iterations that do not decrease cost function with a probability of $\exp(\Delta(f)/T)$, where $\Delta(f)$ is the change in the cost function across successive iterations, and T is a constantly decreasing “temperature” term. Larger T indicates that the algorithm is more willing to accept jumps in cost function evaluation. We initiated the optimization procedure from ten different initial parameter values and selected the best result out of all initialization runs.

4.3.4 Similarity Analysis Between Canonical Functional Networks and Cumulative Linear Combination of Structural Eigenmodes

Here, we examine whether structural eigenmodes can form a linear basis for activation patterns for canonical functional networks and examine if a cumulative combination of structural eigenmodes improves the spatial similarity with CFN’s when compared to individual structural eigenmodes. For each CFN, we first ordered the eigenmodes based on their individual similarity after global parameter optimization using procedures described in the previous section. For each CFN, we then computed similarity of the optimal linear weighting of sorted individual structural eigenmodes \mathbf{u}_l with Ψ_{CFN} by cumulatively adding struc-

tural eigenmodes ordered by their similarity. We minimized the L_2 – norm of $\|\Psi_{CFN} - \sum_{l=1}^N \mathbf{u}_l(\alpha, k)w_l\|$, to obtain the optimal weights w_l and a quantification of spatial patterns obtained by the best cumulative set of eigenmodes.

Spatial similarity of cumulative eigenmodes with CFNs were then computed using both Pearson’s (Figure 4.6) and Spearman’s correlations (Figure S2). While Spearman’s correlation was appropriate for non-continuous correlative comparisons, its non-linearity due to sorting of values was evident in volatile changes of spatial similarity, and Pearson’s correlation provided more stable results.

We repeated the above analysis for both the conventional real-valued Laplacian without frequency and transmission speed tuning, as well as complex Laplacians obtained from randomized connectivity matrices. For random connectivity matrices, we constructed 1000 realizations of random connectivity and distance matrices to allow us to compare and quantify the performance of the brain’s structural eigenmodes against eigenmodes of randomized graphs. The random matrices were constructed with the same sparsity as the HCP template connectome, and the elements of the random matrices were assigned by randomly sampling from a distribution that’s representative of the mean and variance of the HCP template connectome and distance matrices.

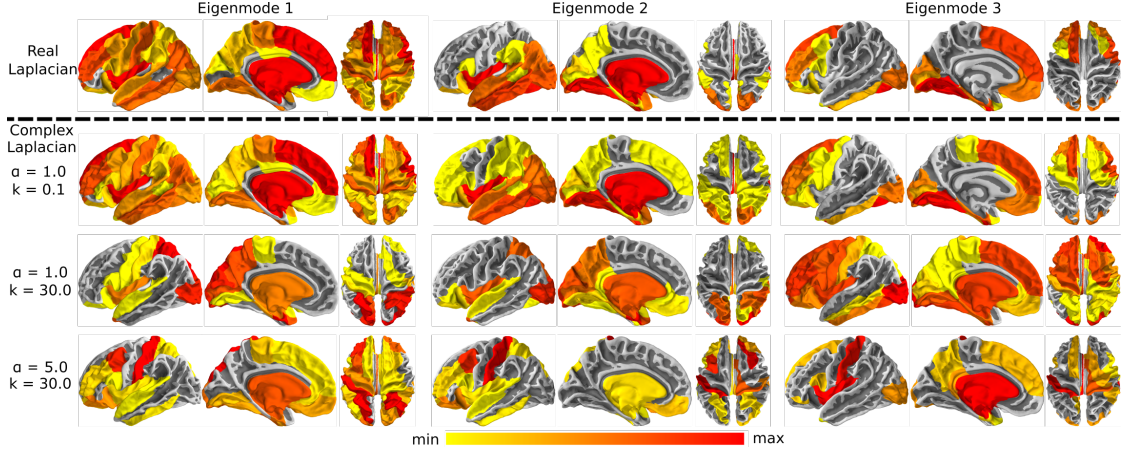


Figure 4.2: Complex Laplacian eigenmode for different parameter choices.

Three representative eigenmodes decomposed from the complex Laplacian with different tuning parameters and three representative eigenmodes decomposed from the real-valued Laplacian without transmission speed and distance delay properties are shown. The top row shows brain renderings of the real Laplacian eigenmodes with coupling strength $\alpha = 1$. Complex Laplacian eigenmodes with high transmission speed approaches extremely small wave number or delays in the network ($\alpha = 1, k = 0.1$), closely resembles the real Laplacian eigenmodes (second row). Complex Laplacian eigenmodes with higher wave numbers with parameters ($\alpha = 1, k = 30$) and ($\alpha = 5, k = 30$) are respectively shown in the third and fourth rows, demonstrating that parameter choice control the spatial distribution of structural eigenmodes.

4.4 Results

4.4.1 Structural connectivity based functional activation patterns

We use the HCP template connectome to demonstrate the wide range of spatial activity patterns achievable by the eigenmodes of the complex Laplacian matrix. The top row of Figure 4.2 shows three exemplary real-valued structural eigenmodes ($\alpha = 1$) without frequency and transmission speed tuning. Consistent with previous works, we see the Laplace eigenmodes of the human structural connectome display a wide range of cortical activity patterns [232, 229].

As a comparison, we show in the next row complex Laplace eigenmodes with low wave number ($k = 0.1$), representing a network with extremely high transmission speed or near zero delay. In such a low delay network, the complex Laplace eigenmode closely resembles the spatial patterns seen in real-valued Laplace eigenmodes where delays are not a factor in the network. We also show two additional examples of complex Laplace eigenmodes with higher wave number values, emphasizing the impact of transmission speed and delays in the structural network of the brain. The combination of coupling strength and wave number global parameters enables a richer diversity of spatial cortical patterns, with left and right hemisphere specific activations around the dorsal-caudal brain regions. Despite the increase in model complexity, our approach allows a feature-rich graph theoretic approach to directly infer resting state functional brain patterns from the structural graph of the brain.

4.4.2 Eigenmodes of the complex Laplacian resemble CFN activation patterns

We re-assigned the voxel-wise parcellations of the seven CFNs from Yeo et al. [53] to brain regions from the Desikan-Killiany atlas (Figure 4.3A, left column), this re-sampling of the parcellations allow spatial pattern comparisons of equal dimensions against our structural connectomes and Laplace eigenmodes. The middle column of Figure 4.3A shows best matching complex Laplace eigenmodes after optimization of the global parameters with the HCP template connectome to each CFN. In addition to displaying the best-performing eigenmode in each case, we further ranked the eigenmodes according to their spatial correlation

values and displayed the best weighted linear combination of the top 10 complex Laplace eigenmodes on the right column of Figure 4.3A, the corresponding scatter plots showing linear regression fits with 95% confidence intervals are shown in Figure 4.3B. Spatial similarity metrics such as Dice score and Jaccard index were also explored, but such metrics require comparison between binary partitions on images, and are extremely sensitive to the thresholding scheme used for binarizing data. Nonetheless, we found model parameters optimized by the Dice coefficient display similar results as spatial correlation metrics (Figure A.3). The spatial correlation values of the best performing eigenmode, and details of cumulative combinations of eigenmodes are reported below and in Figure 6. We observe that CFN patterns emerge when parameters, optimized for each network, are applied to the complex Laplacian. Only a few structural eigenmodes are required to capture a specific functional network.

4.4.3 Parameter tuning of complex Laplacian eigenmodes

To examine the sensitivity of our eigenmodes to our complex Laplacian parameters, we first computed spatial correlation values for all eigenmodes for each CFN across the entire parameter range. Figure 4.4 (top) shows the effect of fixing k and varying α , while bottom row shows the effect of varying k at a fixed α . At a glance, almost all eigenmodes are capable of resembling any given CFN with the proper choice of tuning parameters, and it is evident that we need to tune both the global coupling strength and wave number for a dominant eigenmode matching a specific CFN to emerge. For any given CFN, we find parameter regimes that recruit multiple eigenmodes while others recruit a single one. This is especially true of the wave number parameter and not

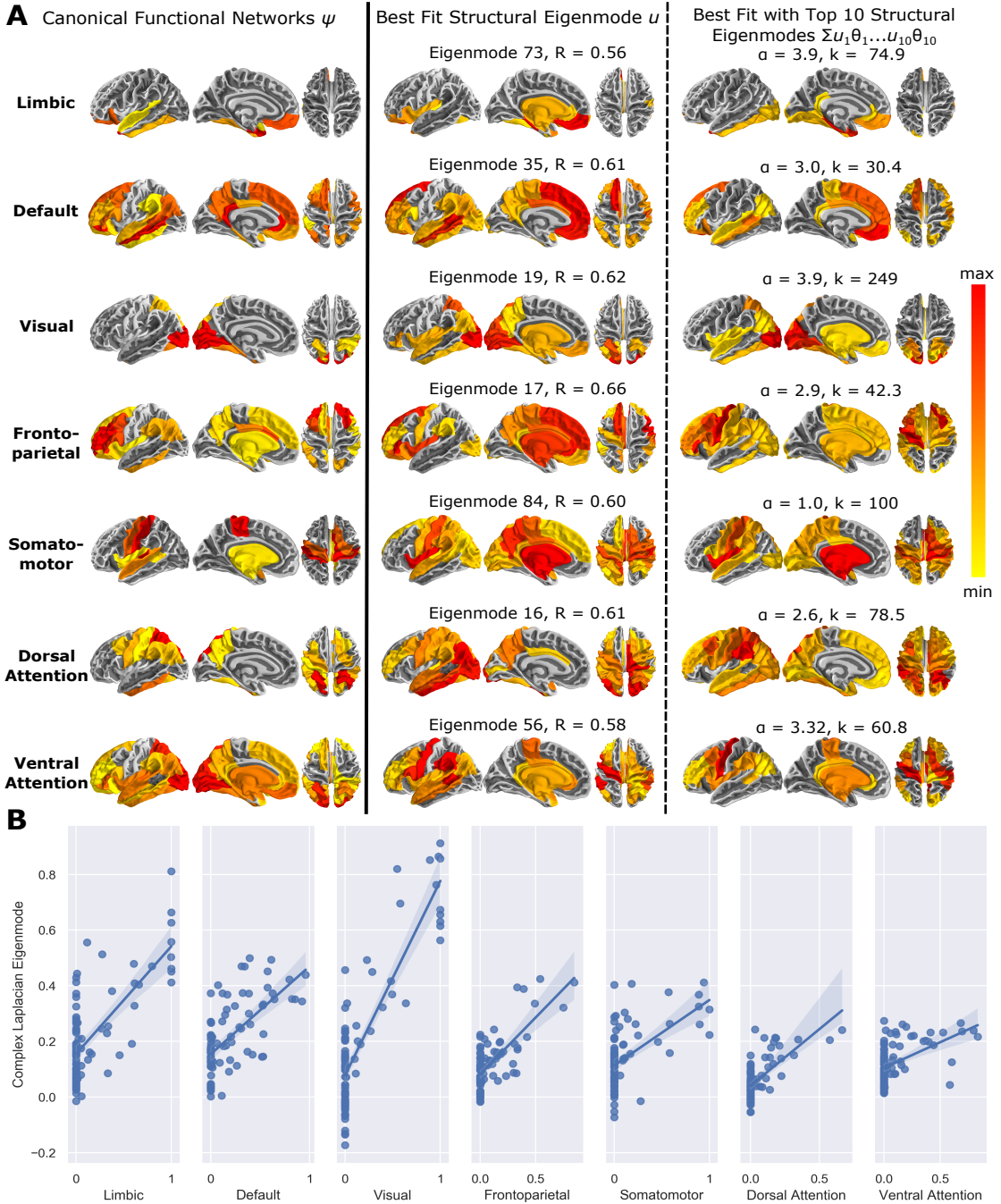


Figure 4.3: Canonical functional networks reproduced by structural eigenmodes.

(A) Brain renderings of the seven canonical functional networks are shown in the left column. Individual structural eigenmodes with the highest spatial correlation to each functional network, after parameter optimization, are shown in the middle column. After ranking all structural eigenmodes by highest spatial correlation, a linear combination of the top ten best performing eigenmodes are shown in the right column. Parameter values producing the best spatial matches to each canonical functional network are listed in the right column and applies to all eigenmodes. (B) Top 10 best fitted structural eigenmodes and canonical functional network comparisons shown in scatter plots with linear regression line and 95% confidence interval.

so for coupling strength. Furthermore, the best achievable spatial correlation stay consistent as we tweak the global coupling strength, whereas wave number tuning causes shifts in spatial similarity value and eigenmode occupation. And finally, the limbic network has the lowest spatial match and the least a mount of shift in spatial correlation values.

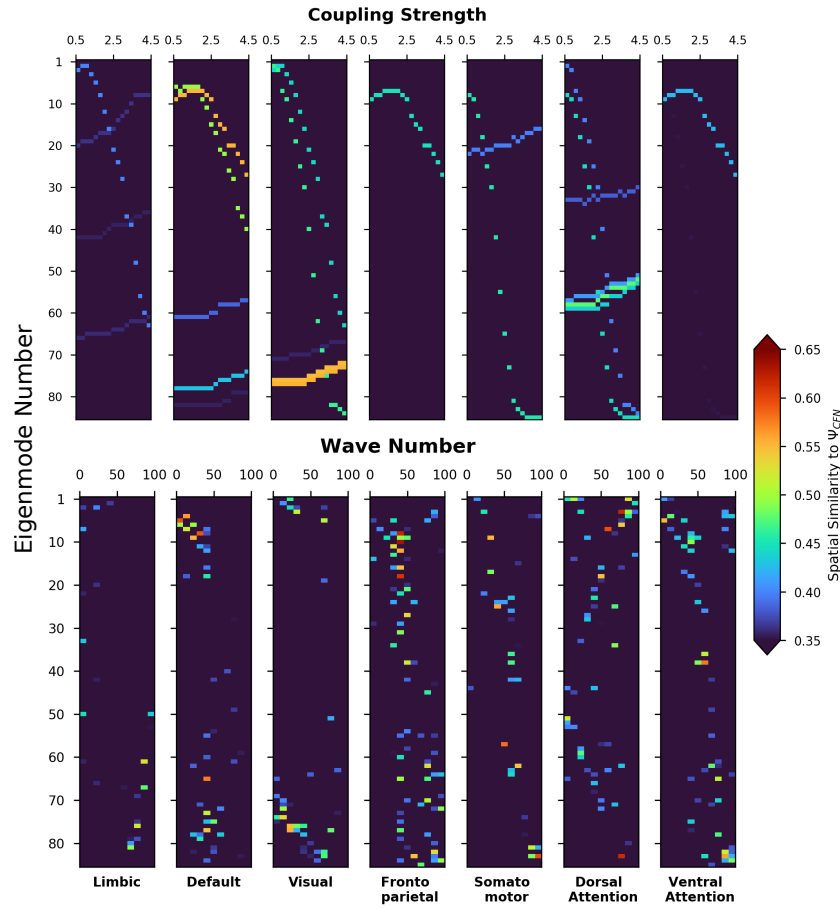


Figure 4.4: Structural eigenmode spatial similarity to canonical functional networks depends on model parameters.

Colors display the spatial correlation values (Spearman's) of all complex Laplacian eigenmodes across all parameter values with each canonical functional network. Shifts in coupling strength (α , top, with wave number held constant at $k = 10$) does not cause a change in peak spatial correlation, but only in the ordering of the eigenmodes. In contrast, however, shifts in wave number (k , bottom), with coupling strength held constant at $\alpha = 1$, leads to changes in eigenmode spatial patterns and spatial correlation to canonical functional networks.

To further examine the tunable parameter's effects on the leading (best per-

forming) eigenmodes, we show a heat map of the spatial correlation achieved by the dominant eigenmode as we shifted parameter values in Figure A.1. As expected, global coupling parameter had no effect on dominant eigenmode's fit while the wave number did. Subsequently, we split the wave number parameter into its two components: transmission velocity and oscillating frequency of signals in the network, showing that those two components equally affect spatial patterns emerging from the complex Laplacian eigenmodes (Figure A.1 bottom row). The spatial correlation patterns of each functional network also implies that there are potentially functional network specific eigenmodes obtainable from the structural complex Laplacian, which will be explored further in the subsequent group level analysis.

On the group level, we found parameter sets that provided the most spatially similar complex Laplace eigenmode for each canonical functional network. The rank of the most spatially similar eigenmodes are summarized in violin plots in Figure 4.5. With the exception of the default mode network, whose best structural match spans across the range of all eigenmodes, all other canonical functional networks exhibit selectivity towards a specific subset of ranked eigenmodes. The limbic and visual networks, which contains dense connections in the anterior and ventral regions of the brain, prefer to occupy eigenmodes at both low and high ends of the eigen spectrum. On the other hand, the dorsal and ventral attention networks mainly occupy the middle of the eigen-spectrum. The specific occupancy patterns shown here implies there may be a hierarchy to the functional and structural organization of the brain, and the functioning brain minimizes the recruitment of unrelated structural connections when engaged in conscious brain activity.

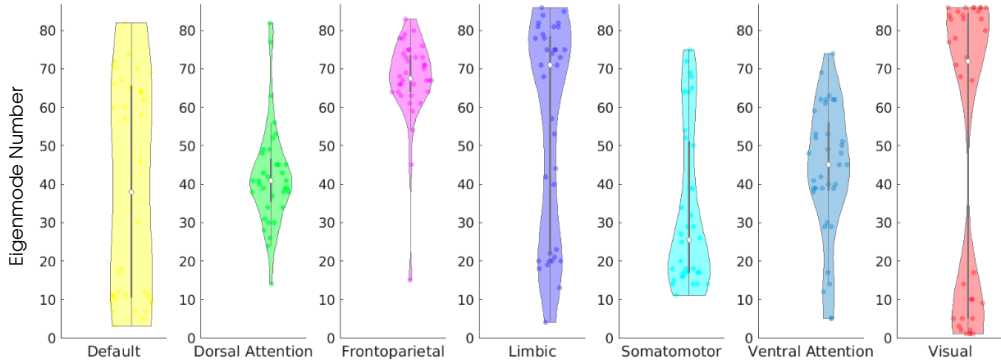


Figure 4.5: Canonical functional networks have complex Laplacian eigenmode specificity.

Each dot on the violin plot corresponds to the best performing eigenmode number. Showing that across all subjects ($n = 36$), canonical functional networks occupies specific structural eigenmodes as the dominant structural basis. Default mode network is the exception as the best performing eigenmode spans across all eigenmodes. On the other hand, the rest of the canonical functional networks cluster to specific eigenmode numbers.

4.4.4 Complex Laplacian eigenmodes outperform real Laplacian eigenmodes

We created 1000 random realizations of connectivity matrices and their corresponding distance adjacency matrices that share the same sparsity, mean, and standard deviation values as the HCP template connectome values. Comparisons between eigenmodes of the HCP template connectome and randomly generated connectomes are displayed in Figure 4.6. The Laplace eigenmodes of the brain's white matter network can be seen as individual subsets of cortical activation patterns that make up the brain's functional activity. Therefore, spatial match between cumulative combinations of eigenmodes to each canonical functional network were computed in addition to just the leading eigenmode.

Overall, the HCP complex Laplacian's best-performing eigenmodes achieved higher spatial correlation and lower residuals than other variants of Laplace

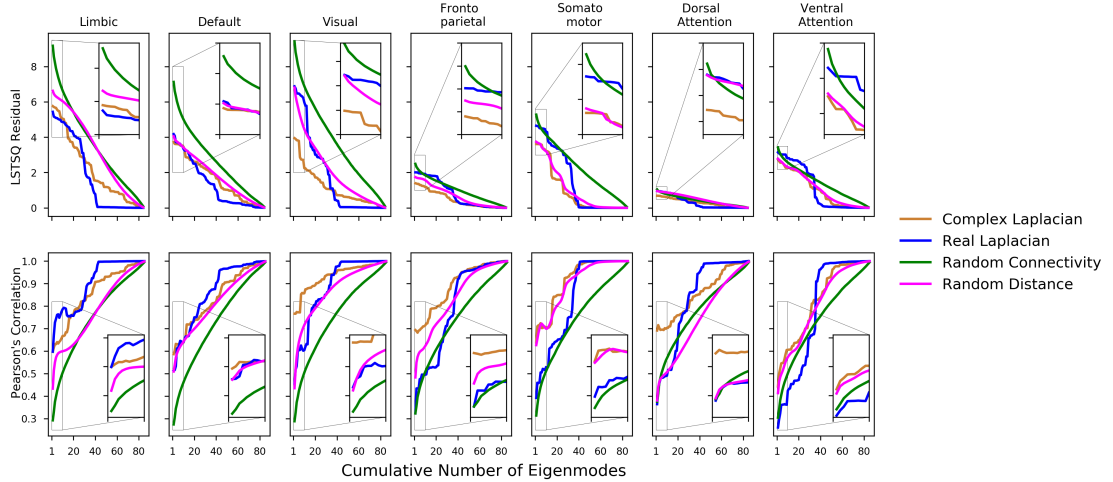


Figure 4.6: Structural eigenmodes of the HCP template complex Laplacian predict canonical functional networks better than structural eigenmodes of the real Laplacian.

For each canonical functional network, we quantified its spatial similarity against linear combinations of structural eigenmodes obtained from various types of Laplacians. The spatial similarities quantified by linear least squares residuals are shown on top, and Pearson’s correlations are shown on the bottom. Overall, accumulation of structural eigenmodes improves the spatial similarity between functional networks and structural eigenmodes. The complex HCP eigenmodes (orange) and real-valued HCP eigenmodes (blue) both outperform eigenmodes decomposed from random connectomes and random distance matrices (green). However, only the complex HCP eigenmodes outperform complex eigenmodes decomposed from the HCP template connectome paired with random distance matrices (magenta).

eigenmodes in 6 out of the 7 CFNs (left-most point on each curve). As more individual eigenmodes are linearly combined, all variants show a steady improvement in spatial similarity, with the fully random variant using the most number of eigenmodes to achieve a high spatial match, suggesting the fully random eigenmodes are the least informative. On the other hand, the complex eigenmodes from randomized distance Laplacians (magenta) consistently performs better than fully random complex eigenmodes (green) but lacks the structural distance information to compete with complex Laplace eigenmodes constructed with HCP template connectivity and distance adjacency matrix. The spatial similarity reported in Figure 4.6 is Pearson’s correlation due to its smooth-

ness, we show the same quantification with Spearman’s correlation in Figure A.2, which is more appropriate for discrete samples, but its more volatile due to its nonlinear ordering of samples.

Spatial similarities from random variants of complex Laplace eigenmodes were normalized into a Z-score distribution for construction of 95% confidence intervals and comparisons against HCP connectome variants. Comparing only the leading eigenmodes without cumulative combinations, Complex Laplacian eigenmodes significantly outperforms random connectivity eigenmodes for all functional network comparisons ($P < 0.05$), but only significantly outperforms the randomized distance eigenmodes for the limbic, visual, frontoparietal, and dorsal attention networks. On the other hand, the real-valued Laplace eigenmodes does not significantly outperform eigenmodes from fully random connectivity profiles for all functional networks. The P -values for both Pearson’s and Spearman’s metrics are shown in Supplementary Tables A.1 and A.2.

4.4.5 Group level eigenmode analysis

Figure 4.7 shows a violin plot of the best spatial correlation achieved by each subject’s complex Laplacian in orange, real Laplacian in blue, and random distance adjacency matrix paired with the HCP connectome in magenta. Consistent with our HCP template connectome analysis, the complex Laplacian eigenmodes outperforms both the real Laplacian eigenmodes and randomized distance complex Laplacian eigenmodes. Our complex Laplacian framework includes the additional distance and delay information in the brain networks compared to conventional real Laplacian eigenmodes, therefore we generated complex Lapla-

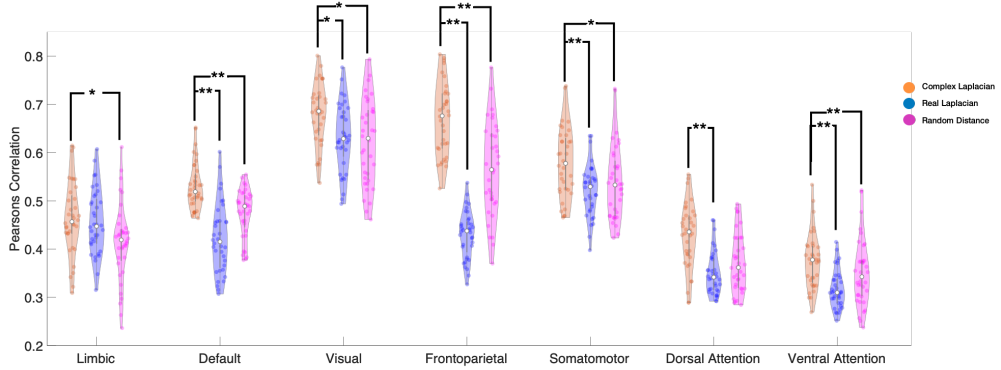


Figure 4.7: Complex Laplacian outperforms real Laplacian in recapitulating canonical functional networks with individual structural connectomes.

Violin plot showing that on a group level (each dot correspond to one subject, $n = 36$), the best performing structural eigenmodes of the complex Laplacian (orange) outperforms the corresponding structural eigenmode from the real Laplacian (blue) and random distance complex Laplacian (magenta). Paired T-test results of complex Laplacian against either real Laplacian or random distance complex Laplacian shows the complex Laplacians eigenmodes achieving significantly higher spatial similarity on the group level (P-values shown as * < 0.5 , ** < 0.01).

cien eigenmodes from HCP structural connectivity paired with random distance adjacency matrices, which as a comparative degree of freedom. Paired T-tests were performed for all CFNs, the complex Laplacian eigenmodes outperformed real Laplacian eigenmodes at the group level for all networks except the limbic network ($p = 0.64$). On the other hand, significantly higher spatial similarity was achieved by complex Laplacian eigenmodes for all networks except the dorsal attention network ($p = 0.12$) when comparing against the random distance group results.

4.5 Discussion

In this study we have proposed a complex graph Laplacian framework that demonstrates an ability to capture functional connectivity patterns, while main-

taining parsimony and low-dimensionality of spectral graph models. The model involves only two global and biophysically meaningful parameters, one controlling the speed of activity propagation, and the other controlling coupling strength between remote populations of neurons connected via axonal projections. The complex Laplacian eigenmodes that emerge from our model are intrinsic properties of the brain’s anatomy, which can potentially become a powerful tool in the study of brain networks. However, it is not at all clear if the well-characterized properties of a real valued Laplacian matrix [238] in the literature can easily translate to its complex counterpart. Questions about the theory and salient properties of the complex Laplacian are important and novel, however, existing literature in this area is limited to exploratory stages, such as the recently published pre-print article on Laplacians and their properties in complex value weighted graphs [239]. In the current manuscript, we showcased application of the complex Laplacian in brain modeling. We presented detailed statistical analysis of the resulting complex-value Laplacian eigenmodes, focusing on their ability to predict the spatial patterns observed on seven CFNs that are well established in functional neuroimaging. The implications of our main contributions are discussed below, with additional context and relevance to current literature.

4.5.1 A simple yet feature-rich graph theoretic approach

We derived a simple model of network diffusion of activity which takes into account the path delays introduced by realistic axonal conductance speeds and fiber lengths, and showed that at the first order the behavior of the model can be captured within a complex Laplacian, on which a complex-valued graph diffusion process is enacted. Using this definition of the complex Laplacian we

demonstrated that its eigenmodes constitute a sparse basis that is capable of reproducing the characteristic spatial patterns of empirical resting state functional activity given by the 7 CFNs.

4.5.2 Higher predictive power than existing graph models

We showed that the complex Laplacian outperforms the existing models that use the eigenmodes of real-valued Laplacian. These results are far better than can be expected by chance, as indicated by the significance values of our results with respect to large simulations with Laplacians calculated from random connectomes. Thus, future graph models can benefit from the enhanced predictive power of the proposed complex Laplacian approach, which in the cases we have tested highly significantly improves performance(see Figure 4.5). Our work can therefore find direct applicability in many clinical and neuroscientific contexts where predicting functional patterns from structure is important [240, 241], particularly in cases of epilepsy [242], stroke [243, 244], and neurodegeneration [168].

4.5.3 Complex eigenmodes accommodate a diversity of spatial patterns

One of the most intriguing aspects of our study is the demonstration that almost all (complex) eigenmodes are capable of resembling any given CFN, with the proper choice of tuning parameters. As observed from Figure 4.4, certain parameter regimes recruit multiple eigenmodes while others recruit a

single one; however with the right selection of the two model parameters, it is possible to "steer" the eigenmodes in such a manner that a small number of them can reproduce any CFN. This not only denotes the strength of our approach, we believe it points to an essential characteristic of real brain activity, which is thought to accommodate a large repertoire of microstates and their concomitant spatial patterns. This rich repertoire was shown above to be capable of being engaged by our parsimonious graph model, which may point to the possibility that complex behavior may be achievable by simple and parsimonious mechanisms, and may not require the kinds of high-dimensional and non-linear oscillatory models that have held sway in the field of neural modeling [175, 226]. Our work also supports the idea that macroscopic neurophysiological data on a graph can be sufficiently modeled with linear metrics, and nonlinear methods may not be required for problem of such scale [245, 246].

4.5.4 Rich repertoire is tunable with two biophysical parameters

In our model, the brain can access any configuration of spatial patterns seen in real resting state functional networks by tuning only two of its global and biophysically meaningful parameters: coupling strength and wave number. Our current work indicates that physical distances and the transmission rate of oscillatory activity in combination with coupling strength is sufficient in generating various canonical functional brain patterns. This demonstration in an analytical model, that a rich repertoire of states is accessible to the brain by tuning biophysical processes, has not previously been reported to our knowledge. The present computational study is not intended to explore the neural mechanisms that might control these parameters. Nevertheless, modern neuroscience provides

several potential mechanisms.

Coupling strength α is a direct scaling of white-matter excitatory long range connections between neural populations in the brain. Phase and amplitude coupling of oscillatory processes in the brain is evidently important for the formation of coherent wide-band frequency profiles of brain recordings and processing of information [247, 248, 249, 250, 15]. Parameterization of coupling strength between distant brain regions via the connectome is ubiquitous in connectivity based models of BOLD fMRI [14, 15, 175, 228] and electroencephalography activity [251, 227, 252]. Furthermore, pathological FC patterns as a result of disconnections in the brain can be reproduced with decrease in coupling strength [253, 254].

The other key tunable parameter in our model, wave number k , is the ratio between the oscillatory frequency and transmission velocity of a propagating signal, describing the amount of oscillations per unit distance traveled by any signal spreading throughout the brain's structural network. While transmission speed of signals between brain regions is often overlooked in brain modeling efforts, its importance is emphasized by the biology of the central nervous system. Neuronal spike arrival timing at the cellular level and coherent oscillatory activity at the network level are carefully managed by synaptic strengths as well as axonal myelination, respectively [255, 256]. Further, wave number can be controlled not just by conductance speed, but also by the operative frequency of oscillations ω . From the deep literature on wide-band frequency response of brain recordings, it is already known that different functional networks of resting state BOLD data are preferentially encapsulated by different higher-frequency bands via phase- and amplitude-coupling [250, 15]. Hence it is plausible that wave number tuning

may be achieved biologically via either dynamic conductance speed or dynamic control of frequency bands.

4.5.5 Relationship to existing studies

Recent graph models involving eigen spectra of the adjacency or Laplacian matrices of the structural connectome have greatly contributed to our understanding of how the brain’s structural wiring gives rise to its functional patterns of activity. Although these models have very attractive features of parsimony and low-dimensionality, they suffer from being feature poor and an inability to make stronger predictions about functional networks.

Such models mapping between structural and functional patterns of the human brain have typically assumed that SC and FC are not independent entities, and that relationship between the two cannot simply be explained by a direct mapping [175]. In addition to connection strength between regions, metrics such as anatomical distances [257], shortest path lengths [258], diffusion properties [232, 243], and structural graph degree [259] were also found to contribute to the brain’s observed functional patterns. Higher-order walks on graphs have also been quite successful; typically these methods involve a series expansion of the graph adjacency or Laplacian matrices [260, 200]. The diffusion and series expansion methods are themselves closely related [234], and almost all harmonic-based approaches may be interpreted as special cases of each other, as demonstrated elegantly in recent studies [261, 262]. The wealth of studies elucidating how the observed function originate from the underlying structural network provided a strong motivation for our approach, which extracts functional patterns from

the informative complex graph Laplacian that incorporates both the connection strengths as well as the anatomical distances of the structural network.

In contrast to spectral graph models, inferring functional connectivity from biophysiological models of neuronal populations have been a specialty of dynamic causal models (DCMs). Such generative models have emerged as powerful tools mainly to infer effective (directional) connectivity for smaller networks [50, 209, 263, 264, 265], or dynamic functional connectivity [266, 267]. While the goal of DCMs is similar to our proposed model that makes model inferences about FC, the two frameworks are different in terms of approach and dimensionality. DCMs examine the second order covariances of brain activity, and it is only recent works with spectral and regression DCM models have expanded the model coverage to the whole-brain scale and the potential to incorporate SC data [268, 269, 270]. However, these models rely on formulation of local neural masses to derive dynamical behavior, which are then used to generate effective or dynamic connectivity through simulations. By avoiding large-scale simulations of neuronal activity, in our proposed framework we not only allowed canonical functional patterns to emerge directly from a complex Laplacian matrix, we have also created a model with only two global parameters. Most DCM models have many more degrees of freedom compared to our work because of their parameterization for different interactions within and between brain regions. In contrast to some of more recent spectral DCM parameterizations, additionally, our global parameters reflecting the brain's anatomical connection density and distances traveled between connections continue to have clear biophysical interpretability.

Frequency-band specific magnetoencephalography (MEG) resting-state networks have been successfully modeled with a combination of delayed NMMs

and eigenmodes of the structural network [230], suggesting delayed interactions in a brain's network give rise to functional patterns constrained by structural eigenmodes. In our recent work, we expanded upon eigenmodes of SC matrices by integrating time delays in the brain with SC to create a complex Laplacian matrix in the Fourier domain [231]. Using the eigen-spectra of the complex Laplacian matrix, we found specific subsets of complex eigenmodes that contributed to specific cortical alpha and beta wave patterns. The findings in the current article expands upon these time-delayed eigenmodes to find subsets of eigenmodes predictive of canonical functional networks derived from resting state fMRI. Our theorized framework provides two global parameters that act on the structural connectome and its corresponding distance adjacency matrix to control coupling strength and delays in the network. These findings supports other works suggesting there is a possible organizational hierarchy, or gradients of topographical organization that spatially constraints cortical function [271, 272, 273, 274, 275]. Margulies et al. proposed that so-called "principal gradients", which may be interpreted as the Laplacian eigenmodes of the FC matrix, serve as the core organizing axis of cerebral cortex, spanning from unimodal sensorimotor to integrative transmodal areas [271]. The complex eigenmodes proposed here may therefore be considered as the structural analog of Margulies' principal gradients.

Similarly, we found that the unimodal sensorimotor networks at one end of the principal gradient, which accounts for the most variance in connectivity, achieved the highest spatial correlations. On the other hand, transmodal networks on the opposite end of the axis, needed much more cumulatively combined structural eigenmodes to achieve high spatial similarity.

Atasoy et al. previously modeled the same resting-state canonical functional networks used here with real-valued Laplacian eigenmodes as structural substrates on which a mean field neural model dictated cortical dynamics [229]. While the model dimensionalities between the two studies are vastly different, we show that in the absence of a neural dynamical system, the addition of time lag in the network allowed canonical functional networks to emerge from just structural substrates. Furthermore, we believe incorporating time lags in our structural connectivity of the brain to create complex Laplacian matrices is an informative but unexplored alternative to regular Laplacian normalizations of brain networks. Particularly, the complex connectivity matrix in Fourier domain allows exploration of oscillatory frequency and phase shifts between brain regions as a property of the network, potentially presenting an opportunity in utilizing complex structural eigenmodes to integrate SC for explaining imaginary coherence patterns in MEG and EEG.

4.5.6 Limitations

The current results are limited by data resolution. Tractograms obtained from diffusion weighted images are approximations of the brain's axonal white-matter connections. We recognize that tractography, paired with anatomical parcellation of brain regions, does fail to appreciate the finer structures in the brain, especially the more refined connections and nuclei in the brain stem as well as close neighbor connections. Despite the coarse parcellation and rough approximations of white matter architecture, our proposed approach utilizes a spatial embedding of the brain's connectomics information and is extendable to finer parcellations.

Our theorized model relies on an averaged approximation of fiber distances between ROIs, and we assumed a global parameter to account for conductance speed in the brain. In reality, the amount of myelination and synaptic strength varies greatly in the brain. However, our approximations were enough in recapitulating canonical functional networks in the human brain, while benefiting from a low dimensional and interpretable model. It is also worth noting that the canonical functional networks used in this work were obtained from data-driven clustering of fMRI activity, and is far from a comprehensive representation of the brain's functional patterns. While our work can be extended to finer functional parcellations, we sought to avoid overlap between canonical functional networks by using the 7 networks parcellation. For example, the dorsal and ventral attention networks are found to overlap with the salience network [276], and task activated fMRI patterns revealed regions that are positively and negatively associated with attention and default networks [277].

4.6 Conclusions

In conclusion, we show that the spatial embedding of the brain's connections in a structural connectome is a rich substrate, on which we can derive intrinsic functional patterns of the brain with a simple network diffusion approach. We show that Laplace eigenbasis in the complex frequency domain outperforms conventional eigenbasis of the graph Laplacian in capturing spatial patterns of canonical functional networks. We recognize the complex nonlinear activities and dense connections present in the brain, but our work suggests that we can continue to extend simpler linear modeling approaches to approximate what we observe with macroscopic imaging techniques such as BOLD fMRI and diffusion

weighted imaging.

CHAPTER 5

SPECTRAL GRAPH THEORY OF BRAIN OSCILLATIONS

5.1 Introduction

5.1.1 The Structure-Function Problem in Neuroscience

It is considered paradigmatic in neuroscience that the brain's structure at various spatial scales is critical for determining its function. In particular, the relationship between the brain's *structural wiring* and the *functional* patterns of neural activity is of fundamental interest in computational neuroscience. Brain structure and function at the scale of macroscopic networks, i.e. amongst identifiable grey matter (GM) regions and their long-range connections through white matter (WM) fiber bundles, can be adequately measured using current non-invasive measurement techniques. Fiber architecture can be measured from diffusion tensor imaging (DTI) followed by tractography algorithms [278, 279]. Similarly, brain function manifested in neural oscillations can be measured non-invasively using magnetoencephalography (MEG) and reconstructed across whole-brain networks. Does the brain's white matter wiring structure constrain functional activity patterns that arise on the macroscopic network or graph, whose nodes represent gray matter regions, and whose edges have weights given by the structural connectivity (SC) of white matter fibers between them? We address this critical open problem here, as the structural and functional networks estimated at various scales are not trivially predictable from each other [175].

Although numerical models of single neurons and local microscopic neuronal assemblies, ranging from simple integrate-and-fire neurons to detailed multi-compartment and multi-channel models [280, 281, 282, 283, 284] have been proposed, it is unclear if these models can explain structure-function coupling at meso- or macroscopic scales. At one extreme, the Blue Brain Project [285, 286] seeks to model in detail all 10^{11} neurons and all their connections in the brain. Indeed spiking models linked up via specified synaptic connectivity and spike timing dependent plasticity rules were found to produce regionally and spectrally organized self-sustaining dynamics, as well as wave-like propagation similar to real fMRI data [287]. However, it is unclear whether such efforts will succeed in providing interpretable models at whole-brain scale [288].

Therefore the traditional computational neuroscience paradigm at the microscopic scale does not easily extend to whole-brain macroscopic phenomena, as large neuronal ensembles exhibit emergent properties that can be unrelated to individual neuronal behavior [289, 290, 291, 292, 293, 228], and are instead largely governed by long-range connectivity [294, 295, 296, 297]. At this scale, graph theory involving network statistics can phenomenologically capture structure-function relationships [298, 213, 299], but do not explicitly embody any details about neural physiology [290, 291]. Strong correlations between functional and structural connections have also been observed at this scale [175, 228, 300, 301, 302, 250, 232, 303], and important graph properties are shared by both SC and functional connectivity (FC) networks, such as small worldness, power-law degree distribution, hierarchy, modularity, and highly connected hubs [213, 304].

A more detailed accounting of the structure-function relationship requires

that we move beyond statistical descriptions to mathematical ones, informed by computational models of neural activity. Numerical simulations are available of mean field [293, 224, 305] and neural mass [297, 252] approximations of the dynamics of neuronal assemblies. By coupling many such neural field or mass models (NMMs) using anatomic connectivity information, it is possible to generate via large-scale stochastic simulations a rough picture of how the network modulates local activity at the global scale to allow the emergence of coherent functional networks [297]. However, simulations are unable to give an analytical (i.e. closed form) encapsulation of brain dynamics and present an interpretational challenge in that behavior is only deducible indirectly from thousands of trial runs of time-consuming simulations. Consequently, the essential minimal rules of organization and dynamics of the brain remain unknown. Furthermore, due to their nonlinear and stochastic nature, model parameter inference is ill-posed, computationally demanding and manifest with inherent identifiability issues (cite identifiability paper here).

How then do stereotyped spatiotemporal patterns emerge from the structural substrate of the brain? How will disease processes perturb brain structure, thereby impacting its function? While stochastic simulations are powerful and useful tools, they provide limited neuroscientific insight, interpretability and predictive power, especially for the practical task of inferring macroscopic functional connectivity from long-range anatomic connectivity. Therefore, there is a need for more direct models of structural network-induced neural activity patterns – a task for which existing numerical modeling approaches, whether for single neurons, local assemblies, coupled neural masses or graph theory, are not ideally suited. Here we use a spectral graph model (SGM) to demonstrate that the spatial distribution of certain brain oscillations are emergent properties of the

spectral graph structure of the structural connectome. Therefore, we also explore how the chosen connectome alters the functional activity patterns they sustain.

5.1.2 A hierarchical, analytic, low-dimensional and linear spectral graph theoretic model of brain oscillations

We present a linear graph model capable of reproducing empirical macroscopic spatial and spectral properties of neural activity. We are interested specifically in the transfer function (defined as the frequency-domain input-output relationship) induced by the macroscopic structural connectome, rather than in the behavior of local neural masses. Therefore we seek an explicit formulation of the frequency spectra induced by the graph, using the eigen-decomposition of the structural graph Laplacian, borrowing heavily from **spectral graph theory** used in diverse contexts including clustering, classification, and machine learning [306, 307, 308, 309]. This theory conceptualizes brain oscillations as a linear superposition of eigenmodes. These eigen-relationships arise naturally from a biophysical abstraction of fine-scaled and complex brain activity into a simple linear model of how mutual dynamic influences or perturbations can spread within the underlying structural brain network, a notion that was advocated previously [228, 310, 258]. We had previously reported that the brain network Laplacian can be decomposed into its constituent “eigenmodes”, which play an important role in both healthy brain function [228, 232, 311, 229] and pathophysiology of disease [311, 312, 313, 314].

We show here that a graph-spectral decomposition is possible at all frequencies, ignoring non-linearities that are operating at the local (node) level. Like

previous NMMs, we lump neural populations at each brain region into neural masses, but unlike them we use a linearized (but frequency-rich) local model – see **Figure 1A**. The macroscopic connectome imposes a linear and deterministic modulation of these local signals, which can be captured by a *network transfer function*. The sequestration of local oscillatory dynamics from the macroscopic network in this way enables the characterization of whole brain dynamics deterministically in closed form in Fourier domain, via the eigen-basis expansion of the network Laplacian. As far as we know, this is the first closed-form analytical model of frequency-rich brain activity constrained by the structural connectome.

We applied this model to and validated its construct against measured source-reconstructed MEG recordings in healthy subjects under rest and eyes-closed. The model closely matches empirical spatial and spectral MEG patterns. In particular, the model displays prominent alpha and beta peaks, and, intriguingly, the eigenmodes corresponding to the alpha oscillations have the same posterior-dominant spatial distribution that is repeatedly seen in eyes-closed alpha power distributions. In contrast to existing less parsimonious models in the literature that invoke spatially-varying parameters or local rhythm generators, to our knowledge, this is the first account of how the spectral graph structure of the structural connectome can parsimoniously explain the spatial power distribution of alpha and beta frequencies over the entire brain measurable on MEG.

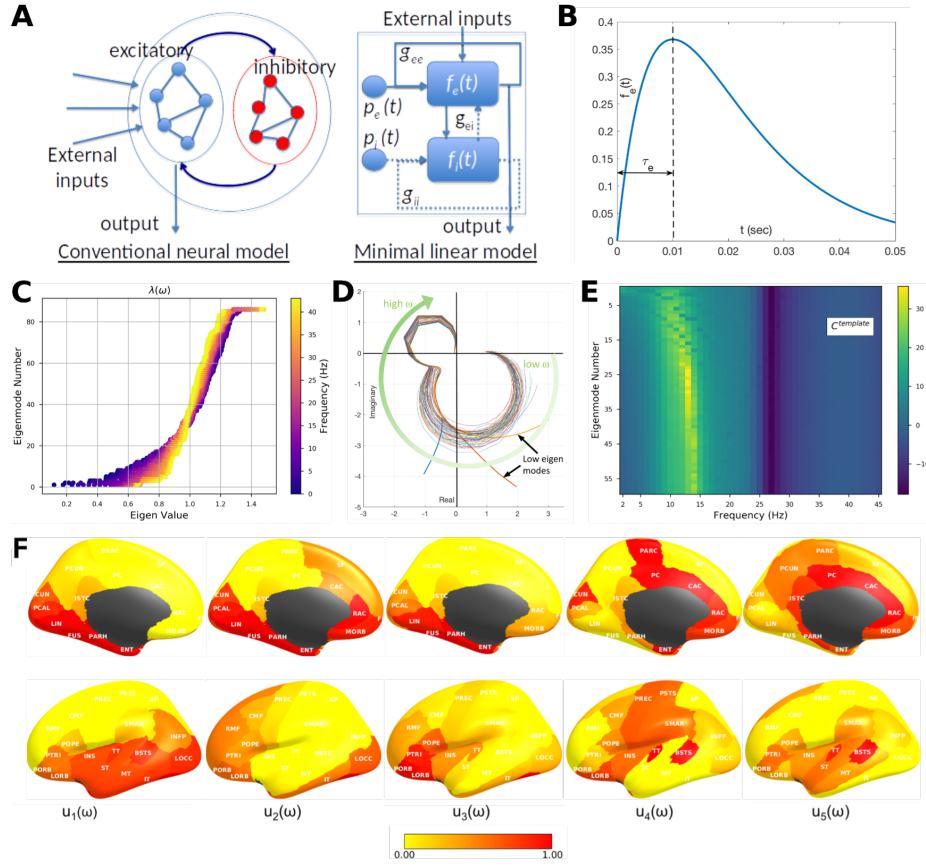


Figure 5.1: The linearized spectral graph model.

(a) Conventional neural mass models instantiate a large assembly of excitatory and inhibitory neurons, which are modeled as fully connected internally. External inputs and outputs are gated through the excitatory neurons only, and inhibitory neurons are considered strictly local. The proposed linear model condenses these local assemblies into lumped linear systems $f_e(t)$ and $f_i(t)$, Gamma-shaped functions having time constants τ_e and τ_i (see panel (b)). The recurrent architecture of the two pools within a local area is captured by the gain terms g_{ee} , g_{ii} , g_{ei} , parameterizing the recurrences within excitatory, inhibitory and cross-populations. (c) The absolute value of eigenvalues of the complex Laplacian $\mathcal{L}(\omega)$ are plotted against the eigenvector index. Each dot represents one eigenvalue $\lambda(\omega)$; its color represents the frequency ω - low (blue) to high (yellow). These eigenvalues change by frequency; small eigenvalues change more compared to large ones. (d) Frequency response of each eigenmode plotted on the complex plane with default model parameters and a template structural connectome. Each curve represents the transit in the complex plane of a single eigenmode's frequency response, starting at low frequencies in the bottom right quadrant, and moving to the upper left quadrant at high frequencies. The magnitude of the response, given by the distance from the origin, suggests that most eigenmodes have two prominent lobes, roughly corresponding to lower frequency alpha rhythms and higher frequency gamma rhythms. In contrast, the lowest eigenmodes start off far from the origin, indicative of a low-pass response. (e) Magnitude of the frequency response of each eigenmode reinforces these impressions more clearly, with clear alpha peak, as well as slower rhythms. (f) The spatial patterns of the top 5 eigenmodes of $\mathcal{L}(\omega)$, evaluated at the alpha frequency. The first 5 eigenmodes $u_1 \dots u_5$ produce resting-state functional networks patterns; These patterns are not exclusive and greatly depend on the frequency, model parameters, and the connectome.

5.2 Methods

5.2.1 Spectral graph model development

Notation. In our notation, vectors and matrices are represented by boldface, and scalars by normal font. We denote frequency of a signal, in Hertz, by symbol f , and the corresponding angular frequency as ($\omega = 2\pi f$). The connectivity matrix is denoted by $\mathbf{C} = \{c_{jk}\}$, consisting of connectivity strength c_{ij} between any two pair of regions j, k .

Model summary: Details of the Spectral Graph model (SGM) is described in detail below. There are very few model parameters, seven in total: $\tau_e, \tau_i, \tau_G, v, g_{ii}, g_{ei}, \alpha$, which are all global and apply at every node. See Table 5.1 for their meaning, initial value and range. Note that the entire model is based on a single equation of graph dynamics, Eq 5.1, which is repeatedly applied to each level of the hierarchy. Here we used two levels: a mesoscopic level where connectivity is all-to-all, and a macroscopic level, where connectivity is measured from fiber architecture. In theory, this template could be refined into finer levels, where neural responses become increasingly non-linear, and connectivity becomes sparser and structured.

Canonical rate model over a graph. We use a canonical rate model to describe neural activity across two hierarchical levels – local cortical mesoscopic levels and long-range macroscopic levels. At each level of the hierarchy of brain circuits, we hypothesize a simple linear rate model of recurrent reverberatory activity given by

Table 5.1: SGM parameters values and limits

Name	Symbol	Default Value	Optimizaiton Bounds
Excitatory Time constant	τ_e	12 ms	[5ms, 20ms]
Inhibitory Time constant	τ_i	3 ms	[5ms, 20ms]
Graph Time constant	τ_G	6 ms	[5ms, 20ms]
Excitatory gain	g_{ee}	1	n/a
Inhibitory gain	g_{ii}	1	[0.5, 5]
Excitatory gain	g_{ei}	4	[0.5, 5]
Transmission velocity	v	5 m/s	[5 m/s, 20 m/s]
Long-range connectivity coupling constant	α	1	[0.1, 1]

$$\frac{dx_{e/i}(t)}{dt} = -\frac{1}{\tau_{e/i}} f_{e/i}(t) * x_{e/i}(t) + \frac{1}{\tau_{e/i}} f_{e/i}(t) * \sum_{j,k} c_{jk} x_{e/i}(t - \tau_{jk}^v) + p_{e/i}(t) \quad (5.1)$$

where $x_{e/i}(t)$ is the mean signal of the excitatory/inhibitory populations and $p_{e/i}(t)$ is internal noise source reflecting local cortical column computations or input. The transit of signals, from pre-synaptic membranes, through dendritic arbors and axonal projections, is sought to be captured into ensemble average neural impulse response functions $f_e(t) = \frac{t}{\tau_e} \exp(-\frac{t}{\tau_e})$ and $f_i(t) = \frac{t}{\tau_i} \exp(-\frac{t}{\tau_i})$ respectively. We disregard the non-linearity of the neural response, hence the output at the terminal to a presynaptic input $u(t)$ is the simple convolution $x_e(t) = f_e(t) * u(t)$. The neural responses $f_{e/i}(t)$ are Gamma-shaped responses (Figure 5.1B) parameterized by time constants $\tau_{e/i}$ that here represent the end result of both synaptic membrane capacitance and the distribution of dendritic/axonal delays introduced by the arborization. NMMs typically use a single classical exponential decay term for membrane capacitance only, since NMMs model highly local cell assemblies where multisynaptic connections are infrequent and axonal and dendritic transport delays are usually incorporated explicitly via connectivity

weights and delays. Since our lumped model was designed for relatively large cortical regions, we employ the Gamma-shaped $f_{e/i}$ to capture not just classical membrane capacitance but also the expected diversity of dendritic transport delays. The dynamics of the entire assembly modeled via a self-decaying term $\tau_{e/i} \frac{dx}{dt} \propto -f_{e/i}(t) * \mathbf{x}(t)$, typically used in most rate or NMM models, but the difference here is that we chose to apply convolution with neural response $f_{e/i}(t)$ within the decay process. We believe this is necessary to ensure that the dynamics of the population cannot participate in the internal recurrent dynamics of the region until the signal has passed through one instance of the neuronal response. Since this neural response is meant to capture a distribution of local circuit delays, its time constants $\tau_{e/i}$ are purposefully far longer (up to 20ms) than expected from membrane capacitance alone. Studies of cortical lag times using paired electrode recordings between primary and higher cortices demonstrate this. A short visual stimulus causes a neural response in the ferret V1 within 20ms post-stimulus, in the primary barrel field within 16-36ms, and the entire visual cortex becomes engaged 48-70ms after stimulus [282]. Brief deflection of a single barrel whisker in the mouse evokes a somatotopically mapped cortical depolarization that remains localized to its C2 barrel column only for a few milliseconds, thence rapidly spreading to a large part of sensorimotor cortex within tens of milliseconds, a mechanism considered essential for the integration of sensory information [315, 316]. Interestingly, the evoked response curve in S1 from the ⁵⁰ study had a prominent Gamma shape. Of note, the duration of S1 response (~50ms) was considerably longer than the time to first sensory response in C2 (7.2ms) [315]. Interestingly, feedback projections from higher to lower areas take ~50ms, hence have a much slower apparent propagation velocity (0.15-0.25m/s) than what would be predicted by axonal conduction alone (1-3m/s) [282].

Individual neural elements are connected to each other via connection strengths c_{jk} . Let the cortico-cortical fiber conduction speed be v , which here is assumed to be a global constant independent of the pathway under question. For a given pathway connecting regions j and k of length d_{jk} , the conduction delay of a signal propagating from region j to region k will be given by $\tau_{jk}^v = \frac{d_{jk}}{v}$. Hence signals from neighboring elements also participate in the same recurrent dynamics, giving the second term of Eq 5.1. Equation 5.1 will serve as our canonical rate model, and will be reproduced at all levels of the hierarchy, and only the connectivity strengths will vary depending on the level of hierarchy we are modeling, as explained below.

Local neural assemblies. The local connectivities c_{jk}^{local} are assumed to be all-to-all, giving a complete graph. Further, the axonal delays τ_{jk}^v associated with purely local connections were already incorporated in the lumped impulse responses $f_{e/i}(t)$. Hence, we assert:

$$c_{jk}^{local} = c_{e/i}, \quad \tau_{jk}^v = 0, \quad \forall j, k \quad (5.2)$$

From spectral graph theory, a complete graph has all equal eigenvalues which allows the local network to be lumped into gain constants, and the summation removed. Indeed, rewriting $x_{e/i}(t)$ as the mean signal of all the excitatory/inhibitory cells and setting the gains $g_{ee} = 1 - c_e N_e$ and $g_{ii} = 1 - c_i N_i$ we get

$$\frac{dx_{e/i}(t)}{dt} = -\frac{g_{ee/ii}}{\tau_{e/i}} f_{e/i}(t) * x_{e/i}(t) + p_{e/i}(t) \quad (5.3)$$

Given the Fourier Transform pairs $\frac{d}{dt} \leftrightarrow j\omega$, $f_{e/i}(t) \leftrightarrow F_{e/i}(\omega) = \frac{1/\tau_{e/i}^2}{(j\omega + 1/\tau_{e/i})^2}$, we take the Fourier transform of Eq 5.1 and obtain the local assembly's frequency

spectrum:

$$X_{e/i}(\omega) = (j\omega + \frac{g_{ee/ii}}{\tau_{e/i}} F_{e/i}(\omega))^{-1} P_{e/i}(\omega) \quad (5.4)$$

Writing this in terms of transfer functions $X_e(\omega) = H_e(\omega)P_e(\omega)$, $X_i(\omega) = H_i(\omega)P_i(\omega)$ we get the lumped local system illustrated in Figure 5.1. Finally, we must also account for signals that alternate between the two populations, which is given by the transfer function

$$H_{ei}(\omega) = H_e(\omega)H_i(\omega)/(1 + g_{ei}H_e(\omega)H_i(\omega)) \quad (5.5)$$

We fix $g_{ee} = 1$ without loss of generality, and let the other terms g_{ii}, g_{ei} be model parameters to be fitted. Finally, the total cortical transfer function is the sum

$$H_{local}(\omega) = H_e(\omega) + H_i(\omega) + H_{ei}(\omega) \quad (5.6)$$

and $X_{local}(\omega) = H_{local}(\omega)P(\omega)$ represents all neural activity in this region, whether from excitatory or inhibitory cells. The canonical local activity is therefore defined by the Fourier transform pair: $x_{local}(t) \leftrightarrow X_{local}(\omega)$.

5.2.2 Macroscopic scale: signal evolution on the entire graph

For the macroscopic level, we use the same canonical network dynamics as Eq 5.1, but now the inter-regional connectivity c_{jk} is non-zero and given by the struc-

tural connectome. Similarly, axonal conductance delays are determined by fiber length and conductance speed $\tau_{jk}^v = d_{jk}/v$. Further, the external driving signals at each node is the local neural activity $x_{local}(t)$ defined above rather than a noise process $p(t)$. In the interest of parsimony we set each node of the macroscopic graph to have the same internal power spectrum $X_{local}(\omega)$ - i.e. all regions are experiencing the same transfer function, driven by identically distributed (but of course not identical) noise. At this scale, activity measured at graph nodes is no longer excitatory or inhibitory, but mixed, and the corticocortical connections are all between long, pyramidal excitatory-only cells. Thus, for the k -th node

$$\frac{dx_k(t)}{dt} = -\frac{1}{\tau_G} f_e(t) * x_k(t) + \frac{\alpha}{\tau_G} f_e(t) * \sum_j c_{jk} x_j(t - \tau_{jk}^v) + x_{local,k}(t) \quad (5.7)$$

Here we have introduced a global coupling constant α , similar to most connectivity-coupled neural mass models, that seeks to control the relative weight given to long-range afferents compared to local signals. We have also introduced a new time constant, τ_G , which is an excitatory time constant and it may be the same as the previously used constant τ_e . However, we allow the possibility that the long-range projection neurons might display a different capacitance and morphology compared to local circuits, hence we have introduced τ_G (subscript G is for “graph” or “global”).

Stacking all equations from all nodes and using vector valued signals $\mathbf{x}(t) = x_k(t)$, we can write

$$\frac{d\mathbf{x}(t)}{dt} = -\frac{1}{\tau_G} f_e(t) * \mathbf{x}(t) + \frac{\alpha}{\tau_G} f_e(t) * C\{\mathbf{x}(t - \tau_{jk}^v)\} + \mathbf{x}_{local}(t) \quad (5.8)$$

where the braces $\{\cdot\}$ represent all elements of a matrix indexed by j, k .

We wish to evaluate the frequency spectrum of the above. In Fourier space, delays become phases; hence we use the transform pairs $\frac{dx}{dt} \leftrightarrow j\omega \mathbf{X}(\omega)$ and $\mathbf{x}(t - \tau) \leftrightarrow e^{-j\tau\omega} \mathbf{X}(\omega)$. Therefore, define a "complex connectivity matrix" at any given angular frequency ω as $\mathbf{C}^*(\omega) = c_{jk} \exp(-j\omega\tau_{jk}^v)$. We then define a normalized complex connectivity matrix at frequency ω as

$$C(\omega) = \text{diag}\left(\frac{1}{\deg}\right)\mathbf{C}^*(\omega) \quad (5.9)$$

where the degree vector \deg is defined as $\deg_k = \sum_j c_{jk}$. Taking the Fourier transform of Equation 5.8, we get

$$(j\omega \mathbf{X}(\omega) + \frac{1}{\tau_G} F_e(\omega)(\mathbf{I} - \alpha C(\omega))\mathbf{X}(\omega)) = H_{local}(\omega)\mathbf{P}(\omega) \quad (5.10)$$

where we assumed identically distributed noise signals driving both the excitatory and inhibitory local populations at each node, such that $P_{e,k}(\omega) = P_{i,k}(\omega) = P_k(\omega)$ at the k -th node. We then collected all nodes' driving inputs in the vector $\mathbf{P}(\omega) = P_k(\omega), \forall k$. Here, we define the complex Laplacian matrix

$$\mathcal{L}(\omega) = \mathbf{I} - \alpha C(\omega) \quad (5.11)$$

where \mathbf{I} is the identity matrix of size $N \times N$. This complex Laplacian will be evaluated via the eigen-decomposition

$$\mathcal{L}(\omega) = \mathbf{U}(\omega)\Lambda(\omega)\mathbf{U}(\omega)^H \quad (5.12)$$

where $\Lambda(\omega) = \text{diag}([\lambda_1(\omega), \dots, \lambda_N(\omega)])$ is a diagonal matrix consisting of the

eigenvalues of the complex Laplacian matrix of the connectivity graph $C(\omega)$, at the angular frequency ω .

Hence

$$\mathbf{X}(\omega) = (j\omega \mathbf{I} + \frac{1}{\tau_G} F_e(\omega) \mathcal{L}(\omega))^{-1} H_{local}(\omega) \mathbf{P}(\omega) \quad (5.13)$$

where we invoke the eigen-decomposition of $\mathcal{L}(\omega)$, and that $\mathbf{U}(\omega)\mathbf{U}(\omega)^H = \mathbf{I}$.

It can then be shown easily that

$$\mathbf{X}(\omega) = \sum_i \frac{\mathbf{u}_i(\omega) \mathbf{u}_i^H(\omega)}{j\omega + \frac{1}{\tau_G} \lambda_i(\omega) F_e(\omega)} H_{local}(\omega) \mathbf{P}(\omega) \quad (5.14)$$

This is the steady state frequency response of the whole brain dynamics. In steady state, we assume that each cortical region is driven by internal noise that spans all frequencies, i.e. white noise. Hence, we assume that the driving function $\mathbf{p}(t)$ is an uncorrelated Gaussian noise process, such that $\mathbf{P}(\omega) = \mathbb{I}$ where \mathbb{I} is a vector of ones. This asserts identical cortical responses at each brain region.

5.2.3 Experimental Procedures

Study cohort. We acquired MEG, anatomical MRI, and diffusion MRI for 36 healthy adult subjects (23 males, 13 females; 26 left-handed, 10 right-handed; mean age 21.75 years (range: 7-51 years). All study procedures were approved by the institutional review board at the University of California at San Francisco (UCSF) and are in accordance with the ethics standards of the Helsinki Declaration of 1975 as revised in 2008.

MRI. A 3 Tesla TIM Trio MR scanner (Siemens, Erlangen, Germany) was

used to perform MRI using a 32-channel phased-array radiofrequency head coil. High-resolution MRI of each subject's brain was collected using an axial 3D magnetization prepared rapid-acquisition gradient-echo (MPRAGE) T1-weighted sequence (echo time [TE] = 1.64 ms, repetition time [TR] = 2530 ms, TI = 1200 ms, flip angle of 7 degrees) with a 256-mm field of view (FOV), and 160 1.0-mm contiguous partitions at a 256×256 matrix. Whole-brain diffusion weighted images were collected at $b = 1000 \text{ s/mm}^2$ with 30 directions using 2-mm voxel resolution in-plane and through-plane.

Magneto-encephalography (MEG) data. MEG recordings were acquired at UCSF using a 275-channel CTF Omega 2000 whole-head MEG system from VSM MedTech (Coquitlam, BC, Canada). All subjects were instructed to keep their eyes closed for five minutes while their MEGs were recorded at a sampling frequency of 1200 Hz.

5.2.4 Data Processing

Region Parcellations. The T1-weighted images were parcellated into 68 cortical regions and 18 subcortical regions using the Desikan-Killiany atlas available in the FreeSurfer software [237]. To do this, the subject specific T1-weighted images were back-projected to the atlas using affine registration, as described in our previous studies [228, 317].

Structural Connectivity Networks. We constructed different structural connectivity networks with the same Desikan-Killiany parcellations to access the capabilities of our proposed model. Firstly, we obtained openly available diffusion MRI data from the MGH-USC Human Connectome Project to create an

average template connectome. As in our previous studies [228, 317], subject specific structural connectivity was computed on diffusion MRI data: *Bedpostx* was used to determine the orientation of brain fibers in conjunction with *FLIRT*, as implemented in the *FSL* software [116]. In order to determine the elements of the adjacency matrix, we performed tractography using *probtrackx2*. We initiated 4000 streamlines from each seed voxel corresponding to a cortical or subcortical gray matter structure and tracked how many of these streamlines reached a target gray matter structure. The weighted connection between the two structures $c_{i,j}$, was defined as the number of streamlines initiated by voxels in region i that reach any voxel within region j , normalized by the sum of the source and target region volumes ($c_{i,j} = \frac{\text{streamlines}}{v_i + v_j}$). This normalization prevents large brain regions from having high connectivity simply due to having initiated or received many streamlines. Afterwards, connection strengths are averaged between both directions ($c_{i,j}$ and $c_{j,i}$) to form undirected edges. It is common in neuroimaging literature to threshold connectivity to remove weakly connected edges, as this can greatly influence the implied topology of the graph. In our work, we chose not to apply further thresholding, as unlike conventional graph theoretic metrics, linear models of spread and consequently network eigenmodes are relatively insensitive to implied topology induced by presence (or lack) of weak nonzero connections. However, to determine the geographic location of an edge, the top 95% of non-zero voxels by streamline count were computed for both edge directions. The consensus edge was defined as the union between both post-threshold sets.

MEG processing and source reconstruction. MEG recordings were down-sampled from 1200 Hz to 600 Hz, then digitally filtered to remove DC offset and any other noisy artifact outside of the 1 to 160 Hz bandpass range. Since

MEG data are in sensor space, meaning they represent the signal observable from sensors placed outside the head, this data needs to be “inverted” in order to infer the neuronal activity that has generated the observed signal by solving the so-called inverse problem. Several effective methods exist for performing *source localization* [318, 319, 320]. Here we eschew the common technique of solving for a small number of discrete dipole sources which is not fully appropriate in the context of inferring resting state activity, since the latter is neither spatially sparse nor localized. Instead, we used adaptive spatial filtering algorithms from the NUTMEG software tool written in house [321] in MATLAB (The MathWorks, Inc., Natick, Massachusetts, United States). To prepare for source localization, all MEG sensor locations were co-registered to each subject’s anatomical MRI scans. The lead field (forward model) for each subject was calculated in NUTMEG using a multiple local-spheres head model (three-orientation lead field) and an 8 mm voxel grid which generated more than 5000 dipole sources, all sources were normalized to have a norm of 1. Finally, the MEG recordings were projected into source space using a beamformer spatial filter. Source estimates tend to have a bias towards superficial currents and the estimates are more error-prone when we approach subcortical regions, therefore, only the sources belonging to the 68 cortical regions were selected to be averaged around the centroid. Specifically, all dipole sources were labeled based on the Desikan-Killiany parcellations, then sources within a 20 mm radial distance to the centroid of each brain region were extracted, the average time course of each region’s extracted sources served as empirical resting-state data for our proposed model.

Alternative benchmark model for comparison. In order to put the proposed model in context, we also implemented for comparison a Wilson-Cowan neural mass model [293, 305, 167] (add criticism citation here) with similar dimensional-

ity. Although NMMs like this can and have been implemented with regionally varying local parameters, here we enforced uniform, regionally non-varying local parameters, meaning all parcellated brain regions shared the same local and global parameters. This is a fair comparison since the proposed model is also regionally non-varying. The purpose of this exercise is to ascertain whether a non-regional NMM can also predict spatial power variations purely as a consequence of network transmission, like the proposed model, using the same model optimization procedure (see below). This NMM incorporates a transmission velocity parameter that introduces a delay based on fiber tract lengths extracted from diffusion MRI, but, unlike our model, does not seek to explicitly evaluate a frequency response based on these delays.

5.2.5 Model Optimization

We computed *maximum a posteriori* estimates for parameters under a flat non-informative prior. A simulated annealing optimization algorithm was used for estimation and provided a set of optimized parameters $\{\tau_e, \tau_i, \tau_c, g_{ei}, g_{ii}, \alpha, v\}$. We defined a data likelihood or goodness of fit (GOF) as the Pearson correlation between empirical source localized MEG power spectra and simulated model power spectra, averaged over all 68 regions of a subject's brain. The proposed model has only seven global parameters as compared to neural mass models with hundreds of parameters, and is available in closed-form. To improve the odds that we capture the global minimum, we chose to implement a probabilistic approach of simulated annealing [206]. The algorithm samples a set of parameters within a set of boundaries by generating an initial trial solution and choosing the next solution from the current point by a probability distribution with a scale

depending on the current “temperature” parameter. While the algorithm always accepts new trial points that map to cost-function values lower than the previous cost-function evaluations, it will also accept solutions that have cost-function evaluations greater than the previous one to move out of local minima. The acceptance probability function is $1/(1 + \frac{\Delta}{e^{\max(T)}})$, where T is the current temperature and Δ is the difference of the new minus old cost-function evaluations. The initial parameter values and boundary constraints for each parameter are given in Table 5.1. All simulated annealing runs were allowed to iterate over the parameter space for a maximum of $N_p \times 3000$ iterations, where N_p is the number of parameters in the model. As a comparison, we performed the same optimization procedure to a regionally non-varying Wilson-Cowan neural mass model [305, 167].

5.3 Results

5.3.1 Graph Laplacian eigenmodes mediate a diversity of frequency responses

First, we demonstrate the spectra produced by graph eigenmodes as per our theory using default choices of model parameters. Figure 5.1C shows the eigen-spectrum of the complex Laplacian, with eigenvalue magnitude ranging from 0 to 1. The absolute value of eigenvalues of the complex Laplacian $\mathcal{L}(\omega)$ are plotted against the eigenvector index. Each dot represents one eigenvalue $\lambda(\omega)$; its color represents the frequency ω - low (blue) to high (yellow). Clearly, these eigenvalues change somewhat by frequency. Small eigenvalues undergo a larger

shift due to frequency, while the large ones stay more stable and tightly clustered around the nominal eigenvalue (i.e. at $\omega = 0$). Each eigenmode produces a frequency response based on its frequency-dependent eigenvalue (Figure 5.1D, E). Figure 5.1D shows the transit in the complex plane of a single eigenmode's frequency response, starting at low frequencies in the bottom right quadrant, and moving to the upper left quadrant at high frequencies. The magnitude, given by distance from origin, suggests that most eigenmodes have two prominent lobes, one roughly corresponding to lower frequency alpha rhythm and another corresponding to higher frequency beta or gamma rhythms, respectively. In contrast, the lowest few eigenmodes start off far from the origin, indicative of a low-pass response. The magnitude of these complex-valued curves shown in Figure 5.1E reinforces these impressions, with clear alpha peak, as well as slower rhythms of the lowest eigenmodes. The spectral profile of the eigenmodes, especially the peak frequencies, are sensitive to the choice of model parameters as demonstrated below.

The spatial patterns of the first 5 eigenmodes of $\mathcal{L}(\omega)$, evaluated at the alpha peak of 10 Hz, are shown in Figure 5.1F. Eigenmodes \mathbf{u}_{1-4} produce posterior and temporal spatial patterns, including many elements of the **default mode network**; \mathbf{u}_4 resembles the **sensorimotor network**; and \mathbf{u}_5 the **structural core** of the human connectome. However, these patterns are not exclusive and greatly depend on the frequency at which they are evaluated, as well as the model parameters. Higher eigenmodes are especially sensitive to axonal velocity and frequency (not shown here).

Since the spectral graph model (SGM) relies on connectome topology, we demonstrate in Figure 5.2 that different connectivity matrices produce different

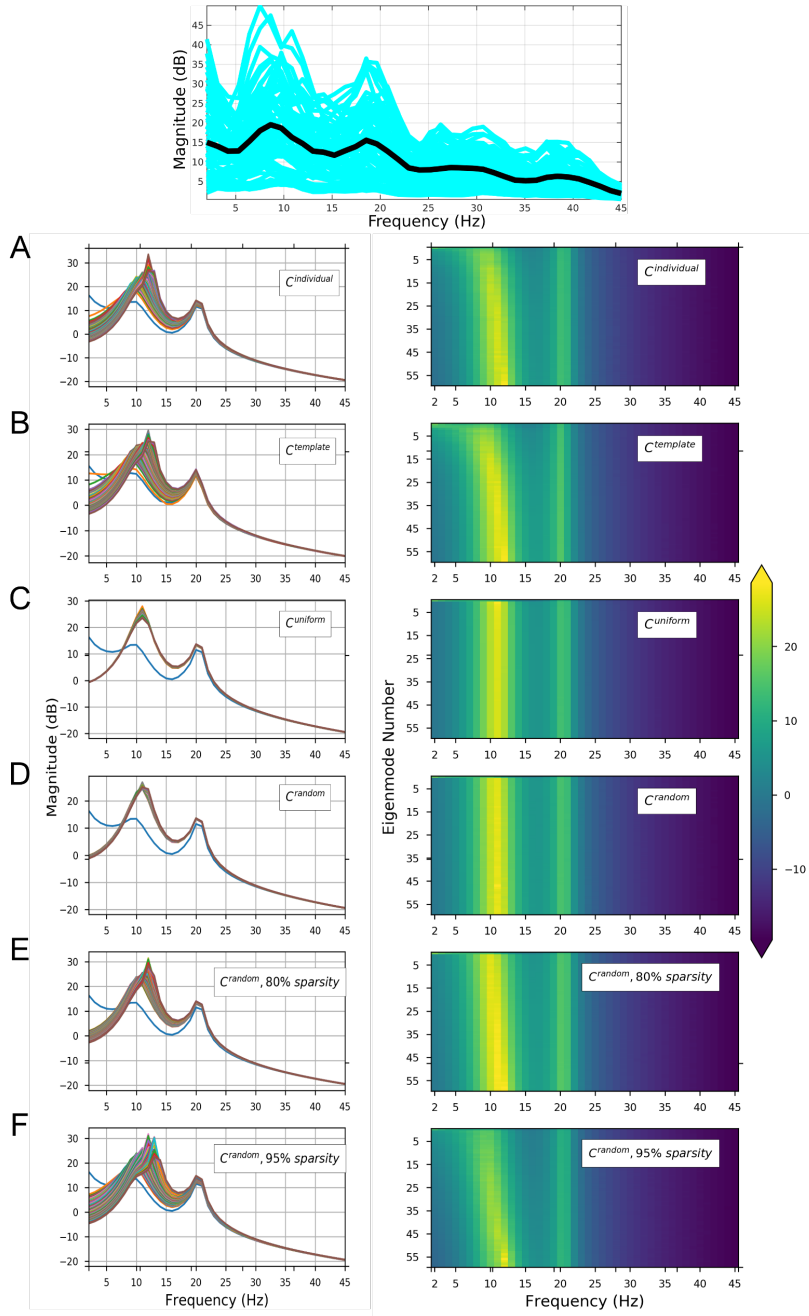


Figure 5.2: Spectral graph model spectra for one subject.

Top-Source localized MEG power spectrum for 68 parcellated brain regions. Estimated spectra for each brain region are shown in blue, and average spectrum across all regions is shown in black. The subsequent rows show each eigenmode's spectral magnitude response with model parameters optimized to match the MEG spectrum ($\tau_e = 0.0073$, $\tau_i = 0.0085$, $\tau_G = 0.0061$, $g_{ei} = 2.9469$, $g_{ii} = 4.4865$, $v = 18.3071$, and $\alpha = 0.4639$). Left column shows each eigenmode's frequency responses, while the right column shows the same information as heatmaps. (a) Model using subject's individual structural connectome. (b) Model using average template connectome obtained from 80 HCP subjects. (c) Model using uniform connectivity matrix of ones. (d) Model using randomized connectivity matrix with 75% sparsity. (f) Model using randomized connectivity matrix with 95% sparsity.

frequency responses: A) the individual's structural connectivity matrix, B) HCP average template connectivity matrix, C) uniform connectivity matrix of ones, D) a randomly generated matrix, E) and F) are randomly generated matrices with 75% and 95% sparsity respectively. For Figure 5.2A, optimized parameters for the individual subject's connectome were used. For Figures 5.2B-F, parameters optimized for the HCP template were used. We can observe the spectral profile of the eigenmodes, especially the peak frequencies, are sensitive to the choice of the connectome and the model parameters. All modeled power spectra show a broad alpha peak at around 10 Hz and a narrower beta peak at around 20 Hz. This is expected, since these general spectral properties are governed by the local linearized rate model. It is important to note that different eigenmodes accommodate a diversity of frequency responses; for instance, the lowest eigenmodes show a low-frequency response with no alpha peak whatsoever. In all cases the connectome modulates the spectral response in delta-theta range, leaving the higher gamma frequencies unchanged. Particularly, the low eigenmodes ($\mathbf{u}_1 \dots \mathbf{u}_{20}$) appear to modulate the lower frequency range, up to beta, and may be considered responsible for the diversity of spectra observed in the model. In the frequency responses from biologically realistic individual and HCP template connectomes, there is a diversity of spectral responses amongst eigenmodes that is lacking in the response produced by the unrealistic uniform and randomized connectivity matrices. As we will see below, graph topology is critical to the power spectrum it induces, hence we explored whether and how sparsity of random graphs mediates spectral power (Figure 5.2D-F). At incrementally increasing sparsity levels, the diversity of spectral responses of different eigenmodes increases and approaches that of realistic connectomes. Therefore, graph eigenmodes induce unique and diverse frequency responses that depend on the

topology of the graph.

5.3.2 Spectral distribution of MEG power depends on model parameters but not connectivity

Network eigenmodes exhibit strong spatial patterning in their frequency responses, even with identical model parameters (Figure 5.3). We evaluated the model spectral response using the subject-specific C^{ind} matrices of 4 representative subjects (Figure 5.3A). The model power spectra strikingly resemble empirical MEG spectra, displaying both the alpha and beta peaks on average, and similar regional variability as in real data.

Regional averages of empirical and modeled power spectra of the entire group after full parameter optimization over individual subjects are shown in Figure 5.3B. The model closely replicates the observed power spectrum (red circles) equally well with both C^{ind} (black triangles) and C^{HCP} (purple triangles). Thus, in most cases we can safely replace the subject-specific connectome with the template connectome. In contrast, when non-optimized average parameters were used (golden green triangles), it resulted in a worse fit, especially at high frequencies, suggesting that individualized parameter optimization is essential to produce realistic spectra. We also examined the model behavior for a random connectomes with 80% sparsity (bright green triangles), or a distance-based connectome (blue triangles) was chosen with identical sparsity (80%) to the actual connectome, and found that even with optimized parameters the average spectra could be accounted for by these connectomes.

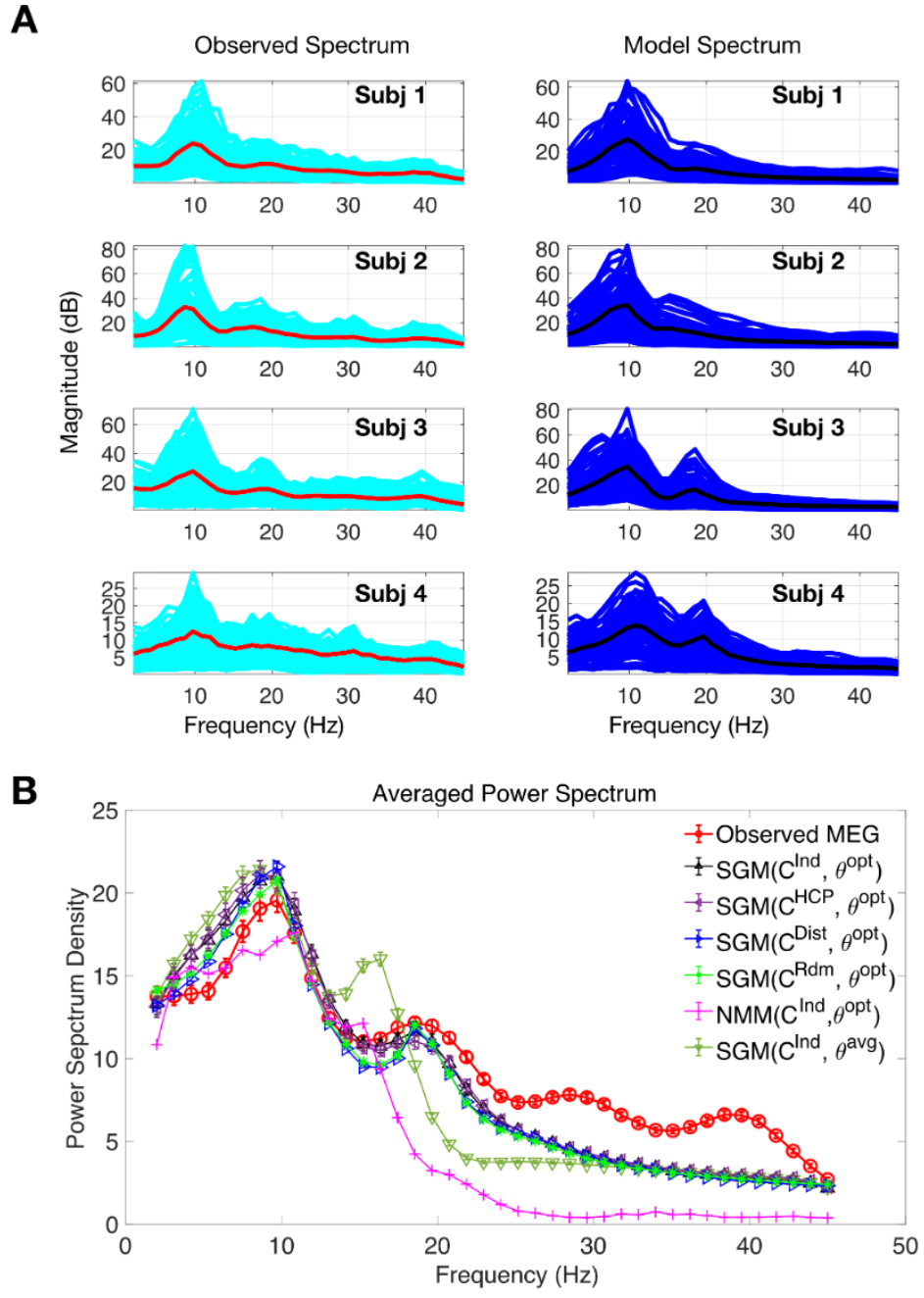


Figure 5.3: Spectral graph model depicts MEG spectra.

(a) The observed spectra and SGM's simulated spectra for four representative subjects. Red and cyan curves illustrate source localized empirical average spectra and region-wise spectra respectively. Black and blue curves illustrate simulated average spectra and region-wise spectra respectively. (b) Average observed spectrum across subjects is shown in red. Subsequently, we show average simulated spectra with optimized parameters for individual subject connectomes (black), HCP template connectome (purple), 80% sparse distance connectome (blue), 80% sparse random connectome (green). As a comparison, we also show simulated spectrum with a network neural mass model (pink) and average parameter values and individual connectome (green).

As another benchmark for comparison, a non-linear network neural mass model [16, 167] (add criticism paper) using our in-house MATLAB implementation, was generally able to produce characteristic alpha and beta frequency peaks, but this model does not resemble empirical wideband spectra. Note that no regionally-varying NMM parameters were used in order to achieve a proper comparison with our model, but both models were optimized with the same algorithm.

Figure 5.4A shows violin plots of the optimized values, indicating that there is a large range of individually optimal model parameters across subjects. The time constants τ_e, τ_i showed tight clustering but the rest of the parameters showed high variability across subjects. The optimal parameters are in a biologically plausible range, similar to values reported in numerous neural mass models. The optimization algorithm aimed to maximize a cost function proportional to the posterior likelihood of the model, and was quantified by the Pearson's correlation between MEG and modeled spectra ("Spectral correlation"). The convergence plots shown in Figure 5.4B, one curve for each subject, indicates substantial improvement in cost function from default choice as optimization proceeds. The distribution of optimized spectral correlations is shown in Figure 5.4C. Other model choices were evaluated for comparison: SGM on random connectomes with 80 and 95% sparsity, with and without a distance effect described in Methods, and SGM applied with average optimal model parameters instead of individually optimized ones. In order to test for significance, Fisher's R to z transform was applied, followed by a paired t-test across all subjects between the optimal SGM and other models. The spectral fits for an SGM model with individual connectomes were significantly better than SGM models with average parameters, no matter what connectomes were chosen ($p < 0.001$). Interestingly,

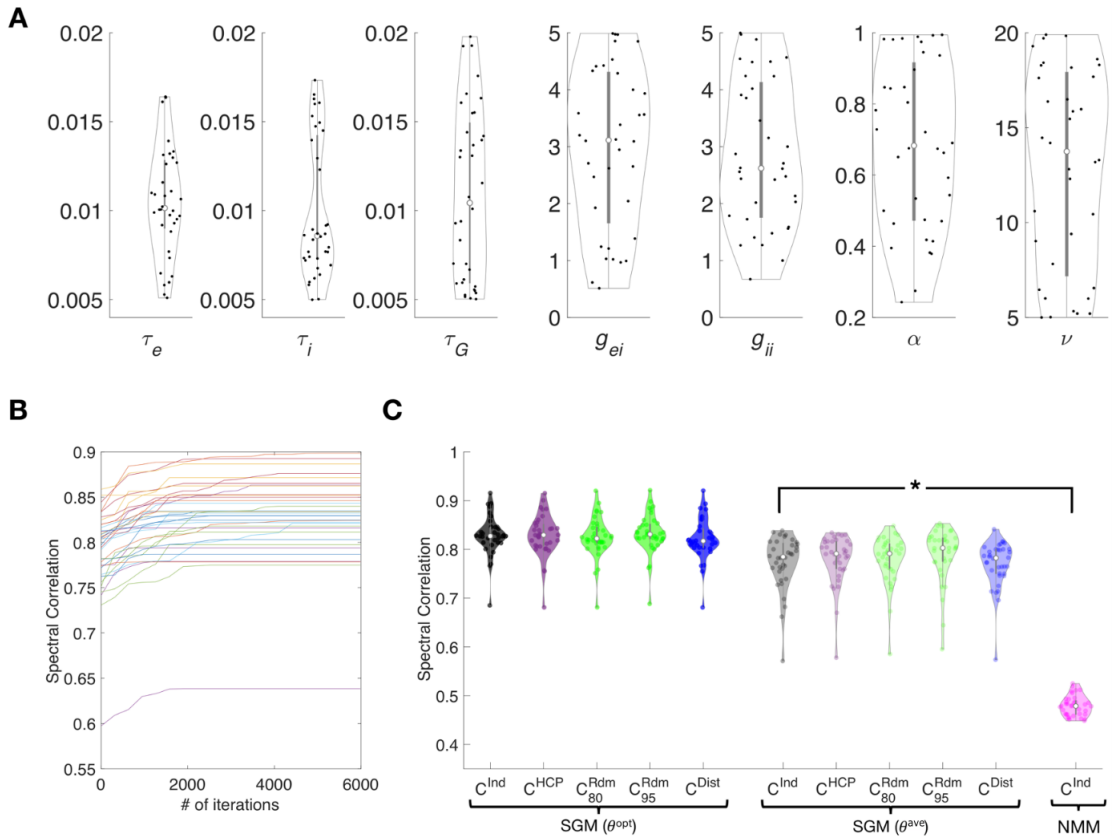


Figure 5.4: Spectral graph model parameter optimization.

(a) Distribution of optimized model parameter values across all 36 subjects for parameters $\{\tau_e, \tau_i, \tau_c, g_{ei}, g_{ii}, \alpha, \nu\}$ are shown in violin plots. (b) Performance of optimization algorithm. Spectral Pearson's correlation between simulated and MEG spectra at each iteration. Each curve shows the spectral correlation achieved by the model optimized for a single subject. (c) Distribution of spectral correlation between optimized model and observed spectra across subjects. Correlations with optimized parameters and 5 various connectomes are shown in the left-most columns. Correlations with average parameter values and the same connectomes are shown in the middle section. SGM model outperforms an optimized network NMM regardless of connectome type as denoted by asterisk ($p < 0.001$).

spectral fits for SGM model were comparable across all connectomes ($p > .05$). Furthermore, spectral fits for the SGM model were significantly better than that for NMM models with optimized parameters and individual connectome ($p < 1e^{-20}$). Therefore, we conclude that with the graph spectral model, the overall regional spectra appear to be dependent on global model parameters rather than on the actual structural connectome.

5.3.3 Spectral graph model recapitulates the spatial distribution of MEG power

Next, we establish that the model is able to reproduce region-specific spectra, even though it uses identical local oscillations. We integrated the spectral area in the range 8-12 Hz for alpha and 13-25 Hz for beta, of each brain region separately. We define "*spatial correlation*" (as compared to spectral correlation above) as Pearson's R between the *regional distribution* of empirical MEG and model-predicted power within a given frequency band.

Small number of eigenmodes capture spatial distributions of alpha and beta band activity

We noticed during our experimentation that only a few eigenmodes appear to contribute substantially to observed MEG alpha and beta patterns. Hence we hypothesized that spatial correlations could be improved by selecting a small subset of eigenmodes. Therefore, we developed a sorting strategy whereby we

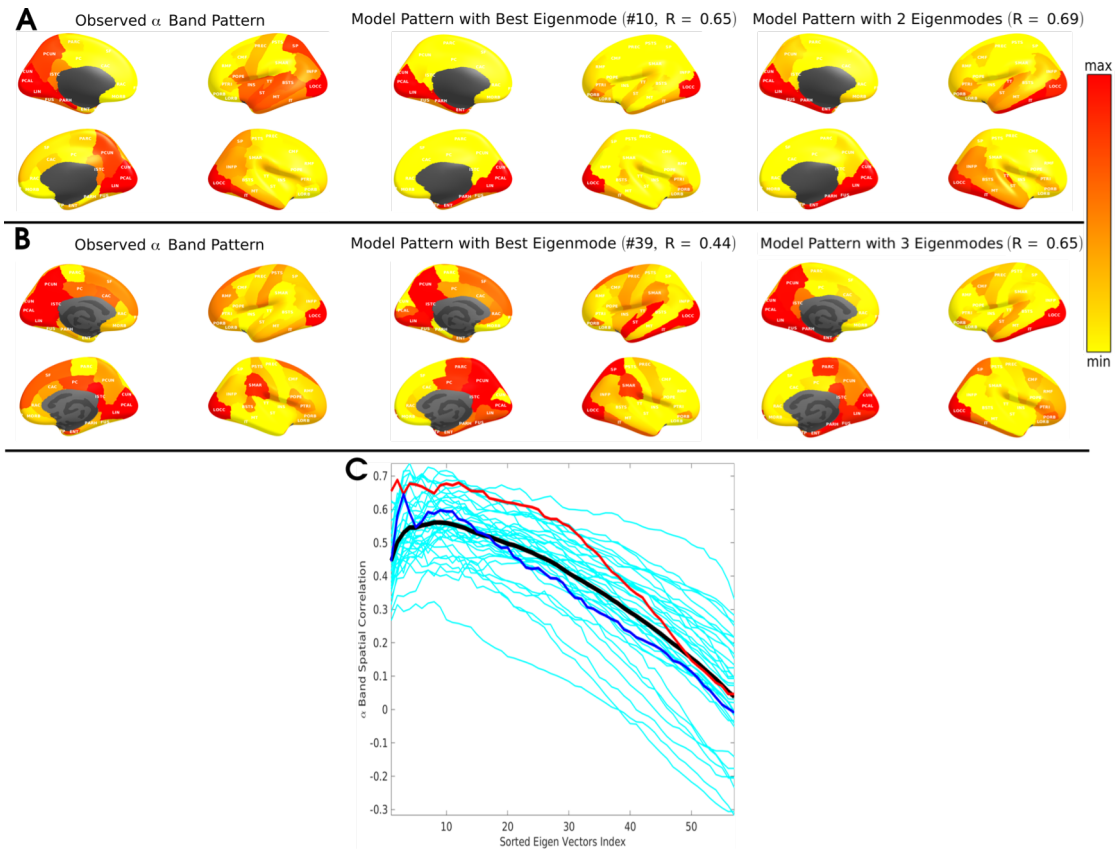


Figure 5.5: Alpha power spatial distribution depicted by specific spectral graph model eigenmodes.

(a,b) The spatially distributed patterns of alpha band power for two representative subjects are displayed in brain surface renderings. For each three brain panels shown, the medial surface rendering is shown on the left column while the lateral surface is rendered on the right, the left hemisphere is shown on top and the right hemisphere is shown in the bottom row. Left column: The observed MEG alpha band spatial distribution showing higher power in posterior regions of the brain. Middle column: Spatial distribution of the best matching eigenmode from the SGM. Right column: Spatial distribution of the best cumulative combination of eigenmodes from the SGM. (c) Alpha band spatial correlation for all subjects from SGM simulations with increasing number of cumulative eigenmodes. Individual subject alpha band spatial correlations are shown in cyan ($n = 36$). Panels A and B correspond to the subjects indicated by red and blue curves respectively. Black curve is the average performance across all subjects.

first rank the eigenmodes in descending order of spatial correlation for a given subject and given frequency band. Then we perform summation over only these eigenmodes according to Eq 5.14, each time incrementally adding a new eigenmode to the sum. The spatial correlation of these "sorted-summed" eigenmodes against empirical alpha power are plotted in Figure 5.5C as a function of increasing number of eigenmodes; one curve for each subject. The thick black curve represents the average over all subjects. The spatial correlation initially increases as we add more well-fitting eigenmodes, but peaks around, and begins declining thereafter. Addition of the remaining eigenmodes only serves to reduce the spatial correlation. This behavior is observed in almost all subjects we studied.

Examples of predicted alpha patterns: Figure 5.5 shows brain surface renderings of the spatially distributed patterns of alpha band power for two representative subjects. Regions are color coded as a heatmap of regional power scaled by mean power over all regions. The observed MEG spatial distribution pattern of alpha band shows higher power in posterior regions of the brain, as expected, with strong effect size in temporal, occipital and medial posterior areas. This pattern is matched by one of the eigenmodes (#10, shown in middle panel, giving $R = 0.65$), and slightly better by a weighted combination of 2 eigenmodes ($R = 0.69$). However, the model did not reproduce parietal and parieto-occipital components seen in real data. The other subject produced similar results, but with 6 eigenmodes. In this instance, the parietal component seen in real data were reasonably reproduced by the model.

Examples of predicted beta patterns. Empirical beta power (Figure 5.6, left) is spread throughout the cortex, especially frontal and sensorimotor cortex. A combination of 4 and 6 best matching eigenmodes produced the best model

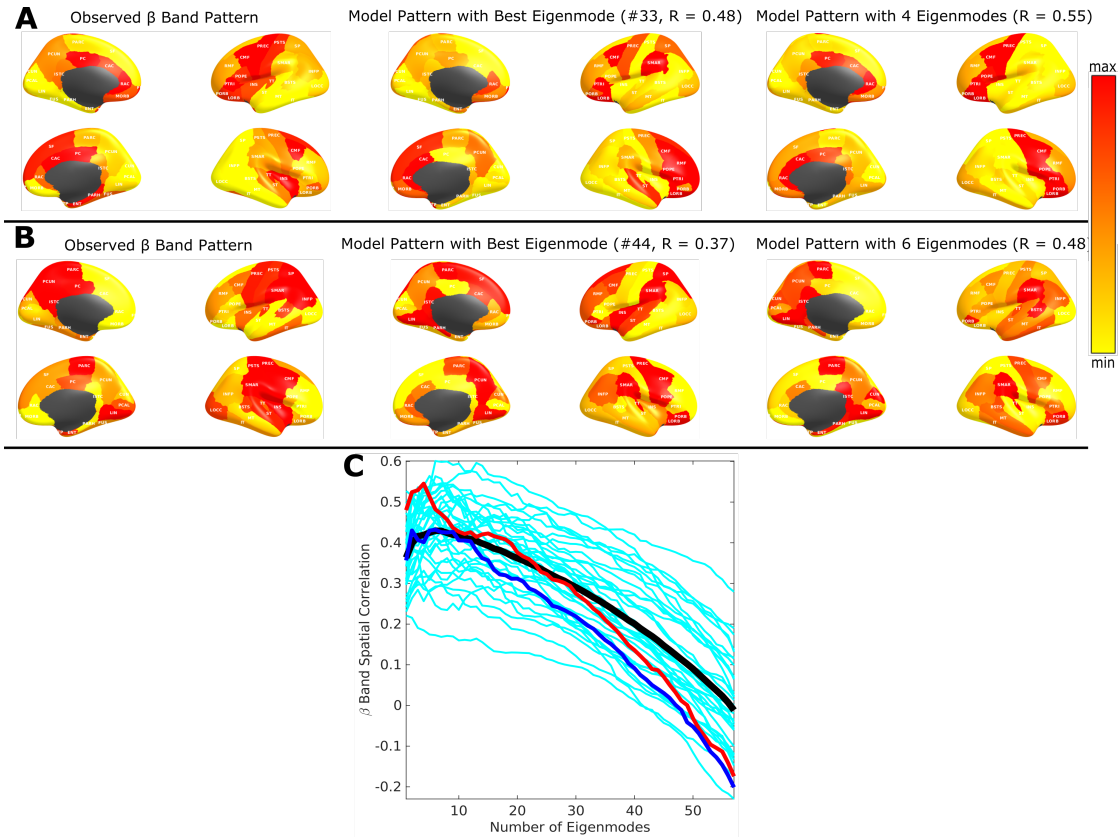


Figure 5.6: Beta power spatial distribution depicted by specific spectral graph model eigenmodes.

Legends and layout is identical to Figure 5.5 but shown for beta band spatial distributions.

match to the source localized pattern of two representative subjects, respectively, with $R = 0.55$ and $R = 0.48$. Figure 5.6C shows how the spatial correlation changes as more eigenmodes are used in the "sorted summed" computations, analogous to that of alpha pattern. Here too a peak is achieved for a small number of eigenmodes, typically under 10.

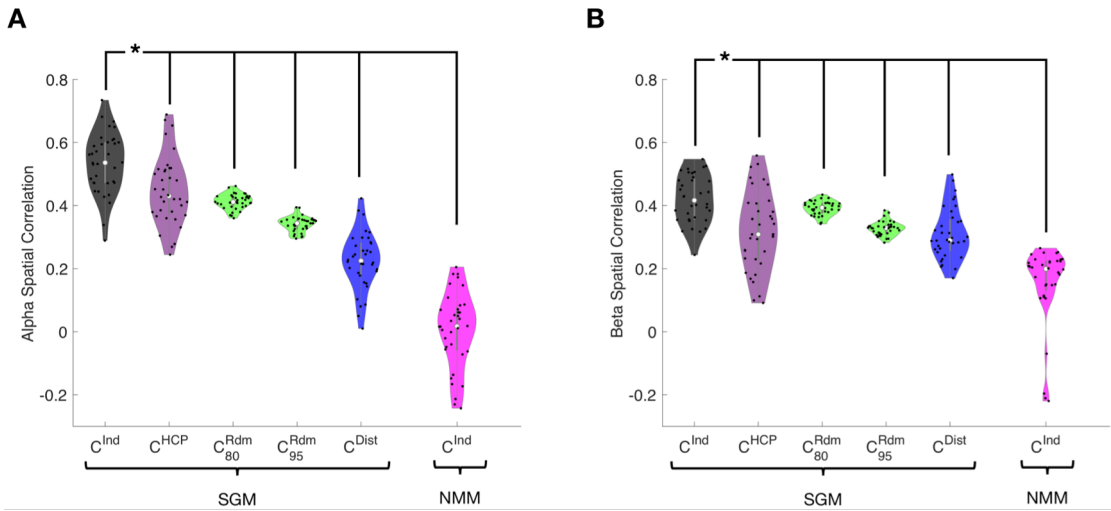


Figure 5.7: Spatial correlation performance of the SGM.

Distribution of the SGM for all subjects with the best performing eigenmode. (a) Alpha band spatial correlations. (b) Beta band spatial correlations. For both panels, spatial correlations are shown for SGM with subject individual connectomes (C^{ind} , black), random connectomes with 80% and 95% sparsity (green), geodesic distance based connectome (C^{dist} , blue), and finally for a NMM with specific individual connectome (pink). For each scenario, a selection of the best eigenmodes were obtained for spatial correlation calculations separately. Paired t-tests between SGM(C^{ind}) and all other model simulations show that the SGM with individual connectomes significantly outperform all other models; $p < 0.001$ for all alpha spatial correlations and $p < 0.012$ for all beta spatial correlations.

Spatial correlation achieved by the spectral graph model is significantly higher than alternative models

The distribution of peak spatial correlations in the alpha band, using optimized parameters and individual connectomes of all subjects, is plotted in Figure 5.7A. For comparison we show results for four model types: a) SGM on subject specific individual connectomes (C^{Ind} , black); b) SGM with the HCP template connectome (C^{HCP} , purple); c) SGM on random connectomes with 80% sparsity comparable to individual connectomes or with 95% sparsity where the model shows spectral diversity (C^{Rdm} , green); d) SGM on geodesic distance based connectomes (C^{Dist} , blue); and e) a Wilson-Cowan NMM with subject

specific individual connectome (C^{Ind} , pink). Analogous results for beta band spatial correlations are contained in Figure 5.7B. For each connectome model, a selection of the cumulative best set of eigenvectors were separately obtained for spatial correlation calculations. Across all subjects the proposed model, SGM on C^{Ind} , gives excellent spatial correlations in alpha band (R distribution centered at 0.6) as well as in the beta band (R distribution centered at 0.5).

Alternate non-linear model

The Wilson-Cowan neural mass model also did not succeed in predicting the spatial patterns of alpha or beta power, with poor correlations (r centered at 0). This could be because in our implementation we enforced uniform local parameters with no regional variability. However, this is the appropriate comparison, since our proposed model also does not require regionally-varying parameters. Interestingly, the random connectomes and geodesic distance based connectome also appear to have some ability to capture these spatial patterns (R centered at 0.4 and 0.2 respectively), perhaps due to the implicit search for best performing eigenmodes, which on average will give at least a few eigenmodes that look like MEG power purely by chance.

Collectively, we conclude that the graph model is able to fit both the spectral and spatial features of empirical source localized MEG data, and that the optimal fits performed on individual subjects occurs at widely varying subject-specific parameter choices.

5.4 Discussion

The proposed hierarchical graph spectral model of neural oscillatory activity is a step towards understanding the fundamental relationship between network topology and the macroscopic whole-brain dynamics. The objective is not just to model brain activity phenomenologically, but to analytically derive the mesoscopic laws that drive macroscopic dynamics. This model of the structure-function relationship has the following key distinguishing features: *(a) Hierarchical*: the model's complexity depends on the level of hierarchy being modeled: complex, non-linear and chaotic dynamics can be accommodated at the local level, but linear graph model is sufficient at the macro-scale. *(b) Graph-based*: Macroscopic dynamics is mainly governed by the connectome, hence linear approximations allow the steady-state frequency response to be specified by the graph Laplacian eigen-decomposition, borrowing heavily from **spectral graph theory** [308, 307, 306, 309]. *(c) Analytic*: The model is available in closed form, without the need for numerical simulations. *(d) Low-dimensional and parsimonious*: Simple, global and universal rules specified with a few parameters, all global and apply at every node, are able to achieve sufficiently complex dynamics. The model is incredibly easy to evaluate, taking no more than a few seconds per brain and to infer model parameters directly from a subject's MEG data. The optimized model matches observed spectral and spatial patterns in MEG data quite well. No time-consuming simulations of coupled neural masses or chaotic oscillators were needed; indeed, the latter greatly underperformed our model. We report several novel findings with potentially important implications, discussed below.

5.4.1 Recapitulating regional power spectra at all frequencies

Our main result is the robust demonstration of the model on 36 subjects' MEG data. The representative examples shown in Figures 5.3-5.6 indicate that the graph model recapitulates the observed source localized MEG power spectra for the 68 parcellated brain regions, reproducing the prominent alpha and beta peaks. For each region, the model is also able to predict some characteristics of the full bandwidth power spectra, including what appears to be an inverse power law fall-off over the entire frequency range of interest. However, this aspect will be quantitatively characterized in future work.

We designed a comprehensive parameter optimization algorithm on individual subjects' MEG data of a suitably defined cost function based on Pearson R statistic as a way to capture all relevant spectral features. Using this fitting procedure, we were able to obtain the range of optimally-fitted parameters across the entire study cohort. As shown in Figure 5.4A, the range is broad in most cases, implying that there is significant inter-subject variability of model parameters, even if a template connectome is used for all. We tested the possibility that a group-averaged parameter set might also succeed in matching real spectral data on individuals. But as shown in Figures 5.3B and 5.4C, this was found to be a poor choice, supporting the key role of individual variability of model parameters (but not variability in the connectome). However, no model is capable of reproducing higher frequencies in the higher beta and gamma range seen in MEG, since by design and by biophysical intuition these frequencies arise from local neural assemblies rather than from modulation by macroscopic networks.

5.4.2 Revealing sources of heterogeneity in spatial patterns of brain activity

The spatial match between model and data is strongest when the model uses empirical macroscopic connectomes obtained from healthy subjects' diffusion weighted MRI scans, followed by tractography. The use of "null" connectomes - randomized connectivity matrices of varying levels of sparsity and distance-based connectivity matrices, respectively, did far worse than actual human connectomes (Figure 5.7), supporting the fact that the latter is the key mediator of spatial patterns of real brain activity. The match was also significantly different when using a template HCP connectome versus the individual subject's own connectomes, and when compared to spatial patterns predicted by an NMM. In conclusion, for the purpose of predicting the spatial topography of brain activity, it is important to use individual connectomes and optimized model parameters.

5.4.3 Macroscopic brain rhythms are governed by the connec-tome

A predominant view assumes that different brain rhythms are produced by groups of neurons with similar characteristic frequencies, which might synchronize and act as "pacemakers". How could this view explain why alpha and beta power are spatially stereotyped across subjects, and why the alpha signal is especially prominent in posterior areas? Although practically any computer model of cortical activity can be tuned, with suitable parameter choice, to oscillate at alpha frequency, e.g. [281, 292, 295, 297, 252, 322, 323], none of them

are able to parsimoniously recapitulate the posterior origin of alpha. Thus the prominence of posterior alpha might be explained by the hypothesized existence of alpha generators in posterior areas. Indeed, most oscillator models of local dynamics are capable of producing these rhythms at any desired frequency [281, 252, 324, 325, 227], and therefore it is common to tweak their parameters to reproduce alpha rhythm. Local networks of simulated multicompartmental neurons can produce oscillations in the range 8–20 Hz [281], and, in a non-linear continuum theory, peaks at various frequencies in the range 2–16Hz were obtained depending on the parameters [325]. Specifically, the role of thalamus as pacemaker has motivated thalamocortical models [287, 292] that are capable of resonances in various ranges. Neural field models of the thalamocortical loop [292] can also predict slow-wave and spindle oscillations in sleep, and alpha, beta, and higher-frequency oscillations in the waking state. In these thalamocortical models, the posterior alpha can arise by postulating a differential effect in weights of the posterior versus anterior thalamic projections, e.g. [323]. Ultimately, hypotheses requiring local rhythm generators suffer from lack of parsimony and specificity: a separate pacemaker must be postulated for each spectral peak at just the right location [326].

An alternative view emerges from our results that macroscopic brain rhythms are governed by the structural connectome. Even with global model parameters, using the exact same local cortical dynamics captured by the local transfer function $H_{local}(\omega)$, driven by identically distributed random noise $\mathbf{P}(\omega)$, our model is capable of predicting prominent spectral (Figures 5.2, 5.3) and spatial (Figures 5.5,5.6) patterning that is quite realistic. This is especially true in the lower frequency range: indeed, the model is able to predict not just the frequency spectra in alpha and beta ranges, but also their spatial patterns – i.e. posterior alpha

and distributed but roughly frontal beta. Although this is not definitive proof, it raises the intriguing possibility that the macroscopic spatial distribution of the spectra of brain signals *does not require spatial heterogeneity of local signal sources, nor regionally variable parameters*. Rather, it implies that the most prominent *patterning of brain activity (especially alpha) may be governed by the topology of the macroscopic network* rather than by local, regionally-varying drivers. Nevertheless, a deeper exploration is required of the topography of the dominant eigenmodes of our linear model, in order to understand the spatial gradients postulated previously [292, 323].

5.4.4 Emergence of linearity from chaotic brain dynamics

The non-linear and chaotic dynamics of brain signals may at first appear to preclude deterministic or analytic modeling of any kind. Yet, vast swathes of neuroscientific terrain are surprisingly deterministic, reproducible and conserved across individuals and even species. Brain rhythms generally fall within identical frequency bands and spatial maps [280, 292, 304]. Based on the hypothesis that the emergent behavior of long-range interactions can be independent of detailed local dynamics of individual neurons [289, 290, 291, 293, 228], and may be largely governed by long-range connectivity [294, 295, 296, 297], we have reported here a minimal linear model of how the brain connectome serves as a spatial-spectral filter that modulates the underlying non-linear signals emanating from local circuits. Nevertheless, we recognize the limitations of a linear model and its inability to capture inherent non-linearities across all levels in the system.

5.4.5 Relationship to other work

One can view the proposed generative model as a biophysical realization of a dynamic causal model (DCM) [327, 328, 329, 264, 263] for whole brain electrophysiological activity but with very different goals, model dimensionality and inference procedures.

First, the goal of many prior efforts using DCMs is to examine effective connectivity in EEG, LFP and fMRI functional connectivity data, typically for smaller networks[263, 50], or dynamic effective connectivity[265, 267, 266]. Hence, they address the second order covariance structures of brain activity. In particular, recent spectral DCM and regression DCM models [270, 269, 268] with local neural masses are formulated in the steady-state frequency-domain, and the resulting whole-brain cross-spectra are evaluated. The goals of these models are to derive model cross-spectra that define the effective connectivity in the frequency domain and are compared with empirical cross-spectra. Based on second-order sufficient statistics, these models attempt to derive effective connectivity from functional connectivity data. These DCMs have so far only been applied to small networks or to BOLD fMRI regime. In contrast, our goal is to examine the role of the eigenmodes of the structural connectome and their influence on power spectral distributions in the full MEG frequency range, and over the entire whole brain. In subsequent work, we intend to extend our efforts to examining effective connectivity but such an effort currently remains outside the scope of the work in this paper. Here, we focus on models that directly estimate the first order effects of observed power spectra and its spatial distributions and compare them with empirical MEG source reconstructions. Our primary motivation is to examine whether spatial distribution of observed power spectra can arise from graph

structure of the connectome, hence our focus on the effects of model behavior as a function of the underlying structural connectome – whether it is individualized, template-based, uniform, random or distance based. DCM methods have not reported first order regional power spectra as we do here, nor have they explored how the structural connectome influences model spectral distributions.

Second, our model is more parsimonious compared to most of these above-mentioned models which have many more degrees of freedom because they often allow for regions and their interactions to have different parameters. Our model parameterization, with only a few global parameters, lends itself to efficient computations over fine-scale whole-brain parcellations, whereas most DCMs (with the exception of recent spectral and regression DCMS[270, 269, 268]) are suited for examining smaller networks but involve large effective connectivity matrices and region-specific parameters. Furthermore, parameters of our model remain grounded and interpretable in terms of the underlying biophysics, i.e. time constants and conductivities. In contrast, spectral and regression DCM models of cross-spectra have parameters that are abstract and do not have immediate biophysical interpretation.

The third major difference is in the emphasis placed on Variational Bayesian inference in DCM. Since our focus was on exploring model behavior over a small number of global parameters and a set of structural connectomes (whether anatomic or random) of identical sparsity and complexity, it was sufficient to use a *maximum a posteriori* (MAP) estimation procedure for Bayesian inference of our global model parameters with flat non-informative priors with pre-determined ranges based on biophysics. Like most DCM efforts our model can be easily be extended to Variational Empirical Bayesian inference for parameter estimation,

for instance to compute a full posterior of the structural connectivity matrix. In such a formulation, we can assume that the observed structural connectome will serve as the prior mean of the connectivity matrix. We reserve such extensions to our future work with this spectral graph model.

5.4.6 Other limitations and extensions

The model currently examines resting-state activity, but future extensions will include prediction of functional connectivity, task-induced modulations of neural oscillations and causal modeling of external stimuli, e.g. transcranial magnetic and direct current stimulation. The current implementation does not incorporate complex local dynamics, but future work will explore using non-white internal noise and chaotic dynamics for local assemblies. This may allow us to examine higher gamma frequencies. Although our model incorporates latency information derived from path distances, we plan to explore path-specific propagation velocities derived from white matter microstructural metrics such as axon diameter distributions and myelin thickness. Future work will also examine the specific topographic features of the structural connectome that may best describe canonical neural activity spectra. Finally, we plan to examine the ability of the model to predict time-varying structure-function relationships.

5.4.7 Potential applications

Mathematical encapsulation of the structure-function relationship can potentiate novel approaches for mapping and monitoring brain diseases such as

autism, schizophrenia, epilepsy and dementia, since early functional changes are more readily and sensitively measured using fMRI and MEG, compared to structural changes. Because of the complementary sensitivity, temporal and spatial resolutions of diffusion MRI, MEG, EEG and fMRI, combining these modalities may be able to reveal fine spatiotemporal structures of neuronal activity that would otherwise remain undetected if using only one modality. Current efforts at fusing multimodalities are interpretive, phenomenological or statistical, with limited cognizance of underlying neuronal processes. Thus, the ability of the presented model to quantitatively and parsimoniously capture the structure-function relationship may be key to achieving true multi-modality integration.

APPENDIX A
APPENDIX: SUPPLEMENTARY FIGURES

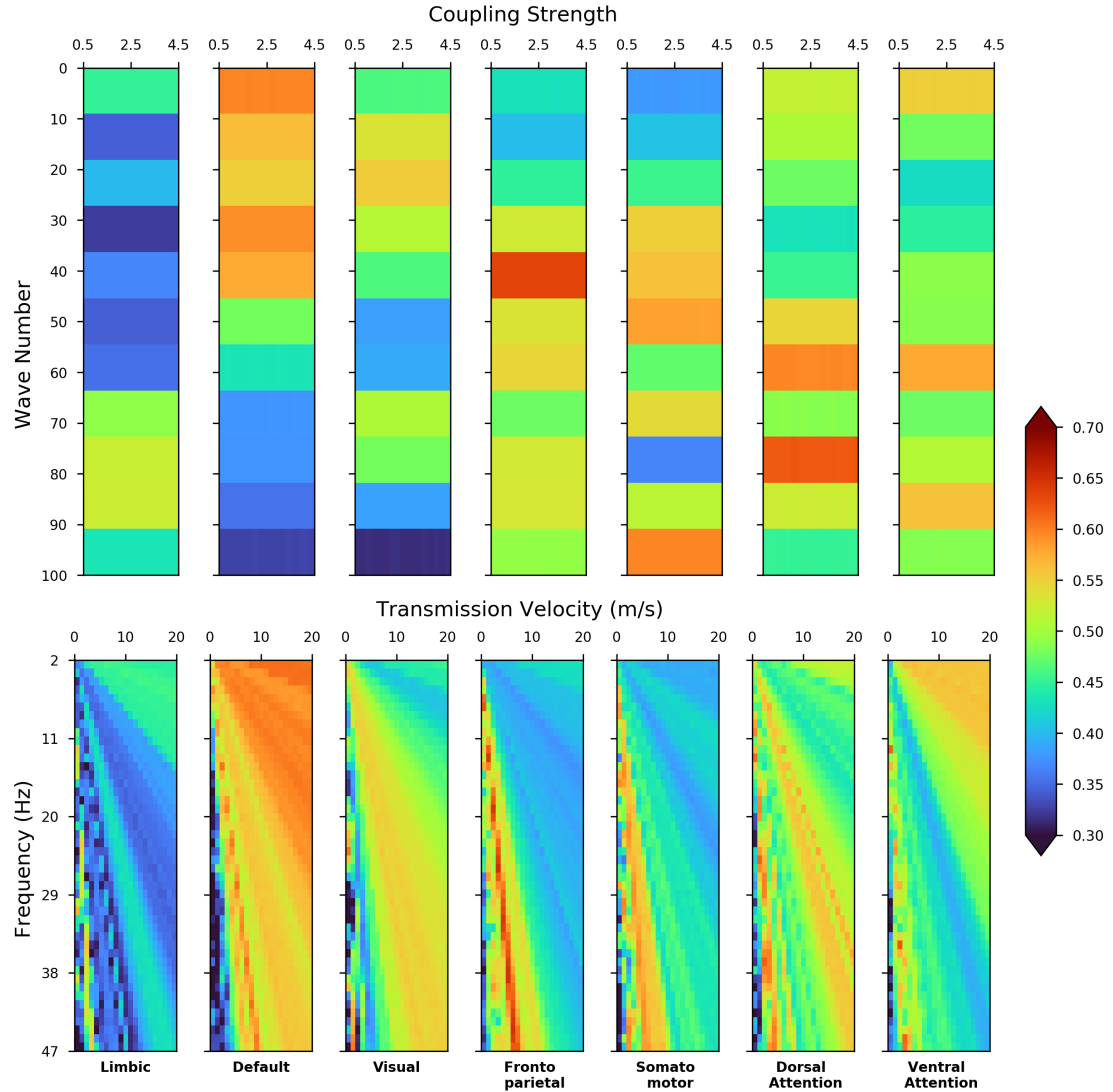


Figure A.1: Parameter dependency of structural complex Laplace eigenmodes.

Heat-maps displaying best achievable spatial correlation values (Spearman's) by a single eigenmode across all parameter values for each canonical functional network. Shifts in coupling strength (top) does not cause a change in peak spatial correlation. The bottom row shows the transmission speed and oscillating frequency of signals in the network dictates the cortical activation patterns in the brain, shifts in wave number parameters while holding global coupling constant changes the best achievable spatial similarity to each canonical network.

	$C_{HCP}^* \text{ vs. } C_{random}^*$ (D_{random})	$C_{HCP} \text{ vs. } C_{random}^*$ (D_{random})	$C_{HCP}^* \text{ vs. } C_{HCP}^*$ (D_{random})	$C_{HCP} \text{ vs. } C_{HCP}^*$ (D_{random})
Limbic	1.504e-06	1.466e-06	1.355e-03	1.328e-03
Default	2.015e-07	5.512e-05	1.119e-01	4.804e-01
Visual	1.122e-13	4.967e-03	9.580e-06	3.928e-01
Frontoparietal	2.263e-06	4.993e-01	2.856e-03	1.789e-02
Somatomotor	5.882e-06	1.459e-01	3.088e-01	9.173e-23
Dorsal Attention	2.412e-04	4.522e-01	6.038e-06	4.101e-01
Ventral Attention	2.700e-02	2.705e-01	6.175e-02	6.202e-16

Table A.1: Statistical comparison between HCP connectome and random connectome with Pearson's correlation.

P-values table from random connectome comparisons of leading eigenmodes. Z-score distributions of spatial correlation (Pearson's) were created from 1000 sets of complex Laplace eigenmodes of $C_{random}^*(D_{random})$ and $C_{HCP}^*(D_{random})$ random connectomes. For all canonical networks' similarity comparisons, a 95% confidence interval of the Z-scores distributions were obtained and used to compute the *P*-values shown in the tables.

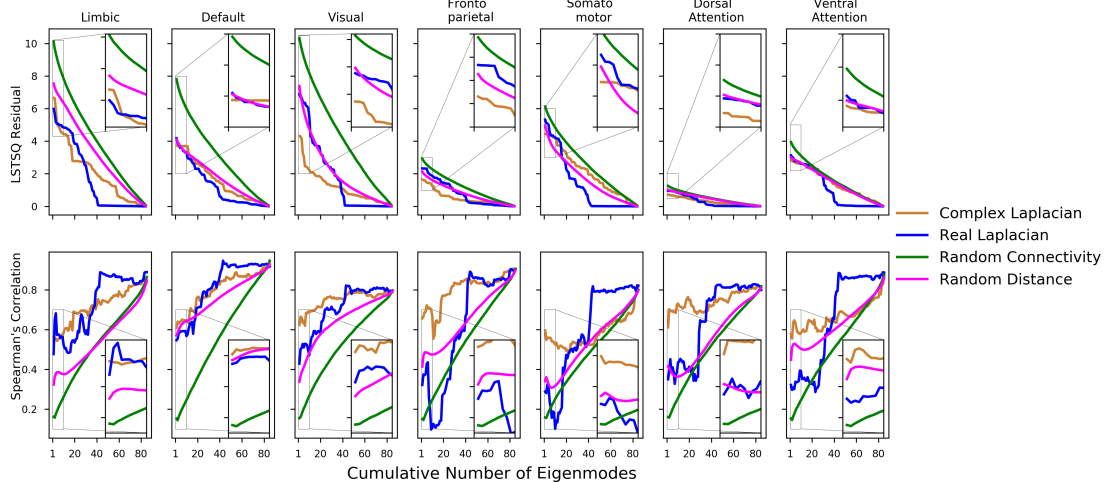


Figure A.2: Spatial similarity quantified by Spearman's correlation

Spatial pattern similarity of HCP template connnectome complex Laplacian structural eigenmodes to canonical functional networks quantified with Spearman's correlation. The same analysis performed in Figure 2 but Pearson's correlation was replaced with Spearman's correlation for discrete samples for the bottom row, and the top row shows linear least square residuals. Despite the more inconsistent increasing trend in spatial pattern similarity due to ranking of discrete samples, the complex Laplacian eigenmodes are able to outperform the real-valued Laplacian eigenmodes (blue), complex eigenmodes from random structural connectome with random distance matrix (green), as well as complex eigenmodes from HCP template connectome with random distance matrix.

	$C_{HCP}^* \text{ vs. } C_{random}^*$ (D_{random})	$C_{HCP} \text{ vs. } C_{random}^*$ (D_{random})	$C_{HCP}^* \text{ vs. } C_{HCP}^*$ (D_{random})	$C_{HCP} \text{ vs. } C_{HCP}^*$ (D_{random})
Limbic	4.423e-06	2.448e-04	4.593e-07	8.516e-04
Default	1.404e-07	4.469e-06	2.872e-01	3.573e-01
Visual	7.601e-08	1.091e-03	1.312e-05	9.155e-02
Frontoparietal	3.181e-09	2.455e-02	4.866e-05	6.873e-02
Somatomotor	4.160e-07	7.129e-02	5.856e-07	1.616e-01
Dorsal Attention	5.086e-07	1.955e-02	7.333e-03	2.072e-01
Ventral Attention	1.312e-06	3.077e-02	4.396e-02	4.676e-02

Table A.2: Statistical comparison between HCP connectome and random connectome with Spearman's correlation.

P-values table from random connectome comparisons of leading eigenmodes. This table is produced the same way as Table S1, but the Z-score distributions were computed from Spearman's correlation

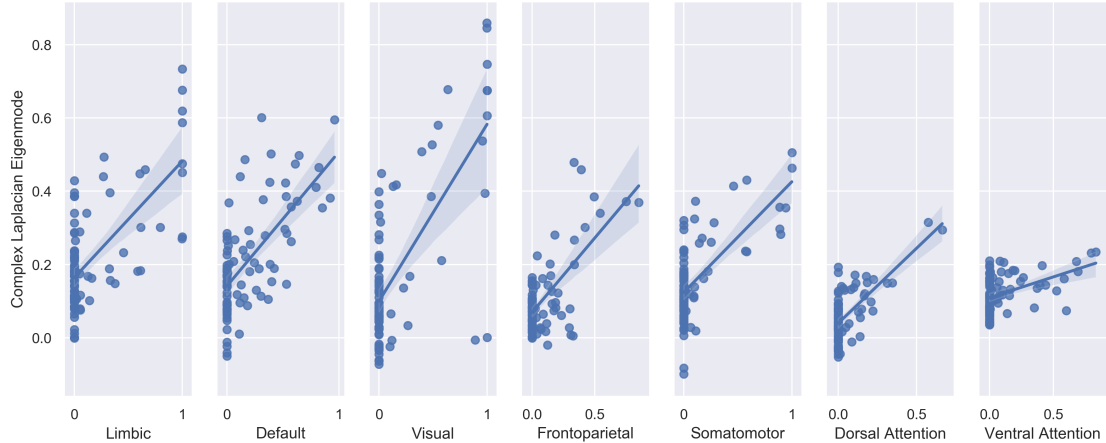


Figure A.3: Dice coefficient optimized spatial correlation.

Dice coefficient optimized model parameters display similar spatial matching as spatial correlation optimized model parameters. Both the canonical functional networks and complex Laplacian eigenmodes were binarized with a threshold value that resulted in the closest number of non-zero elements in both spatial maps, then the optimized model parameters were found by minimizing the dice coefficient between binarized versions of the canonical functional networks and the complex Laplacian eigenmodes. Scatter plots shows the linear combination of the top 10 matching eigenmodes for each canonical functional network and their linear regression fitted line with 95% confidence intervals.

BIBLIOGRAPHY

- [1] Catherine Y. Wan and Gottfried Schlaug. Music making as a tool for promoting brain plasticity across the life span. *The Neuroscientist : a review journal bringing neurobiology, neurology and psychiatry*, 16(5):566–577, October 2010.
- [2] Timothy L. Warren, Evren C. Tumer, Jonathan D. Charlesworth, and Michael S. Brainard. Mechanisms and time course of vocal learning and consolidation in the adult songbird. *Journal of Neurophysiology*, 106(4):1806–1821, October 2011.
- [3] Andreas Nieder. Counting on neurons: the neurobiology of numerical competence. *Nature Reviews Neuroscience*, 6(3):177–190, March 2005.
- [4] Ilka Diester and Andreas Nieder. Semantic associations between signs and numerical categories in the prefrontal cortex. *PLOS Biology*, 5(11):e294, October 2007.
- [5] A. L. Hodgkin and A. F. Huxley. A quantitative description of membrane current and its application to conduction and excitation in nerve. *The Journal of Physiology*, 117:500–544, 1952.
- [6] Hermann Haken. An Introduction. In Hermann Haken, editor, *Synergetics: Introduction and Advanced Topics*, pages 1–387. Springer, Berlin, Heidelberg, 2004.
- [7] H. E. Fiedler. Coherent Structures. In *Advances in Turbulence*, pages 320–336, Berlin, Heidelberg, 1987. Springer.
- [8] V. K. Jirsa and H. Haken. Field theory of electromagnetic brain activity. *Phys. Rev. Lett.*, 77:960–963, Jul 1996.
- [9] Walter J. Freeman. *Mass action in the nervous system: examination of the neurophysiological basis of adaptive behavior through the EEG*. Academic Press, New York, 1975.
- [10] Michael Breakspear, JA Roberts, John R Terry, Serafim Rodrigues, N Mabant, and PA Robinson. A unifying explanation of primary generalized seizures through nonlinear brain modeling and bifurcation analysis. *Cerebral Cortex*, 16(9):1296–1313, 2006.

- [11] Ingo Bojak, Zhivko V Stoyanov, and David TJ Liley. Emergence of spatially heterogeneous burst suppression in a neural field model of electrocortical activity. *Frontiers in systems neuroscience*, 9:18, 2015.
- [12] AJK Phillips and Peter A Robinson. A quantitative model of sleep-wake dynamics based on the physiology of the brainstem ascending arousal system. *Journal of Biological Rhythms*, 22(2):167–179, 2007.
- [13] Ingo Bojak and DTJ Liley. Modeling the effects of anesthesia on the electroencephalogram. *Physical Review E*, 71(4):041902, 2005.
- [14] Christopher J Honey, Rolf Kötter, Michael Breakspear, and Olaf Sporns. Network structure of cerebral cortex shapes functional connectivity on multiple time scales. *Proceedings of the National Academy of Sciences*, 104(24):10240–10245, 2007.
- [15] G. Deco, V. Jirsa, A. R. McIntosh, O. Sporns, and R. Kotter. Key role of coupling, delay, and noise in resting brain fluctuations. *Proceedings of the National Academy of Sciences*, 106(25):10302–10307, 2009.
- [16] H R Wilson and J D Cowan. Excitatory and inhibitory interactions in localized populations of model neurons. *Biophysical journal*, 12(1):1–24, 1972.
- [17] Henri Poincaré. *Les méthodes nouvelles de la mécanique céleste*, volume 3. Gauthier-Villars, 1899.
- [18] A Aldo Faisal, Luc PJ Selen, and Daniel M Wolpert. Noise in the nervous system. *Nature reviews neuroscience*, 9(4):292–303, 2008.
- [19] Bratislav Mišic, Travis Mills, Margot J Taylor, and Anthony R McIntosh. Brain noise is task dependent and region specific. *Journal of Neurophysiology*, 104(5):2667–2676, 2010.
- [20] Paula Sanz-Leon, Stuart A. Knock, Andreas Spiegler, and Viktor K. Jirsa. Mathematical framework for large-scale brain network modeling in the virtual brain. *NeuroImage*, 111:385–430, May 2015.
- [21] Quentin J. M. Huys, Tiago V. Maia, and Michael J. Frank. Computational psychiatry as a bridge from neuroscience to clinical applications. *Nature Neuroscience*, 19(3):404–413, March 2016.

- [22] Rafal Bogacz, Eric Brown, Jeff Moehlis, Philip Holmes, and Jonathan D. Cohen. The physics of optimal decision making: a formal analysis of models of performance in two-alternative forced-choice tasks. *Psychological Review*, 113(4):700–765, October 2006.
- [23] Henry Hamburger. Donald R. J. Laming. Information, theory of choice-reaction times. New York: Academic Press, 1968. *Behavioral Science*, 14(4):330–333, 1969.
- [24] Roger Ratcliff and Gail McKoon. The Diffusion Decision Model: Theory and Data for Two-Choice Decision Tasks. *Neural computation*, 20(4):873–922, April 2008.
- [25] Roger Ratcliff, Trisha Van Zandt, and Gail McKoon. Connectionist and diffusion models of reaction time. *Psychological Review*, 106(2):261–300, 1999.
- [26] Philip L. Smith. From Poisson shot noise to the integrated Ornstein-Uhlenbeck process: Neurally principled models of information accumulation in decision-making and response time. *JOURNAL OF MATHEMATICAL PSYCHOLOGY*, 54(2), 2010.
- [27] Jiaxiang Zhang and Rafal Bogacz. Optimal Decision Making on the Basis of Evidence Represented in Spike Trains. *Neural Computation*, 22(5):1113–1148, May 2010.
- [28] Bela Bollobas. *Graph Theory: An Introductory Course*. Graduate Texts in Mathematics. Springer-Verlag, New York, 1979.
- [29] Yong He, Zhang J. Chen, and Alan C. Evans. Small-world anatomical networks in the human brain revealed by cortical thickness from MRI. *Cerebral Cortex (New York, N.Y.: 1991)*, 17(10):2407–2419, October 2007.
- [30] Lav R. Varshney, Beth L. Chen, Eric Paniagua, David H. Hall, and Dmitri B. Chklovskii. Structural Properties of the *Caenorhabditis elegans* Neuronal Network. *PLOS Computational Biology*, 7(2):e1001066, February 2011.
- [31] Danielle S. Bassett, Jesse A. Brown, Vibhas Deshpande, Jean M. Carlson, and Scott T. Grafton. Conserved and variable architecture of human white matter connectivity. *NeuroImage*, 54(2):1262–1279, January 2011.

- [32] Karl J. Friston. Functional and effective connectivity: a review. *Brain Connectivity*, 1(1):13–36, 2011.
- [33] Olaf Sporns and Richard F. Betzel. Modular Brain Networks. *Annual Review of Psychology*, 67:613–640, 2016.
- [34] Ann E. Sizemore, Chad Giusti, Ari Kahn, Jean M. Vettel, Richard F. Betzel, and Danielle S. Bassett. Cliques and cavities in the human connectome. *Journal of Computational Neuroscience*, 44(1):115–145, February 2018.
- [35] Michael W. Reimann, Max Nolte, Martina Scolamiero, Katharine Turner, Rodrigo Perin, Giuseppe Chindemi, Paweł Dłotko, Ran Levi, Kathryn Hess, and Henry Markram. Cliques of Neurons Bound into Cavities Provide a Missing Link between Structure and Function. *Frontiers in Computational Neuroscience*, 11:48, 2017.
- [36] Danielle Smith Bassett and Ed Bullmore. Small-world brain networks. *The Neuroscientist*, pages 512–523, 2006.
- [37] Christoph Börgers and Nancy Kopell. Synchronization in networks of excitatory and inhibitory neurons with sparse, random connectivity. *Neural Computation*, 15(3):509–538, March 2003.
- [38] Elad Ganmor, Ronen Segev, and Elad Schneidman. Sparse low-order interaction network underlies a highly correlated and learnable neural population code. *Proceedings of the National Academy of Sciences of the United States of America*, 108(23):9679–9684, June 2011.
- [39] Andrea Avena-Koenigsberger, Bratislav Misic, and Olaf Sporns. Communication dynamics in complex brain networks. *Nature Reviews. Neuroscience*, 19(1):17–33, December 2017.
- [40] L. F. Abbott. Theoretical Neuroscience Rising. *Neuron*, 60(3):489–495, November 2008.
- [41] Jinjie Zhu, Zhen Chen, and Xian-Bin Liu. Effects of distance-dependent delay on small-world neuronal networks. *Physical Review E*, 93, April 2016.
- [42] J. A. Acebrón, A. R. Bulsara, and W.-J. Rappel. Noisy FitzHugh-Nagumo model: From single elements to globally coupled networks. *Physical Review E*, 69(2):026202, February 2004. Publisher: American Physical Society.

- [43] Michael Breakspear, Stewart Heitmann, and Andreas Daffertshofer. Generative Models of Cortical Oscillations: Neurobiological Implications of the Kuramoto Model. *Frontiers in Human Neuroscience*, 4:190, 2010.
- [44] Michael Breakspear. Dynamic models of large-scale brain activity. *Nature Neuroscience*, 20(3):340–352, March 2017.
- [45] Wulfram Gerstner, Henning Sprekeler, and Gustavo Deco. Theory and Simulation in Neuroscience. *Science*, 338(6103):60–65, October 2012.
- [46] F. Babiloni, F. Cincotti, C. Babiloni, F. Carducci, D. Mattia, L. Astolfi, A. Basilisco, P. M. Rossini, L. Ding, Y. Ni, J. Cheng, K. Christine, J. Sweeney, and B. He. Estimation of the cortical functional connectivity with the multimodal integration of high-resolution EEG and fMRI data by directed transfer function. *NeuroImage*, 24(1):118–131, January 2005.
- [47] Steven L. Bressler and Anil K. Seth. Wiener-Granger causality: a well established methodology. *NeuroImage*, 58(2):323–329, September 2011.
- [48] André M. Bastos and Jan-Mathijs Schoffelen. A Tutorial Review of Functional Connectivity Analysis Methods and Their Interpretational Pitfalls. *Frontiers in Systems Neuroscience*, 9:175, 2016.
- [49] Felice T. Sun, Lee M. Miller, and Mark D’Esposito. Measuring interregional functional connectivity using coherence and partial coherence analyses of fMRI data. *NeuroImage*, 21(2):647–658, February 2004.
- [50] Jean Daunizeau, Stefan J. Kiebel, and Karl J. Friston. Dynamic causal modelling of distributed electromagnetic responses. *NeuroImage*, 47(2):590–601, 2009.
- [51] Marcus E. Raichle, Ann Mary MacLeod, Abraham Z. Snyder, William J. Powers, Debra A. Gusnard, and Gordon L. Shulman. A default mode of brain function. *Proceedings of the National Academy of Sciences*, 98(2):676–682, January 2001.
- [52] Stephen M. Smith, Peter T. Fox, Karla L. Miller, David C. Glahn, P. Mickle Fox, Clare E. Mackay, Nicola Filippini, Kate E. Watkins, Roberto Toro, Angela R. Laird, and Christian F. Beckmann. Correspondence of the brain’s functional architecture during activation and rest. *Proceedings of the National Academy of Sciences*, 106(31):13040–13045, August 2009.

- [53] B T Thomas Yeo, Fenna M Krienen, Jorge Sepulcre, Mert R Sabuncu, Danial Lashkari, Marisa Hollinshead, Joshua L Roffman, Jordan W Smoller, Lilla Zöllei, Jonathan R Polimeni, Bruce Fischl, Hesheng Liu, and Randy L Buckner. The organization of the human cerebral cortex estimated by intrinsic functional connectivity. *Journal of neurophysiology*, 106:1125–65, 2011.
- [54] Markus Siegel, Tobias H. Donner, and Andreas K. Engel. Spectral fingerprints of large-scale neuronal interactions. *Nature Reviews. Neuroscience*, 13(2):121–134, January 2012.
- [55] Ian Nauhaus, Laura Busse, Matteo Carandini, and Dario L. Ringach. Stimulus contrast modulates functional connectivity in visual cortex. *Nature Neuroscience*, 12(1):70–76, January 2009.
- [56] Danielle S. Bassett, Muzhi Yang, Nicholas F. Wymbs, and Scott T. Grafton. Learning-induced autonomy of sensorimotor systems. *Nature Neuroscience*, 18(5):744–751, May 2015.
- [57] Tao Wu, Liang Wang, Yi Chen, Cheng Zhao, Kuncheng Li, and Piu Chan. Changes of functional connectivity of the motor network in the resting state in Parkinson’s disease. *Neuroscience Letters*, 460(1):6–10, August 2009.
- [58] Christopher P. Pawela, Bharat B. Biswal, Anthony G. Hudetz, Rupeng Li, Seth R. Jones, Younghoon R. Cho, Hani S. Matloub, and James S. Hyde. Interhemispheric neuroplasticity following limb deafferentation detected by resting-state functional connectivity magnetic resonance imaging (fcMRI) and functional magnetic resonance imaging (fMRI). *NeuroImage*, 49(3):2467–2478, February 2010.
- [59] Katherine H. Karlsgodt, Theo G. M. van Erp, Russell A. Poldrack, Carrie E. Bearden, Keith H. Nuechterlein, and Tyrone D. Cannon. Diffusion tensor imaging of the superior longitudinal fasciculus and working memory in recent-onset schizophrenia. *Biological Psychiatry*, 63(5):512–518, March 2008.
- [60] Carl D. Hacker, Joel S. Perlmutter, Susan R. Criswell, Beau M. Ances, and Abraham Z. Snyder. Resting state functional connectivity of the striatum in Parkinson’s disease. *Brain: A Journal of Neurology*, 135(Pt 12):3699–3711, December 2012.
- [61] Ulrike Lueken, Benjamin Straube, Carsten Konrad, Hans-Ulrich Wittchen, Andreas Ströhle, André Wittmann, Bettina Pfleiderer, Christina Uhlmann,

- Volker Arolt, Andreas Jansen, and Tilo Kircher. Neural substrates of treatment response to cognitive-behavioral therapy in panic disorder with agoraphobia. *The American Journal of Psychiatry*, 170(11):1345–1355, November 2013.
- [62] Glyn P. Hallam, Hannah E. Thompson, Mark Hymers, Rebecca E. Millman, Jennifer M. Rodd, Matthew A. Lambon Ralph, Jonathan Smallwood, and Elizabeth Jefferies. Task-based and resting-state fMRI reveal compensatory network changes following damage to left inferior frontal gyrus. *Cortex*, 99:150–165, February 2018.
- [63] Judea Pearl. Causality: Models, reasoning, and inference, second edition. *Causality*, 29, January 2000.
- [64] Simon Musall, Matthew T. Kaufman, Steven Gluf, and Anne K. Churchland. Movement-related activity dominates cortex during sensory-guided decision making. Technical report, April 2018.
- [65] Carsen Stringer, Marius Pachitariu, Nicholas Steinmetz, Charu Bai Reddy, Matteo Carandini, and Kenneth D. Harris. Spontaneous behaviors drive multidimensional, brainwide activity. *Science*, 364(6437):eaav7893, April 2019.
- [66] E. H. Simpson. The Interpretation of Interaction in Contingency Tables. *Journal of the Royal Statistical Society. Series B (Methodological)*, 13(2):238–241, 1951.
- [67] Reece Roberts, Sylvia Hach, Lynette Tippett, and Donna Addis. The Simpson’s paradox and fMRI: Similarities and differences between functional connectivity measures derived from within-subject and across-subject correlations. *NeuroImage*, 135, April 2016.
- [68] Mehraveh Salehi, Abigail S. Greene, Amin Karbasi, Xilin Shen, Dustin Scheinost, and R. Todd Constable. There is no single functional atlas even for a single individual: Functional parcel definitions change with task. *NeuroImage*, 208:116366, March 2020.
- [69] Angela M Bruno, William N Frost, and Mark D Humphries. A spiral attractor network drives rhythmic locomotion. *eLife*, 6:e27342, August 2017.
- [70] Evan M. Gordon, Timothy O. Laumann, Adrian W. Gilmore, Dillan J.

- Newbold, Deanna J. Greene, Jeffrey J. Berg, Mario Ortega, Catherine Hoyt-Drazen, Caterina Gratton, Haoxin Sun, Jacqueline M. Hampton, Rebecca S. Coalson, Annie L. Nguyen, Kathleen B. McDermott, Joshua S. Shimony, Abraham Z. Snyder, Bradley L. Schlaggar, Steven E. Petersen, Steven M. Nelson, and Nico U. F. Dosenbach. Precision Functional Mapping of Individual Human Brains. *Neuron*, 95(4):791–807.e7, August 2017.
- [71] Ely M. Marceau, Denise Meuldijk, Michelle L. Townsend, Nadia Solowij, and Brin F. S. Grenyer. Biomarker correlates of psychotherapy outcomes in borderline personality disorder: A systematic review. *Neuroscience and Biobehavioral Reviews*, 94:166–178, November 2018.
- [72] Adela Desowska and Duncan L. Turner. Dynamics of brain connectivity after stroke. *Reviews in the Neurosciences*, 30(6):605–623, July 2019.
- [73] Lian Beijers, Klaas J. Wardenaar, Hanna M. van Loo, and Robert A. Schoevers. Data-driven biological subtypes of depression: systematic review of biological approaches to depression subtyping. *Molecular Psychiatry*, 24(6):888–900, June 2019.
- [74] David Marc Anton Mehler and Konrad Paul Kording. The lure of misleading causal statements in functional connectivity research. *arXiv:1812.03363 [q-bio]*, October 2020.
- [75] Pedro J Gonçalves, Jan-Matthis Lueckmann, Michael Deistler, Marcel Nonnenmacher, Kaan Öcal, Giacomo Bassetto, Chaitanya Chintaluri, William F Podlaski, Sara A Haddad, Tim P Vogels, David S Greenberg, and Jakob H Macke. Training deep neural density estimators to identify mechanistic models of neural dynamics. *eLife*, 9:e56261, September 2020.
- [76] Usama Pervaiz, Diego Vidaurre, Mark W. Woolrich, and Stephen M. Smith. Optimising network modelling methods for fMRI. *NeuroImage*, page 116604, February 2020.
- [77] Harshit Parmar, Brian Nutter, Rodney Long, Sameer Antani, and Sunanda Mitra. Spatiotemporal feature extraction and classification of Alzheimer’s disease using deep learning 3D-CNN for fMRI data. *Journal of Medical Imaging*, 7(5):056001, October 2020.
- [78] E. O. Stejskal and J. E. Tanner. Spin diffusion measurements: Spin echoes in the presence of a time-dependent field gradient. *The Journal of Chemical Physics*, 42(1):288–292, January 1965.

- [79] D. Le Bihan, E. Breton, D. Lallemand, P. Grenier, E. Cabanis, and M. Laval-Jeantet. MR imaging of intravoxel incoherent motions: application to diffusion and perfusion in neurologic disorders. *Radiology*, 161(2):401–407, November 1986.
- [80] P. J. Basser, J. Mattiello, and D. LeBihan. Estimation of the effective self-diffusion tensor from the NMR spin echo. *Journal of Magnetic Resonance, Series B*, 103(3):247–254, March 1994.
- [81] P.J. Basser, J. Mattiello, and D. LeBihan. MR diffusion tensor spectroscopy and imaging. *Biophysical Journal*, 66(1):259–267, January 1994.
- [82] Carlo Pierpaoli and Peter J. Basser. Toward a quantitative assessment of diffusion anisotropy. *Magnetic Resonance in Medicine*, 36(6):893–906, 1996.
- [83] A. M. Uluğ and P. C. van Zijl. Orientation-independent diffusion imaging without tensor diagonalization: anisotropy definitions based on physical attributes of the diffusion ellipsoid. *Journal of magnetic resonance imaging: JMRI*, 9(6):804–813, June 1999.
- [84] C. Thomsen, O. Henriksen, and P. Ring. In vivo measurement of water self diffusion in the human brain by magnetic resonance imaging. *Acta Radiologica (Stockholm, Sweden: 1987)*, 28(3):353–361, June 1987.
- [85] T. L. Chenevert, J. A. Brunberg, and J. G. Pipe. Anisotropic diffusion in human white matter: demonstration with MR techniques in vivo. *Radiology*, 177(2):401–405, November 1990.
- [86] D. Chien, R. B. Buxton, K. K. Kwong, T. J. Brady, and B. R. Rosen. MR diffusion imaging of the human brain. *Journal of Computer Assisted Tomography*, 14(4):514–520, August 1990.
- [87] M. E. Moseley, Y. Cohen, J. Kucharczyk, J. Mintorovitch, H. S. Asgari, M. F. Wendland, J. Tsuruda, and D. Norman. Diffusion-weighted MR imaging of anisotropic water diffusion in cat central nervous system. *Radiology*, 176(2):439–445, August 1990.
- [88] M. D. King, N. van Bruggen, R. G. Ahier, J. E. Cremer, J. V. Hajnal, S. R. Williams, and M. Doran. Diffusion-weighted imaging of kainic acid lesions in the rat brain. *Magnetic Resonance in Medicine*, 20(1):158–164, July 1991.
- [89] F. A. Howe, A. G. Filler, B. A. Bell, and J. R. Griffiths. Magnetic resonance

- neurography. *Magnetic Resonance in Medicine*, 28(2):328–338, December 1992.
- [90] J. V. Hajnal, M. Doran, A. S. Hall, A. G. Collins, A. Oatridge, J. M. Pennock, I. R. Young, and G. M. Bydder. MR imaging of anisotropically restricted diffusion of water in the nervous system: technical, anatomic, and pathologic considerations. *Journal of Computer Assisted Tomography*, 15(1):1–18, February 1991.
- [91] M. E. Moseley, J. Kucharczyk, H. S. Asgari, and D. Norman. Anisotropy in diffusion-weighted MRI. *Magnetic Resonance in Medicine*, 19(2):321–326, June 1991.
- [92] H. Sakuma, Y. Nomura, K. Takeda, T. Tagami, T. Nakagawa, Y. Tamagawa, Y. Ishii, and T. Tsukamoto. Adult and neonatal human brain: diffusional anisotropy and myelination with diffusion-weighted MR imaging. *Radiology*, 180(1):229–233, July 1991.
- [93] M. A. Rutherford, F. M. Cowan, A. Y. Manzur, L. M. Dubowitz, J. M. Pennock, J. V. Hajnal, I. R. Young, and G. M. Bydder. MR imaging of anisotropically restricted diffusion in the brain of neonates and infants. *Journal of Computer Assisted Tomography*, 15(2):188–198, April 1991.
- [94] P. Douek, R. Turner, J. Pekar, N. Patronas, and D. Le Bihan. MR color mapping of myelin fiber orientation. *Journal of Computer Assisted Tomography*, 15(6):923–929, December 1991.
- [95] S. Warach, J. Gaa, B. Siewert, P. Wielopolski, and R. R. Edelman. Acute human stroke studied by whole brain echo planar diffusion-weighted magnetic resonance imaging. *Annals of Neurology*, 37(2):231–241, February 1995.
- [96] Valerij G. Kiselev. Fundamentals of diffusion MRI physics. *NMR in biomedicine*, 30(3), March 2017.
- [97] Dow-Mu Koh and David J. Collins. Diffusion-weighted MRI in the body: applications and challenges in oncology. *AJR. American journal of roentgenology*, 188(6):1622–1635, June 2007.
- [98] Santiago Aja-Fernandez, Carlos Alberola-Lopez, and Carl-Fredrik Westin. Noise and signal estimation in magnitude MRI and rician distributed images: A LMMSE approach. *IEEE Transactions on Image Processing*, 17(8):1383–1398, August 2008.

- [99] Jelle Veraart, Wim Van Hecke, and Jan Sijbers. Constrained maximum likelihood estimation of the diffusion kurtosis tensor using a rician noise model. *Magnetic Resonance in Medicine*, 66(3):678–686, September 2011.
- [100] Denis Le Bihan, Cyril Poupon, Alexis Amadon, and Franck Lethimonnier. Artifacts and pitfalls in diffusion MRI. *Journal of magnetic resonance imaging: JMRI*, 24(3):478–488, September 2006.
- [101] Jesper L. R. Andersson and Stefan Skare. A model-based method for retrospective correction of geometric distortions in diffusion-weighted EPI. *NeuroImage*, 16(1):177–199, May 2002.
- [102] Jesper L. R. Andersson and Stamatis N. Sotropoulos. An integrated approach to correction for off-resonance effects and subject movement in diffusion MR imaging. *NeuroImage*, 125:1063–1078, January 2016.
- [103] Jelle Veraart, Els Fieremans, Ileana O. Jelescu, Florian Knoll, and Dmitry S. Novikov. Gibbs ringing in diffusion MRI. *Magnetic Resonance in Medicine*, 76(1):301–314, 2016.
- [104] GJM Parker, GJ Barker, and CA Wheeler-Kingshot. Gibbs ringing and negative ADC values. In *Proceedings of the ISMRM ninth meeting*, 2001.
- [105] Jacques-Donald Tournier, Susumu Mori, and Alexander Leemans. Diffusion tensor imaging and beyond. *Magnetic Resonance in Medicine*, 65(6):1532–1556, 2011.
- [106] Elias Kellner, Bibek Dhital, Valerij G. Kiselev, and Marco Reisert. Gibbs-ringing artifact removal based on local subvoxel-shifts. *Magnetic Resonance in Medicine*, 76(5):1574–1581, 2016.
- [107] Daniele Perrone, Jan Aelterman, Aleksandra Pižurica, Ben Jeurissen, Wilfried Philips, and Alexander Leemans. The effect of gibbs ringing artifacts on measures derived from diffusion MRI. *NeuroImage*, 120:441–455, October 2015.
- [108] Matt A. Bernstein, John Huston, and Heidi A. Ward. Imaging artifacts at 3.0T. *Journal of magnetic resonance imaging: JMRI*, 24(4):735–746, October 2006.
- [109] Boubakeur Belaroussi, Julien Milles, Sabin Carme, Yue Min Zhu, and Hugues Benoit-Cattin. Intensity non-uniformity correction in MRI: existing

- methods and their validation. *Medical Image Analysis*, 10(2):234–246, April 2006.
- [110] Ali Tabesh, Jens H. Jensen, Babak A. Ardekani, and Joseph A. Helpern. Estimation of tensors and tensor-derived measures in diffusional kurtosis imaging. *Magnetic Resonance in Medicine*, 65(3):823–836, 2011.
- [111] Zaixu Cui, Suyu Zhong, Pengfei Xu, Gaolang Gong, and Yong He. PANDA: a pipeline toolbox for analyzing brain diffusion images. *Frontiers in Human Neuroscience*, 7:42, 2013.
- [112] Benjamin Ades-Aron, Jelle Veraart, Peter Kochunov, Stephen McGuire, Paul Sherman, Elias Kellner, Dmitry S. Novikov, and Els Fieremans. Evaluation of the accuracy and precision of the diffusion parameter estimation with gibbs and noise removal pipeline. *NeuroImage*, 183:532–543, December 2018.
- [113] J.-Donald Tournier, Robert Smith, David Raffelt, Rami Tabbara, Thijs Dhollander, Maximilian Pietsch, Daan Christiaens, Ben Jeurissen, Chun-Hung Yeh, and Alan Connelly. MRtrix3: A fast, flexible and open software framework for medical image processing and visualisation. *NeuroImage*, 202:116137, November 2019.
- [114] Bruce Fischl. Freesurfer. *NeuroImage*, 62:774–781, 2012.
- [115] William D. Penny, Karl J. Friston, John Ashburner, Stefan J Kiebel, and Thomas Nichols. *Statistical Parametric Mapping: The Analysis of Functional Brain Images*. Elsevier/Academic Press, 2006.
- [116] Mark Jenkinson, Christian F. Beckmann, Timothy E.J. Behrens, Mark W. Woolrich, and Stephen M. Smith. Fsl. *NeuroImage*, 62(2):782–790, August 2012.
- [117] Luca Vizioli, Steen Moeller, Logan Dowdle, Mehmet Akçakaya, Federico De Martino, Essa Yacoub, and Kamil Ugurbil. Lowering the thermal noise barrier in functional brain mapping with magnetic resonance imaging. *Nature Communications*, 12(1):5181, August 2021.
- [118] D. I Hoult and R. E Richards. The signal-to-noise ratio of the nuclear magnetic resonance experiment. *Journal of Magnetic Resonance (1969)*, 24(1):71–85, October 1976.

- [119] W. A. Edelstein, G. H. Glover, C. J. Hardy, and R. W. Redington. The intrinsic signal-to-noise ratio in NMR imaging. *Magnetic Resonance in Medicine*, 3(4):604–618, August 1986.
- [120] K. P. Pruessmann, M. Weiger, M. B. Scheidegger, and P. Boesiger. SENSE: sensitivity encoding for fast MRI. *Magnetic Resonance in Medicine*, 42(5):952–962, November 1999.
- [121] C. Triantafyllou, R. D. Hoge, G. Krueger, C. J. Wiggins, A. Potthast, G. C. Wiggins, and L. L. Wald. Comparison of physiological noise at 1.5 T, 3 T and 7 T and optimization of fMRI acquisition parameters. *NeuroImage*, 26(1):243–250, May 2005.
- [122] Christina Triantafyllou, Jonathan R. Polimeni, and Lawrence L. Wald. Physiological noise and signal-to-noise ratio in fMRI with multi-channel array coils. *NeuroImage*, 55(2):597–606, March 2011.
- [123] A. Buades, B. Coll, and J.-M. Morel. A non-local algorithm for image denoising. In *2005 IEEE Computer Society Conference on Computer Vision and Pattern Recognition (CVPR'05)*, volume 2, pages 60–65 vol. 2, 2005.
- [124] Pierrick Coupé, Pierre Yger, and Christian Barillot. Fast non local means denoising for 3D MR images. *Medical image computing and computer-assisted intervention: MICCAI*, 9(Pt 2):33–40, 2006.
- [125] José V. Manjón, José Carbonell-Caballero, Juan J. Lull, Gracián García-Martí, Luís Martí-Bonmatí, and Montserrat Robles. MRI denoising using non-local means. *Medical Image Analysis*, 12(4):514–523, August 2008.
- [126] Jeff Orchard, Mehran Ebrahimi, and Alexander Wong. Efficient nonlocal-means denoising using the svd. In *2008 15th ieee international conference on image processing*, pages 1732–1735. IEEE, 2008.
- [127] Jeny Rajan, Ben Jeurissen, Marleen Verhoye, Johan Van Audekerke, and Jan Sijbers. Maximum likelihood estimation-based denoising of magnetic resonance images using restricted local neighborhoods. *Physics in Medicine and Biology*, 56(16):5221–5234, August 2011.
- [128] Alessandro Foi. Noise estimation and removal in mr imaging: The variance-stabilization approach. In *2011 IEEE International symposium on biomedical imaging: from nano to macro*, pages 1809–1814. IEEE, 2011.

- [129] Harold Hotelling. Analysis of a complex of statistical variables into principal components. *Journal of educational psychology*, 24(6):417, 1933.
- [130] Charles-Alban Deledalle, Joseph Salmon, Arnak S Dalalyan, et al. Image denoising with patch based pca: local versus global. In *BMVC*, volume 81, pages 425–455, 2011.
- [131] José V. Manjón, Pierrick Coupé, and Antonio Buades. MRI noise estimation and denoising using non-local PCA. *Medical Image Analysis*, 22(1):35–47, May 2015.
- [132] Vladimir Alexandrovich Marchenko and Leonid Andreevich Pastur. Distribution of eigenvalues for some sets of random matrices. *Matematicheskii Sbornik*, 114(4):507–536, 1967.
- [133] Jelle Veraart, Dmitry S. Novikov, Daan Christiaens, Benjamin Ades-aron, Jan Sijbers, and Els Fieremans. Denoising of diffusion MRI using random matrix theory. *NeuroImage*, 142:394–406, November 2016.
- [134] Joseph D Bronzino. *Biomedical Engineering Handbook 2*, volume 2. Springer Science & Business Media, 2000.
- [135] Reuben Mezrich. A perspective on k-space. *Radiology*, 195(2):297–315, 1995.
- [136] David Gottlieb, Chi-Wang Shu, Alex Solomonoff, and Hervé Vandeven. On the Gibbs phenomenon I: recovering exponential accuracy from the Fourier partial sum of a nonperiodic analytic function. *Journal of Computational and Applied Mathematics*, 43(1-2):81–98, November 1992.
- [137] David Gottlieb and Chi-Wang Shu. On the Gibbs Phenomenon and Its Resolution. *SIAM Review*, 39(4):644–668, January 1997.
- [138] Abdul J. Jerri. Lanczos-Like Sigma-Factors for Reducing the Gibbs Phenomenon in General Orthogonal Expansions and Other Representations. *Journal of Computational Analysis and Applications*, 2(2):111–127, April 2000.
- [139] Rick Archibald and Anne Gelb. A method to reduce the Gibbs ringing artifact in MRI scans while keeping tissue boundary integrity. *IEEE transactions on medical imaging*, 21(4):305–319, April 2002.

- [140] Hákon Gudbjartsson and Samuel Patz. The Rician Distribution of Noisy MRI Data. *Magnetic resonance in medicine*, 34(6):910–914, December 1995.
- [141] Cheng Guan Koay and Peter J. Basser. Analytically exact correction scheme for signal extraction from noisy magnitude MR signals. *Journal of Magnetic Resonance (San Diego, Calif.)*: 1997, 179(2):317–322, April 2006.
- [142] Y. Zhang, M. Brady, and S. Smith. Segmentation of brain MR images through a hidden Markov random field model and the expectation-maximization algorithm. *IEEE transactions on medical imaging*, 20(1):45–57, January 2001.
- [143] Stephen M. Smith, Mark Jenkinson, Mark W. Woolrich, Christian F. Beckmann, Timothy E. J. Behrens, Heidi Johansen-Berg, Peter R. Bannister, Marilena De Luca, Ivana Drobniak, David E. Flitney, Rami K. Niazy, James Saunders, John Vickers, Yongyue Zhang, Nicola De Stefano, J. Michael Brady, and Paul M. Matthews. Advances in functional and structural MR image analysis and implementation as FSL. *NeuroImage*, 23:S208–S219, January 2004.
- [144] Nicholas J. Tustison, Brian B. Avants, Philip A. Cook, Yuanjie Zheng, Alexander Egan, Paul A. Yushkevich, and James C. Gee. N4ITK: Improved N3 Bias Correction. *IEEE transactions on medical imaging*, 29(6):1310–1320, June 2010.
- [145] Krzysztof J. Gorgolewski, Tibor Auer, Vince D. Calhoun, R. Cameron Craddock, Samir Das, Eugene P. Duff, Guillaume Flandin, Satrajit S. Ghosh, Tristan Glatard, Yaroslav O. Halchenko, Daniel A. Handwerker, Michael Hanke, David Keator, Xiangrui Li, Zachary Michael, Camille Maumet, B. Nolan Nichols, Thomas E. Nichols, John Pellman, Jean-Baptiste Poline, Ariel Rokem, Gunnar Schaefer, Vanessa Sochat, William Triplett, Jessica A. Turner, Gaël Varoquaux, and Russell A. Poldrack. The brain imaging data structure, a format for organizing and describing outputs of neuroimaging experiments. *Scientific Data*, 3(1):160044, June 2016.
- [146] Krzysztof Gorgolewski, Christopher Burns, Cindee Madison, Dav Clark, Yaroslav Halchenko, Michael Waskom, and Satrajit Ghosh. NiPy: A Flexible, Lightweight and Extensible Neuroimaging Data Processing Framework in Python. *Frontiers in Neuroinformatics*, 5:13, 2011.
- [147] Brian B Avants, Nick Tustison, Gang Song, et al. Advanced normalization tools (ants). *Insight j*, 2(365):1–35, 2009.

- [148] Tal Yarkoni, Christopher J. Markiewicz, Alejandro de la Vega, Krzysztof J. Gorgolewski, Taylor Salo, Yaroslav O. Halchenko, Quinten McNamara, Krista DeStasio, Jean-Baptiste Poline, Hans Johnson, Oscar Esteban, Dmitry Petrov, James D. Kent, Stefan Appelhoff, Valérie Hayot-Sasson, Dylan M. Nielson, Johan Carlin, Gregory Kiar, Kirstie Whitaker, Mathias Goncalves, Satrajit Ghosh, Adina Wagner, Elizabeth DuPre, Andrew Janke, Alexander Ivanov, Ashley Gillman, Johannes Wennberg, Lee S. Tirrell, Steven Tilley II, Adam Li, Jon Haitz Legarreta, Lea Waller, Mainak Jas, Michael Hanke, Russell Poldrack, Chadwick Boulay, Chris Holdgraf, Evgenii Kalenkovich, Isla Staden, James Kent, Remi Gau, Ariel Rokem, Azeez Adebimpe, Bertrand Thirion, Dave F. Kleinschmidt, Erin W Dickie, John A. Lee, John Kruper, Matteo Visconti di Oleggio Castello, Michael Philipp Notter, Pauline Roca, Ross Blair, Shashank Bansal, and Suganya Sundaravadivelu. Pybids: Python tools for bids datasets, August 2021.
- [149] Tal Yarkoni, Christopher J. Markiewicz, Alejandro de la Vega, Krzysztof J. Gorgolewski, Taylor Salo, Yaroslav O. Halchenko, Quinten McNamara, Krista DeStasio, Jean-Baptiste Poline, Dmitry Petrov, Valérie Hayot-Sasson, Dylan M. Nielson, Johan Carlin, Gregory Kiar, Kirstie Whitaker, Elizabeth DuPre, Adina Wagner, Lee S. Tirrell, Mainak Jas, Michael Hanke, Russell A. Poldrack, Oscar Esteban, Stefan Appelhoff, Chris Holdgraf, Isla Staden, Bertrand Thirion, Dave F. Kleinschmidt, John A. Lee, Matteo Visconti Oleggio di Castello, Michael P. Notter, and Ross Blair. PyBIDS: Python tools for BIDS datasets. *Journal of Open Source Software*, 4(40):1294, August 2019.
- [150] Matthew Brett, Ingrid S. Johnsruude, and Adrian M. Owen. The problem of functional localization in the human brain. *Nature Reviews Neuroscience*, 3(3):243–249, March 2002.
- [151] Brian Patenaude, Stephen M. Smith, David N. Kennedy, and Mark Jenkinson. A Bayesian model of shape and appearance for subcortical brain segmentation. *NeuroImage*, 56(3):907–922, June 2011.
- [152] Ben Jeurissen, Jacques-Donald Tournier, Thijs Dhollander, Alan Connelly, and Jan Sijbers. Multi-tissue constrained spherical deconvolution for improved analysis of multi-shell diffusion MRI data. *NeuroImage*, 103:411–426, December 2014.
- [153] J.-Donald Tournier, Fernando Calamante, David G. Gadian, and Alan Connelly. Direct estimation of the fiber orientation density function from diffusion-weighted MRI data using spherical deconvolution. *NeuroImage*, 23(3):1176–1185, November 2004.

- [154] Robert E. Smith, Jacques-Donald Tournier, Fernando Calamante, and Alan Connelly. SIFT2: Enabling dense quantitative assessment of brain white matter connectivity using streamlines tractography. *NeuroImage*, 119:338–351, October 2015.
- [155] Lingzhong Fan, Hai Li, Junjie Zhuo, Yu Zhang, Jiaojian Wang, Liangfu Chen, Zhengyi Yang, Congying Chu, Sangma Xie, Angela R. Laird, Peter T. Fox, Simon B. Eickhoff, Chunshui Yu, and Tianzi Jiang. The Human Brainnetome Atlas: A New Brain Atlas Based on Connectional Architecture. *Cerebral Cortex*, 26(8):3508–3526, August 2016.
- [156] Eleftherios Garyfallidis, Matthew Brett, Bagrat Amirbekian, Ariel Rokem, Stefan Van Der Walt, Maxime Descoteaux, and Ian Nimmo-Smith. Dipy, a library for the analysis of diffusion MRI data. *Frontiers in Neuroinformatics*, 8:8, 2014.
- [157] Jeffrey I. Berman, SungWon Chung, Pratik Mukherjee, Christopher P. Hess, Eric T. Han, and Roland G. Henry. Probabilistic streamline q-ball tractography using the residual bootstrap. *NeuroImage*, 39(1):215–222, January 2008.
- [158] Ariel Rokem, Jason D. Yeatman, Franco Pestilli, Kendrick N. Kay, Aviv Mezer, Stefan van der Walt, and Brian A. Wandell. Evaluating the accuracy of diffusion MRI models in white matter. *PLOS ONE*, 10(4):e0123272, April 2015.
- [159] Eleftherios Garyfallidis, Nahla E, and Yu-Chien Wu. Superresolved HYDI dataset. 11 2019.
- [160] Nahla M H Elsaïd, Pierrick Coupé, and Yu-Chien Wu. Super-resolution hybrid diffusion imaging (SR-HYDI). *International Society for Magnetic Resonance in Medicine (ISMRM)*, 2019.
- [161] Robert C. Wilson and Yael Niv. Is model fitting necessary for model-based fmri? *PLOS Computational Biology*, 11(6):e1004237, June 2015.
- [162] Walter J. Freeman. Tutorial on neurobiology: from single neurons to brain chaos. *International Journal of Bifurcation and Chaos*, 02(03):451–482, September 1992.
- [163] F. H. Lopes da Silva, A. Hoeks, H. Smits, and L. H. Zetterberg. Model of brain rhythmic activity - The alpha-rhythm of the thalamus. *Kybernetik*, 15(1):27–37, May 1974.

- [164] P. A. Robinson, C. J. Rennie, J. J. Wright, H. Bahramali, E. Gordon, and D. L. Rowe. Prediction of electroencephalographic spectra from neurophysiology. *Physical Review E*, 63(2):021903, January 2001.
- [165] P. A. Valdes, J. C. Jimenez, J. Riera, R. Biscay, and T. Ozaki. Nonlinear EEG analysis based on a neural mass model. *Biological Cybernetics*, 81(5):415–424, 1999.
- [166] Jack D. Cowan, Jeremy Neuman, and Wim van Drongelen. Wilson–cowan equations for neocortical dynamics. *The Journal of Mathematical Neuroscience*, 6(1):1, January 2016.
- [167] Sarah Feldt Muldoon, Fabio Pasqualetti, Shi Gu, Matthew Cieslak, Scott T. Grafton, Jean M. Vettel, and Danielle S. Bassett. Stimulation-based control of dynamic brain networks. *PLOS Computational Biology*, 12(9):1–23, 2016.
- [168] J. Zimmermann, A. Perry, M. Breakspear, M. Schirner, P. Sachdev, W. Wen, N. A. Kochan, M. Mapstone, P. Ritter, A. R. McIntosh, and A. Solodkin. Differentiation of alzheimer’s disease based on local and global parameters in personalized virtual brain models. *NeuroImage: Clinical*, 19:240–251, 2018.
- [169] Romesh G. Abeysuriya, Jonathan Hadida, Stamatis N. Sotiropoulos, Saad Jbabdi, Robert Becker, Benjamin A. E. Hunt, Matthew J. Brookes, and Mark W. Woolrich. A biophysical model of dynamic balancing of excitation and inhibition in fast oscillatory large-scale networks. *PLOS Computational Biology*, 14(2):e1006007, February 2018.
- [170] Matthew F. Singh, Todd S. Braver, Michael W. Cole, and ShiNung Ching. Estimation and validation of individualized dynamic brain models with resting state fMRI. *NeuroImage*, 221:117046, November 2020.
- [171] Áine Byrne, Reuben D. O’Dea, Michael Forrester, James Ross, and Stephen Coombes. Next-generation neural mass and field modeling. *Journal of Neurophysiology*, 123(2):726–742, November 2019.
- [172] Peng Wang, Ru Kong, Xiaolu Kong, Raphaël Liégeois, Csaba Orban, Gustavo Deco, Martijn P. van den Heuvel, and B. T. Thomas Yeo. Inversion of a large-scale circuit model reveals a cortical hierarchy in the dynamic resting human brain. *Science Advances*, 5(1):eaat7854, January 2019.
- [173] Agus Hartoyo, Peter J. Cadusch, David T. J. Liley, and Damien G. Hicks. Parameter estimation and identifiability in a neural population model for

- electro-cortical activity. *PLOS Computational Biology*, 15(5):e1006694, May 2019.
- [174] Murat Demirtaş, Joshua B. Burt, Markus Helmer, Jie Lisa Ji, Brendan D. Adkinson, Matthew F. Glasser, David C. Van Essen, Stamatiros N. Sotiropoulos, Alan Anticevic, and John D. Murray. Hierarchical heterogeneity across human cortex shapes large-scale neural dynamics. *Neuron*, 101(6):1181–1194.e13, March 2019.
 - [175] C. J. Honey, O. Sporns, L. Cammoun, X. Gigandet, J. P. Thiran, R. Meuli, and P. Hagmann. Predicting human resting-state functional connectivity from structural connectivity. *Proceedings of the National Academy of Sciences*, 106(6):2035–2040, February 2009.
 - [176] Zhou Lu, Hongming Pu, Feicheng Wang, Zhiqiang Hu, and Liwei Wang. The Expressive Power of Neural Networks: A View from the Width. *arXiv:1709.02540 [cs]*, November 2017. arXiv: 1709.02540.
 - [177] Ding-Xuan Zhou. Universality of deep convolutional neural networks. *Applied and Computational Harmonic Analysis*, 48(2):787–794, March 2020.
 - [178] Michael Schirner, Anthony Randal McIntosh, Viktor Jirsa, Gustavo Deco, and Petra Ritter. Inferring multi-scale neural mechanisms with brain network modelling. *eLife*, 7:e28927, January 2018.
 - [179] Maria Inez Falcon, Jeffrey D. Riley, Viktor Jirsa, Anthony R. McIntosh, Ahmed D. Shereen, E. Elinor Chen, and Ana Solodkin. The virtual brain: Modeling biological correlates of recovery after chronic stroke. *Frontiers in Neurology*, 6:228, November 2015.
 - [180] Gustavo Deco, Joana Cabral, Mark W. Woolrich, Angus B. A. Stevner, Tim J. van Harteveldt, and Morten L. Kringelbach. Single or multiple frequency generators in on-going brain activity: A mechanistic whole-brain model of empirical meg data. *NeuroImage*, 152:538–550, May 2017.
 - [181] J. Hadida, S. N. Sotiropoulos, R. G. Abeysuriya, M. W. Woolrich, and S. Jbabdi. Bayesian optimisation of large-scale biophysical networks. *NeuroImage*, 174:219–236, July 2018.
 - [182] Rahul S. Desikan, Florent Segonne, Bruce Fischl, Brian T. Quinn, Bradford C. Dickerson, Deborah Blacker, Randy L. Buckner, Anders M. Dale, R. Paul Maguire, Bradley T. Hyman, Marilyn S. Albert, and Ronald J.

- Killiany. An automated labeling system for subdividing the human cerebral cortex on MRI scans into gyral based regions of interest. *NeuroImage*, 31:968–980, 2006.
- [183] Jennifer A. McNab, Brian L. Edlow, Thomas Witzel, Susie Y. Huang, Himanshu Bhat, Keith Heberlein, Thorsten Feiweier, Kecheng Liu, Boris Keil, Julien Cohen-Adad, M. Dylan Tisdall, Rebecca D. Folkerth, Hannah C. Kinney, and Lawrence L. Wald. The human connectome project and beyond: Initial applications of 300mt/m gradients. *NeuroImage*, 2013.
- [184] Mark Jenkinson, Christian F. Beckmann, Timothy E.J. Behrens, Mark W. Woolrich, and Stephen M. Smith. Fsl. *NeuroImage*, 62(2):782–790, 2012.
- [185] S S Dalal, J M Zumer, V Agrawal, K E Hild, K Sekihara, and S S Nagarajan. NUTMEG: a neuromagnetic source reconstruction toolbox. *Neurology & clinical neurophysiology : NCN*, 2004:52, 2004.
- [186] Alexandre Gramfort, Martin Luessi, Eric Larson, Denis A. Engemann, Daniel Strohmeier, Christian Brodbeck, Roman Goj, Mainak Jas, Teon Brooks, Lauri Parkkonen, and Matti S. Hämäläinen. MEG and EEG data analysis with MNE-Python. *Frontiers in Neuroscience*, 7(267):1–13, 2013.
- [187] Joerg F. Hipp, David J. Hawellek, Maurizio Corbetta, Markus Siegel, and Andreas K. Engel. Large-scale cortical correlation structure of spontaneous oscillatory activity. *Nature Neuroscience*, 15(6), June 2012.
- [188] Matthew J. Brookes, Joanne R. Hale, Johanna M. Zumer, Claire M. Stevenson, Susan T. Francis, Gareth R. Barnes, Julia P. Owen, Peter G. Morris, and Srikanth S. Nagarajan. Measuring functional connectivity using MEG: Methodology and comparison with fcMRI. *NeuroImage*, 56(3):1082–1104, June 2011.
- [189] W. K. Hastings. Monte Carlo sampling methods using markov chains and their applications. *Biometrika*, 57(1):97–109, April 1970.
- [190] Stuart Geman and Donald Geman. Stochastic relaxation, gibbs distributions, and the bayesian restoration of images. *IEEE Transactions on Pattern Analysis and Machine Intelligence*, PAMI-6(6):721–741, November 1984.
- [191] Alan E. Gelfand and Adrian F. M. Smith. Sampling-based approaches to calculating marginal densities. *Journal of the American Statistical Association*, 85(410):398–409, June 1990.

- [192] Thomas Donoghue, Matar Haller, Erik J. Peterson, Paroma Varma, Priyadarshini Sebastian, Richard Gao, Torben Noto, Antonio H. Lara, Joni D. Wallis, Robert T. Knight, Avgusta Shestyuk, and Bradley Voytek. Parameterizing neural power spectra into periodic and aperiodic components. *Nature Neuroscience*, 23(12):1655–1665, December 2020.
- [193] Ernst Hairer and Gerhard Wanner. *Analysis by Its History*. Readings in Mathematics. Springer-Verlag, New York, 2008.
- [194] Richard B. Buxton, Eric C. Wong, and Lawrence R. Frank. Dynamics of blood flow and oxygenation changes during brain activation: The balloon model. *Magnetic Resonance in Medicine*, 39(6):855–864, 1998.
- [195] K. J. Friston, A. Mechelli, R. Turner, and C. J. Price. Nonlinear responses in fMRI: The Balloon Model, Volterra Kernels, and Other Hemodynamics. *NeuroImage*, 12(4):466–477, October 2000.
- [196] Gustavo Deco, Adrián Ponce-Alvarez, Dante Mantini, Gian Luca Romani, Patric Hagmann, and Maurizio Corbetta. Resting-state functional connectivity emerges from structurally and dynamically shaped slow linear fluctuations. *The Journal of Neuroscience*, 33(27):11239–11252, July 2013.
- [197] G. Deco, A. Ponce-Alvarez, P. Hagmann, G. . Romani, D. Mantini, and M. Corbetta. How local excitation-inhibition ratio impacts the whole brain dynamics. *The Journal of neuroscience*, 34(23):7886–98, 2014. ISBN: 0270-6474.
- [198] Oana-Teodora Chis, Alejandro F. Villaverde, Julio R. Banga, and Eva Balsa-Canto. On the relationship between sloppiness and identifiability. *Mathematical Biosciences*, 282, December 2016.
- [199] Alejandro F. Villaverde. Observability and Structural Identifiability of Nonlinear Biological Systems. *Complexity*, 2019:e8497093, January 2019. Publisher: Hindawi.
- [200] Cassiano Becker, Sérgio Pequito, George Pappas, Michael Miller, Scott Grafton, Danielle Bassett, and Victor M. Preciado. Spectral mapping of brain functional connectivity from diffusion imaging. *Nature Scientific Reports*, 8(1411), 2018.
- [201] Ashish Raj, Chang Cai, Xihe Xie, Eva Palacios, Julia Owen, Pratik Mukherjee, and Srikanth Nagarajan. Spectral graph theory of brain oscillations. *Human Brain Mapping*, 41(11):2980–2998, 2020.

- [202] Friedemann Pulvermüller, Rosario Tomasello, Malte R. Henningsen-Schomers, and Thomas Wennekers. Biological constraints on neural network models of cognitive function. *Nature Reviews Neuroscience*, 22(8), August 2021.
- [203] Erfan Nozari, Jennifer Stiso, Lorenzo Caciagli, Eli J. Cornblath, Xiaosong He, Maxwell A. Bertolero, Arun S. Mahadevan, George J. Pappas, and Danielle S. Bassett. Is the brain macroscopically linear? a system identification of resting state dynamics. *arXiv:2012.12351 [cs, eess, math, q-bio]*, December 2020.
- [204] Andrew Gelman and Donald B. Rubin. Inference from iterative simulation using multiple sequences. *Statistical Science*, 7(4):457–472, November 1992.
- [205] Jonathan Goodman and Jonathan Weare. Ensemble samplers with affine invariance. *Communications in Applied Mathematics and Computational Science*, 5(1):65–80, January 2010. Publisher: Mathematical Sciences Publishers.
- [206] S Kirkpatrick, C D Gelatt, and M P Vecchi. Optimization by simulated annealing. *Science*, 220(4598):671–680, 1983.
- [207] David J. Wales and Jonathan P.K. Doye. Global optimization by basin-hopping and the lowest energy structures of lennard-jones clusters containing up to 110 atoms. *Journal of Physical Chemistry A*, 101:5111–5116, 1997.
- [208] Karl J. Friston, Baojuan Li, Jean Daunizeau, and Klaas E. Stephan. Network discovery with dcm. *NeuroImage*, 56(3):1202–1221, June 2011.
- [209] Klaas E Stephan, Lars Kasper, Lee M Harrison, Jean Daunizeau, Hanneke E M den Ouden, Michael Breakspear, and Karl J Friston. Nonlinear dynamic causal models for fmri. *NeuroImage*, 42(2):649–662, 2008.
- [210] Dustin Tran, Matthew D. Hoffman, Dave Moore, Christopher Suter, Srinivas Vasudevan, Alexey Radul, Matthew Johnson, and Rif A. Saurous. Simple, distributed, and accelerated probabilistic programming. In *Neural Information Processing Systems*, 2018.
- [211] John Salvatier, Thomas V. Wiecki, and Christopher Fonnesbeck. Probabilistic programming in python using PyMC3. *PeerJ Computer Science*, 2:e55, apr 2016.

- [212] Sara Sommariva, Alberto Sorrentino, Michele Piana, Vittorio Pizzella, and Laura Marzetti. A comparative study of the robustness of frequency-domain connectivity measures to finite data length. *Brain Topography*, 32(4):675–695, July 2019.
- [213] Ed Bullmore and Olaf Sporns. Complex brain networks: graph theoretical analysis of structural and functional systems. *Nature Reviews Neuroscience*, 10(3):186–198, March 2009.
- [214] R. Cameron Craddock, G. Andrew James, Paul E. Holtzheimer, Xiaoping P. Hu, and Helen S. Mayberg. A whole brain fMRI atlas generated via spatially constrained spectral clustering. *Human brain mapping*, 33, 2012.
- [215] Danielle S. Bassett and Edward T. Bullmore. Human brain networks in health and disease. *Current Opinion in Neurology*, 22:340–347, August 2009.
- [216] Miao Cao, Jin-Hui Wang, Zheng-Jia Dai, Xiao-Yan Cao, Li-Li Jiang, Feng-Mei Fan, Xiao-Wei Song, Ming-Rui Xia, Ni Shu, Qi Dong, Michael P. Milham, F. Xavier Castellanos, Xi-Nian Zuo, and Yong He. Topological organization of the human brain functional connectome across the lifespan. *Developmental Cognitive Neuroscience*, 7, 2014.
- [217] Nivedita Chatterjee and Sitabhra Sinha. Understanding the mind of a worm: hierarchical network structure underlying nervous system function in c. elegans. *Progress in Brain Research*, 168:145–153, 2008.
- [218] Y. He, Z. Chen, and A. Evans. Structural insights into aberrant topological patterns of large-scale cortical networks in alzheimer’s disease. *Journal of Neuroscience*, 28:4756–4766, 2008.
- [219] R. L. Buckner. Molecular, structural, and functional characterization of alzheimer’s disease: Evidence for a relationship between default activity, amyloid, and memory. *Journal of Neuroscience*, 25:7709–7717, 2005.
- [220] N Brunel and N Brunel. Dynamics of sparsely connected networks of excitatory and inhibitory neurons. *Computational Neuroscience*, 8:183–208, 2000.
- [221] Nicolas Brunel and Xiao Jing Wang. Effects of neuromodulation in a cortical network model of object working memory dominated by recurrent inhibition. *Journal of Computational Neuroscience*, 11:63–85, 2001.

- [222] Laura E. Suárez, Ross D. Markello, Richard F. Betzel, and Bratislav Misic. Linking structure and function in macroscale brain networks. *Trends in Cognitive Sciences*, 24:302–315, 2020-04-01.
- [223] Shi Gu, Fabio Pasqualetti, Matthew Cieslak, Qawi K. Telesford, Alfred B. Yu, Ari E. Kahn, John D. Medaglia, Jean M. Vettel, Michael B. Miller, Scott T. Grafton, and Danielle S. Bassett. Controllability of structural brain networks. *Nature Communications*, 6:8414, 2015.
- [224] Sami El Boustani and Alain Destexhe. A master equation formalism for macroscopic modeling of asynchronous irregular activity states. *Neural computation*, 21(1):46–100, 2009.
- [225] Paul L. Nunez. The brain wave equation: a model for the EEG. *Mathematical Biosciences*, 21(3):279–297, 1974.
- [226] V. K. Jirsa and H. Haken. A derivation of a macroscopic field theory of the brain from the quasi-microscopic neural dynamics. *Physica D: Nonlinear Phenomena*, 99(4):503–526, 1997-01-01.
- [227] A. Spiegler and V. Jirsa. Systematic approximations of neural fields through networks of neural masses in the virtual brain. *NeuroImage*, 83(March):704–725, 2013.
- [228] Farras Abdenour, Henning U. Voss, and Ashish Raj. Network diffusion accurately models the relationship between structural and functional brain connectivity networks. *NeuroImage*, 90:335–347, 2014.
- [229] Selen Atasoy, Isaac Donnelly, and Joel Pearson. Human brain networks function in connectome-specific harmonic waves. *Nature Communications*, 7(1):10340, April 2016.
- [230] Prejaas Tewarie, Romesh Abeysuriya, Aine Byrne, George C. O'Neill, Stamatios N. Sotiropoulos, Matthew J. Brookes, and Stephen Coombes. How do spatially distinct frequency specific MEG networks emerge from one underlying structural connectome? the role of the structural eigenmodes. *NeuroImage*, 186:211–220, 2019.
- [231] Ashish Raj, Chang Cai, Xihe Xie, Eva Palacios, Julia Owen, Pratik Mukherjee, and Srikanth Nagarajan. Spectral graph theory of brain oscillations. *Human Brain Mapping*, 41(11):1–19, 2020.

- [232] Farras Abdehnour, Michael Dayan, Orrin Devinsky, Thomas Thesen, and Ashish Raj. Functional brain connectivity is predictable from anatomic network's laplacian eigen-structure. *NeuroImage*, 172:728–739, 2018.
- [233] Ian Stewart. Holes and hot spots. *Nature*, 401:863–865, 1999.
- [234] P. A. Robinson, X. Zhao, K. M. Aquino, J. D. Griffiths, S. Sarkar, and Grishma Mehta-Pandejee. Eigenmodes of brain activity: Neural field theory predictions and comparison with experiment. *NeuroImage*, 142:79–98, 2016.
- [235] Maria Giulia Preti and Dimitri Van De Ville. Decoupling of brain function from structure reveals regional behavioral specialization in humans. *Nature Communications*, 10, 2019.
- [236] A.P. French. *Vibrations and Waves*. M.I.T. introductory physics series. Taylor & Francis, 1971.
- [237] Bruce Fischl, David H Salat, Evelina Busa, Marilyn Albert, Megan Dieterich, Christian Haselgrove, Andre Van Der Kouwe, Ron Killiany, David Kennedy, Shuna Klaveness, Albert Montillo, Nikos Makris, Bruce Rosen, and Anders M Dale. Whole brain segmentation: Automated labeling of neuroanatomical structures in thehuman brain. *Neuron*, 33:341–355, 2002.
- [238] Mikhail Belkin and Partha Niyogi. Laplacian eigenmaps for dimensionality reduction and data representation. *Neural Computation*, 15(6):1373–1396, 2003.
- [239] Jiu-Gang Dong and Li Qiu. Complex laplacians and applications in multi-agent systems. *arXiv*, 2015.
- [240] Tianzi Jiang. Brainnetome: a new -ome to understand the brain and its disorders. *NeuroImage*, 80:263–272, 2013.
- [241] Alex Fornito, Andrew Zalesky, and Michael Breakspear. The connectomics of brain disorders. *Nature Reviews. Neuroscience*, 16(3):159–172, 2015.
- [242] Ana C. Coan, Brunno M. Campos, Clarissa L. Yasuda, Bruno Y. Kubota, Felipe Pg Bergo, Carlos Am Guerreiro, and Fernando Cendes. Frequent seizures are associated with a network of gray matter atrophy in temporal lobe epilepsy with or without hippocampal sclerosis. *PloS One*, 9(1):e85843, 2014.

- [243] A. Kuceyeski, S. Shah, J. P. Dyke, S. Bickel, F. Abdelnour, N. D. Schiff, H. U. Voss, and A. Raj. The application of a mathematical model linking structural and functional connectomes in severe brain injury. *NeuroImage: Clinical*, 11:635–647, 2016.
- [244] Anne K. Rehme and Christian Grefkes. Cerebral network disorders after stroke: evidence from imaging-based connectivity analyses of active and resting brain states in humans. *The Journal of Physiology*, 591(1):17–31, 2013.
- [245] Jaroslav Hlinka, Milan Palus, Martin Vejmelka, Dante Mantini, and Maurizio Corbetta. Functional connectivity in resting-state fMRI: is linear correlation sufficient? *NeuroImage*, 54(3):2218–2225, 2011.
- [246] D. Hartman, J. Hlinka, M. Palus, D. Mantini, and M. Corbetta. The role of nonlinearity in computing graph-theoretical properties of resting-state functional magnetic resonance imaging brain networks. *Chaos (Woodbury, N.Y.)*, 21(1):013119, 2011.
- [247] Pascal Fries. A mechanism for cognitive dynamics: neuronal communication through neuronal coherence. *Trends in Cognitive Sciences*, 9(10):474–480, 2005.
- [248] Alfons Schnitzler and Joachim Gross. Normal and pathological oscillatory communication in the brain. *Nature Reviews Neuroscience*, 6(4):285–296, 2005-04.
- [249] Francisco Varela, Jean-Philippe Lachaux, Eugenio Rodriguez, and Jacques Martinerie. The brainweb: Phase synchronization and large-scale integration. *Nature Reviews Neuroscience*, 2(4):229–239, 2001-04. Number: 4 Publisher: Nature Publishing Group.
- [250] A. Ghosh, Y. Rho, A. R. McIntosh, R. Kötter, and V. K. Jirsa. Cortical network dynamics with time delays reveals functional connectivity in the resting brain. *Cognitive Neurodynamics*, 2(2):115, April 2008.
- [251] Anandamohan Ghosh, Y. Rho, A. R. McIntosh, R. Kötter, and V. K. Jirsa. Noise during rest enables the exploration of the brain’s dynamic repertoire. *PLoS Computational Biology*, 4(10), 2008.
- [252] Olivier David and Karl J. Friston. A neural mass model for meg/eeg: coupling and neuronal dynamics. *NeuroImage*, 20(3):1743–1755, November 2003.

- [253] Joana Cabral, Etienne Hugues, Morten L. Kringelbach, and Gustavo Deco. Modeling the outcome of structural disconnection on resting-state functional connectivity. *NeuroImage*, 62(3):1342–1353, 2012.
- [254] V. K. Jirsa, O. Sporns, M. Breakspear, G. Deco, and A. R. McIntosh. Towards the virtual brain: Network modeling of the intact and the damaged brain. *Archives Italiennes de Biologie*, 148:189–205, 2010.
- [255] I Lorena Arancibia-Cárcamo, Marc C Ford, Lee Cossell, Kinji Ishida, Koujiro Tohyama, and David Attwell. Node of ranvier length as a potential regulator of myelinated axon conduction speed. *eLife*, 6:e23329, 2017.
- [256] R. Douglas Fields. A new mechanism of nervous system plasticity: activity-dependent myelination. *Nature Reviews Neuroscience*, 16(12):756–767, 2015-12.
- [257] Aaron F. Alexander-Bloch, Petra E. Vértes, Reva Stidd, François Lalonde, Liv Clasen, Judith Rapoport, Jay Giedd, Edward T. Bullmore, and Nitin Gogtay. The anatomical distance of functional connections predicts brain network topology in health and schizophrenia. *Cerebral Cortex (New York, NY)*, 23(1):127–138, 2013-01.
- [258] Joaquín Goñi, Martijn P. van den Heuvel, Andrea Avena-Koenigsberger, Nieves Velez de Mendizabal, Richard F. Betzel, Alessandra Griffa, Patric Hagmann, Bernat Corominas-Murtra, Jean-Philippe Thiran, and Olaf Sporns. Resting-brain functional connectivity predicted by analytic measures of network communication. *Proceedings of the National Academy of Sciences*, 111(2):833–838, January 2014.
- [259] C. J. Stam, E. C. W. van Straaten, E. Van Dellen, P. Tewarie, G. Gong, A. Hillebrand, J. Meier, and P. Van Mieghem. The relation between structural and functional connectivity patterns in complex brain networks. *International Journal of Psychophysiology*, 103:149–160, 2016.
- [260] Jil Meier, Prejaas Tewarie, Arjan Hillebrand, Linda Douw, Bob W. van Dijk, Steven M. Stufflebeam, and Piet Van Mieghem. A mapping between structural and functional brain networks. *Brain Connectivity*, 6(4):298–311, 2016.
- [261] Samuel Deslauriers-Gauthier, M Zucchelli, M Frigo, and Rachid Deriche. A unified framework for multimodal structure-function mapping based on eigenmodes. *Medical Image Analysis*, 66:101799, 2020.

- [262] Prejaas Tewarie, B Prasse, JM Meier, F Santos, L Douw, MM Schoonheim, CJ Stam, P 5 Van Mieghem, and A Hillebrand. Mapping functional brain networks from the structural connectome: Relating the series expansion and eigenmode approaches. *Neuroimage*, 216:116805, 2020.
- [263] D. A. Pinotsis, J. P. Geerts, L. Pinto, T. H. B. FitzGerald, V. Litvak, R. Auksztulewicz, and K. J. Friston. Linking canonical microcircuits and neuronal activity: Dynamic causal modelling of laminar recordings. *NeuroImage*, 146:355–366, February 2017.
- [264] Adeel Razi, Joshua Kahan, Geraint Rees, and Karl J. Friston. Construct validation of a dcm for resting state fmri. *NeuroImage*, 106:1–14, 2015.
- [265] Hae Jeong Park, Karl J. Friston, Chongwon Pae, Bumhee Park, and Adeel Razi. Dynamic effective connectivity in resting state fmri. *NeuroImage*, 180(May 2017):594–608, 2018.
- [266] Maria Giulia Preti, Thomas AW Bolton, and Dimitri Van De Ville. The dynamic functional connectome: State-of-the-art and perspectives. *NeuroImage*, 160:41–54, October 2017.
- [267] Frederik Van de Steen, Hannes Almgren, Adeel Razi, Karl Friston, and Daniele Marinazzo. Dynamic causal modelling of fluctuating connectivity in resting-state eeg. *NeuroImage*, 189:476–484, April 2019.
- [268] Stefan Frässle, Ekaterina I. Lomakina, Lars Kasper, Zina M. Manjaly, Alex Leff, Klaas P. Pruessmann, Joachim M. Buhmann, and Klaas E. Stephan. A generative model of whole-brain effective connectivity. *NeuroImage*, 179(May):505–529, 2018.
- [269] Stefan Frässle, Ekaterina I. Lomakina, Adeel Razi, Karl J. Friston, Joachim M. Buhmann, and Klaas E. Stephan. Regression dcm for fmri. *NeuroImage*, 155(February):406–421, 2017.
- [270] Adeel Razi, Mohamed L. Seghier, Yuan Zhou, Peter McColgan, Peter Zeidman, Hae-Jeong Park, Olaf Sporns, Geraint Rees, and Karl J. Friston. Large-scale dcms for resting-state fmri. *Network Neuroscience*, 1(3):222–241, October 2017.
- [271] Daniel S. Margulies, Satrajit S. Ghosh, Alexandros Goulas, Marcel Falkiewicz, Julia M. Huntenburg, Georg Langs, Gleb Bezgin, Simon B. Eickhoff, F. Xavier Castellanos, Michael Petrides, Elizabeth Jefferies, and

- Jonathan Smallwood. Situating the default-mode network along a principal gradient of macroscale cortical organization. *Proceedings of the National Academy of Sciences*, 113(44):12574–12579, 2016.
- [272] Jorge Sepulcre, Mert R. Sabuncu, Thomas B. Yeo, Hesheng Liu, and Keith A. Johnson. Stepwise connectivity of the modal cortex reveals the multimodal organization of the human brain. *Journal of Neuroscience*, 32(31):10649–10661, 2012.
- [273] Bertha Vázquez-Rodríguez, Laura E. Suárez, Ross D. Markello, Golia Shafiei, Casey Paquola, Patric Hagmann, Martijn P. van den Heuvel, Boris C. Bernhardt, R. Nathan Spreng, and Bratislav Misic. Gradients of structure–function tethering across neocortex. *Proceedings of the National Academy of Sciences*, page 201903403, 2019.
- [274] Julia M. Huntenburg, Pierre-Louis Bazin, and Daniel S. Margulies. Large-scale gradients in human cortical organization. *Trends in Cognitive Sciences*, 22(1):21–31, 2018.
- [275] Randy L. Buckner and Daniel S. Margulies. Macroscale cortical organization and a default-like apex transmodal network in the marmoset monkey. *Nature Communications*, 10(1):1976, 2019.
- [276] William W. Seeley, Vinod Menon, Alan F. Schatzberg, Jennifer Keller, Gary H. Glover, Heather Kenna, Allan L. Reiss, and Michael D. Greicius. Dissociable intrinsic connectivity networks for salience processing and executive control. *Journal of Neuroscience*, 27:2349–2356, 2007.
- [277] Michael D. Fox, Abraham Z. Snyder, Justin L. Vincent, Maurizio Corbetta, David C. Van Essen, and Marcus E. Raichle. The human brain is intrinsically organized into dynamic, anticorrelated functional networks. *Proceedings of the National Academy of Sciences*, 102:9673–9678, 2005.
- [278] Patric Hagmann, Leila Cammoun, Xavier Gigandet, Reto Meuli, Christopher J. Honey, Van J. Wedeen, and Olaf Sporns. Mapping the structural core of human cerebral cortex. *PLOS Biology*, 6(7):e159, July 2008.
- [279] Yasser Iturria-Medina. Anatomical brain networks on the prediction of abnormal brain states. *Brain connectivity*, 3(1):1–21, January 2013.
- [280] Walter J. Freeman and Jian Zhai. Simulated power spectral density (psd) of background electrocorticogram (ecog). *Cognitive Neurodynamics*, 3(1):97–103, March 2009.

- [281] D T J Liley, D M Alexander, JJ Wright, and M D Aldous. Alpha rhythm emerges from large-scale networks of realistically coupled multicompartmental model cortical neurons. *Network-Computation In Neural Systems*, 10(1):79–92, 1999.
- [282] Per E. Roland, Claus C. Hilgetag, and Gustavo Deco. Tracing evolution of spatio-temporal dynamics of the cerebral cortex: cortico-cortical communication dynamics. *Frontiers in Systems Neuroscience*, 8:76, 2014.
- [283] Valentin Markounikau, Christian Igel, Amiram Grinvald, and Dirk Jancke. A dynamic neural field model of mesoscopic cortical activity captured with voltage-sensitive dye imaging. *PLOS Computational Biology*, 6(9):e1000919, September 2010.
- [284] Evan S. Schaffer, Srdjan Ostojic, and L. F. Abbott. A complex-valued firing-rate model that approximates the dynamics of spiking networks. *PLOS Computational Biology*, 9(10):e1003301, October 2013.
- [285] Henry Markram. The Blue Brain Project. *Nature Reviews Neuroscience*, 7(2):153–160, February 2006.
- [286] Henry Markram, Eilif Muller, Srikanth Ramaswamy, Michael W. Reimann, Marwan Abdellah, Carlos Aguado Sanchez, Anastasia Ailamaki, Lidia Alonso-Nanclares, Nicolas Antille, Selim Arsever, Guy Antoine Atenekeng Kahou, Thomas K. Berger, Ahmet Bilgili, Nenad Buncic, Athanassia Chalimourda, Giuseppe Chindemi, Jean-Denis Courcol, Fabien Delalondre, Vincent Delattre, Shaul Druckmann, Raphael Dumusc, James Dynes, Stefan Eilemann, Eyal Gal, Michael Emiel Gevaert, Jean-Pierre Ghobril, Albert Gidon, Joe W. Graham, Anirudh Gupta, Valentin Haenel, Etay Hay, Thomas Heinis, Juan B. Hernando, Michael Hines, Lida Kanari, Daniel Keller, John Kenyon, Georges Khazen, Yihwa Kim, James G. King, Zoltan Kisvarday, Pramod Kumbhar, Sébastien Lasserre, Jean-Vincent Le Bé, Bruno R. C. Magalhães, Angel Merchán-Pérez, Julie Meystre, Benjamin Roy Morrice, Jeffrey Muller, Alberto Muñoz-Céspedes, Shruti Muralidhar, Keerthan Muthurasa, Daniel Nachbaur, Taylor H. Newton, Max Nolte, Aleksandr Ovcharenko, Juan Palacios, Luis Pastor, Rodrigo Perin, Rajnish Ranjan, Imad Riachi, José-Rodrigo Rodríguez, Juan Luis Riquelme, Christian Rössert, Konstantinos Sfyrakis, Ying Shi, Julian C. Shillcock, Gilad Silberberg, Ricardo Silva, Farhan Tauheed, Martin Telefont, Maria Toledo-Rodriguez, Thomas Tränkler, Werner Van Geit, Jafet Villafranca Díaz, Richard Walker, Yun Wang, Stefano M. Zaninetta, Javier DeFelipe, Sean L. Hill, Idan Segev, and Felix Schürmann. Reconstruction and simulation of neocortical microcircuitry. *Cell*, 163(2):456–492, October 2015.

- [287] Eugene M. Izhikevich and Gerald M. Edelman. Large-scale model of mammalian thalamocortical systems. *Proceedings of the National Academy of Sciences*, 105(9):3593–3598, March 2008.
- [288] Tobias C. Potjans and Markus Diesmann. The cell-type specific cortical microcircuit: relating structure and activity in a full-scale spiking network model. *Cerebral Cortex (New York, N.Y.: 1991)*, 24(3):785–806, March 2014.
- [289] H. Shimizu and H. Haken. Co-operative dynamics in organelles. *Journal of Theoretical Biology*, 104(2):261–273, September 1983.
- [290] Bratislav Mišić, Olaf Sporns, and Anthony R. McIntosh. Communication efficiency and congestion of signal traffic in large-scale brain networks. *PLoS Computational Biology*, 10(1), 2014.
- [291] Bratislav Mišić, Richard F. Betzel, Azadeh Nematzadeh, Joaquin Goñi, Alessandra Griffa, Patric Hagmann, Alessandro Flammini, Yong Yeol Ahn, and Olaf Sporns. Cooperative and competitive spreading dynamics on the human connectome. *Neuron*, 86(6):1518–1529, 2015.
- [292] P a Robinson, C J Rennie, D L Rowe, S C O'Connor, E Gordon, S C O Connor, and E Gordon. Multiscale brain modelling. *Philosophical transactions of the Royal Society of London. Series B, Biological sciences*, 360(1457):1043–50, 2005.
- [293] Alain Destexhe and Terrence J. Sejnowski. The wilson-cowan model, 36 years later. *Biological Cybernetics*, 101(1):1–2, 2009.
- [294] F Abdelnour, A Raj, M Dayan, O Devinsky, and T Thesen. Estimating function from structure in epileptics using graph diffusion model. In *2015 IEEE 12th International Symposium on Biomedical Imaging (ISBI)*, pages 466–469, April 2015.
- [295] Tristan T Nakagawa, Mark Woolrich, Henry Luckhoo, Morten Joensson, Hamid Mohseni, Morten L Kringlebach, Viktor Jirsa, and Gustavo Deco. How delays matter in an oscillatory whole-brain spiking-neuron network model for MEG alpha-rhythms at rest. *NeuroImage*, 87:383–94, February 2014.
- [296] V.K. Jirsa, K.J. Jantzen, A. Fuchs, and J.A.S. Kelso. Spatiotemporal forward solution of the eeg and meg using network modeling. *IEEE Transactions on Medical Imaging*, 21(5):493–504, May 2002.

- [297] Gustavo Deco, Mario Senden, and Viktor Jirsa. How anatomy shapes dynamics: a semi-analytical study of the brain at rest by a simple spin model. *Frontiers in computational neuroscience*, 6:68, January 2012.
- [298] Sophie Achard, Raymond Salvador, Brandon Whitcher, John Suckling, and Ed Bullmore. A resilient, low-frequency, small-world human brain functional network with highly connected association cortical hubs. *The Journal of neuroscience : the official journal of the Society for Neuroscience*, 26(1):63–72, January 2006.
- [299] Steven H. Strogatz. Exploring complex networks. *Nature*, 410(6825):268–76, March 2001.
- [300] Martijn P. van den Heuvel, René C. W. Mandl, René S. Kahn, and Hilleke E. Hulshoff Pol. Functionally linked resting-state networks reflect the underlying structural connectivity architecture of the human brain. *Human Brain Mapping*, 30(10):3127–3141, October 2009.
- [301] Ann M. Hermundstad, Danielle S. Bassett, Kevin S. Brown, Elissa M. Aminoff, David Clewett, Scott Freeman, Amy Frithsen, Arianne Johnson, Christine M. Tipper, Michael B. Miller, Scott T. Grafton, and Jean M. Carlson. Structural foundations of resting-state and task-based functional connectivity in the human brain. *Proceedings of the National Academy of Sciences of the United States of America*, 110(15):6169–6174, April 2013.
- [302] Mikail Rubinov, Olaf Sporns, Cees van Leeuwen, and Michael Breakspear. Symbiotic relationship between brain structure and dynamics. *BMC Neuroscience*, 10(1):55, June 2009.
- [303] Hae-Jeong Park and Karl Friston. Structural and functional brain networks: from connections to cognition. *Science (New York, N.Y.)*, 342(6158):1238411, November 2013.
- [304] Biyu J. He, John M. Zempel, Abraham Z. Snyder, and Marcus E. Raichle. The temporal structures and functional significance of scale-free brain activity. *Neuron*, 66(3):353–369, May 2010.
- [305] H. R. Wilson and J. D. Cowan. A mathematical theory of the functional dynamics of cortical and thalamic nervous tissue. *Kybernetik*, 13(2):55–80, September 1973.
- [306] Rasmus Larsen, Mads Nielsen, Jon Sporring, Fan Zhang, and Edwin Han-

- cock. *Medical Image Computing and Computer-Assisted Intervention – MICCAI 2006*, volume 4191. Springer Berlin Heidelberg, Berlin, Heidelberg, 2006.
- [307] Risi Imre Kondor and John Lafferty. Diffusion kernels on graphs and other discrete structures. In *In Proceedings of the ICML*, pages 315–322, 2002.
 - [308] Benjamin Auffarth. Spectral graph clustering. *Universitat de Barcelona, course report for*, pages 1–12, 2007.
 - [309] Andrew Y. Ng, Michael I. Jordan, and Yair Weiss. On spectral clustering: Analysis and an algorithm. In *ADVANCES IN NEURAL INFORMATION PROCESSING SYSTEMS*, pages 849–856. MIT Press, 2001.
 - [310] Roberto F. Galán. On How Network Architecture Determines the Dominant Patterns of Spontaneous Neural Activity. *PLOS ONE*, 3(5):e2148, May 2008.
 - [311] Maxwell B. Wang, Julia P. Owen, Pratik Mukherjee, and Ashish Raj. Brain network eigenmodes provide a robust and compact representation of the structural connectome in health and disease. *PLOS Computational Biology*, 13(6):e1005550, June 2017.
 - [312] Farras Abdnour, Susanne Mueller, and Ashish Raj. Relating cortical atrophy in temporal lobe epilepsy with graph diffusion-based network models. *PLOS Computational Biology*, 11(10):e1004564, October 2015.
 - [313] Farras Abdnour, Ashish Raj, Orrin Devinsky, and Thomas Thesen. Network analysis on predicting mean diffusivity change at group level in temporal lobe epilepsy. *Brain Connectivity*, 6(8):607–620, October 2016.
 - [314] Ashish Raj, Amy Kuceyeski, and Michael Weiner. A network diffusion model of disease progression in dementia. *Neuron*, 73(6):1204–1215, March 2012.
 - [315] Isabelle Ferezou, Florent Haiss, Luc J. Gentet, Rachel Aronoff, Bruno Weber, and Carl C. H. Petersen. Spatiotemporal Dynamics of Cortical Sensorimotor Integration in Behaving Mice. *Neuron*, 56(5):907–923, December 2007.
 - [316] Pierre-Olivier Polack and Diego Contreras. Long-Range Parallel Processing and Local Recurrent Activity in the Visual Cortex of the Mouse. *The Journal of Neuroscience*, 32(32):11120–11131, August 2012.

- [317] Julia P. Owen, Yi-Ou Li, Etay Ziv, Zoe Strominger, Jacquelyn Gold, Polina Bukhpun, Mari Wakahiro, Eric J. Friedman, Elliott H. Sherr, and Pratik Mukherjee. The structural connectome of the human brain in agenesis of the corpus callosum. *NeuroImage*, 70:340–355, April 2013.
- [318] David P. Wipf, Julia P. Owen, Hagai T. Attias, Kensuke Sekihara, and Srikantan S. Nagarajan. Robust Bayesian estimation of the location, orientation, and time course of multiple correlated neural sources using MEG. *NeuroImage*, 49(1):641–655, January 2010.
- [319] Johanna M. Zumer, Hagai T. Attias, Kensuke Sekihara, and Srikantan S. Nagarajan. Probabilistic algorithms for meg/eeg source reconstruction using temporal basis functions learned from data. *NeuroImage*, 41(3):924–940, July 2008.
- [320] K. Jerbi, S. Baillet, J. C. Mosher, G. Nolte, L. Garnero, and R. M. Leahy. Localization of realistic cortical activity in meg using current multipoles. *NeuroImage*, 22(2):779–793, June 2004.
- [321] S S Dalal, J M Zumer, V Agrawal, K E Hild, K Sekihara, and S S Nagarajan. Nutmeg: a neuromagnetic source reconstruction toolbox. *Neurology & clinical neurophysiology : NCN*, 2004:52, 2004.
- [322] Paul L. Nunez and Ramesh Srinivasan. A theoretical basis for standing and traveling brain waves measured with human eeg with implications for an integrated consciousness. *Clinical Neurophysiology: Official Journal of the International Federation of Clinical Neurophysiology*, 117(11):2424–2435, November 2006.
- [323] Sujith Vijayan, ShiNung Ching, Patrick L. Purdon, Emery N. Brown, and Nancy J. Kopell. Thalamocortical mechanisms for the anteriorization of alpha rhythms during propofol-induced unconsciousness. *The Journal of Neuroscience*, 33(27):11070–11075, July 2013.
- [324] A. van Rotterdam, F. H. Lopes da Silva, J. van den Ende, M. A. Viergever, and A. J. Hermans. A model of the spatial-temporal characteristics of the alpha rhythm. *Bulletin of Mathematical Biology*, 44(2):283–305, January 1982.
- [325] D.T.J. Liley, P.J. Cadusch, and M.P. Dafilis. A spatially continuous mean field theory of electrocortical activity. *Network: Computation in Neural Systems*, 13(1):67–113, January 2002.

- [326] Paul L. Nunez. A study of origins of the time dependencies of scalp eeg: I - theoretical basis. *IEEE Transactions on Biomedical Engineering*, BME-28(3):271–280, March 1981.
- [327] J. Daunizeau, O. David, and K. E. Stephan. Dynamic causal modelling: a critical review of the biophysical and statistical foundations. *NeuroImage*, 58(2):312–322, September 2011.
- [328] K J Friston, Katrin H Preller, Chris Mathys, Hayriye Cagnan, Jakob Heinze, Adeel Razi, and Peter Zeidman. Dynamic causal modelling revisited. *NeuroImage*, 199(February), 2017.
- [329] D. A. Pinotsis, E. Hansen, K. J. Friston, and V. K. Jirsa. Anatomical connectivity and the resting state activity of large cortical networks. *NeuroImage*, 65:127–138, 2013.